UNIVERSIDADE DA BEIRA INTERIOR
Engenharia

Study of Low Earth Orbit impact on ORCA^{2}SAT subsystems

Luís Henrique Romeiro da Silva Simões

Dissertação para obtenção do Grau de Mestre em
Engenharia Aeronáutica
(Ciclo de Estudos Integrado)

Orientador: Prof. Doutor Kouamana Bousson
Orientador: Prof. Doutor Afzal Suleman

Covilhã, Janeiro de 2019

Dedicated to my Mother.

Acknowledgments

I would like to thank both my supervisors: Dr. Kouamana Bousson and Dr. Afzal Suleman. Dr. Bousson always showed interest in my work throughout my journey at University of Beira Interior, making me improving my skills, knowledge and to instill the need for me to do better every time. Dr. Suleman provided the amazing opportunity of developing this thesis at University of Victoria and supported the work with all his knowledge and contacts network. More than expressing my gratitude, I would like to refer that under your guidance I was able to acquire skills which will definitely help me in my future as an engineer.

I would also like to thank the UVic Satellite Design Team, especially the team leads, for always being ready to help and share their knowledge, making all this work more interesting and enlightening. To the other Portuguese students also doing their thesis under Dr. Suleman's guidance, I would like to thank for the fun environment and road trips we shared. Without a doubt, you all made my staying in Canada much more pleasant.

To all my house mates throughout my university journey, I would like to express my gratitude for all the fun and crazy moments and also for the brotherhood we developed. To all the different and amazing people I was able to meet during my journey through Covilhã, São Carlos and Victoria who are, unfortunately, far too many to enumerate, I would like to thank them for always teaching me different lessons and sharing experiences making me a better person everyday.

Lastly, I would like to conclude by thanking my family, especially my mother, for their everyday support and sacrifices, for pushing and encouraging me to take a chance, to follow my ambitions and performing better than the day before.

Resumo

O planeamento de missões de CubeSats pode ser bastante desafiante devido às suas restrições de massa, volume e energia. Além disso, a maioria dos projetos de CubeSats são a nível universitário, o que pode também significar restrições de orçamento. De modo a garantir o sucesso da missão, vários aspetos devem ser estudados antes do lançamento. Primeiramente, deve-se certificar que o satélite tem tempos de acesso suficientes às estações em solo desejadas de modo a estabelecer comunicações enquanto em órbita. Contudo, para manter o satélite operacional, é necessário gerar energia. O perfil da produção de energia varia ao longo do ano e é profundamente dependente da órbita do CubeSat. Portanto, é crucial avaliar a produção de energia durante um longo período de modo a garantir a operação do satélite e ajudar a definir limites no design de sistemas e seleção de componentes. As restrições mencionadas acima fazem com que sejam usados magnetorquers como principais atuadores de atitude, os quais requerem um estudo do campo magnético da Terra de modo a comparar os torques gerados com os torques perturbativos inerentes do ambiente espacial. Outro cuidado a ter são os limites de temperatura dos componentes, assim, é necessário calcular as temperaturas experienciadas em órbita pelo satélite e decisões têm que ser tomadas para garantir o sucesso da missão. Tal como nas análises anteriores, o comportamento dinâmico do CubeSat sob condições de lançamento pode também definir a linha entre sucesso e fracasso. Este trabalho descreve os passos seguidos para simular todos os aspetos supracitados, para o tempo da missão estimado, de modo a minimizar os riscos associados e garantir o sucesso da missão do ORCA^{2}Sat, um CubeSat de duas unidades. Simulações foram feitas através de modelos de elementos finitos pertinentes e modelos computacionais do ambiente espacial, para um lançamento desde a Estação Espacial Internacional. Foi provado, através de uma abrangente análise da missão, que para os fatores críticos estudados a missão do ORCA^{2}Sat poder ser efetuada para o período de tempo desejado, mantendo o satélite operacional ao longo do seu tempo em órbita.

Palavras-chave

CubeSat, Análise da missão, Estação Espacial Internacional, Tempo de acesso, Sistema de energia, Campo magnético, Análise térmica, Análise dinâmica

Abstract

Mission planning of CubeSats can be very challenging due to their mass, volume and power constraints. In addition, the majority of CubeSat projects are done at a University level, which can also mean constraints in terms of budget. In order to guarantee the mission's success, several aspects must be studied prior to launch. Firstly, it must be assured that the satellite has enough accesses to the desired ground stations in order to establish communications while in orbit. However, to keep the satellite operational power generation is required. The profile of power generation varies throughout the year and is heavily dependent on the CubeSat's orbit. Thus, it is crucial to assess the power generation for a long period in order to guarantee the operation of the satellite and help set limits for systems design and hardware selection. The constraints mentioned above make use of magnetorquers as the main attitude actuators, which require a study of the Earth's magnetic field in order to compare the generated torques with the perturbative torques inherent to the space environment. Another concern are temperature limits of the components, therefore, the temperatures experienced by the satellite in orbit must be computed and decisions must be taken to allow for the mission's success. As in the previous analysis, the dynamic behavior of the CubeSat under launch conditions can also draw the line between success and failure. This work describes the steps taken in order to simulate all the aforementioned aspects for the computed mission lifetime, in order to mitigate inherent risks and guarantee mission success for ORCA^{2}Sat, a two unit CubeSat. The simulations were done through pertinent finite elements models and space environment computational models, for a deployment from the International Space Station. It was proved, with this comprehensive mission analysis, that for the studied critical factors ORCA^{2}Sat's mission can be accomplished for the desired period of time, keeping the satellite operational throughout its life in orbit.

Keywords

CubeSat, Mission analysis, International Space Station, Access time, Power system, Magnetic field, Thermal analysis, Dynamic analysis

Contents

Acknowledgments . . . v
Resumo . . . vii
Abstract . . . ix
List of Figures . . . xiv
List of Tables . . . xv
Nomenclature . . . xvii
List of Acronyms . . . xxi

1 Introduction **1**
1.1 Context . . . 1
1.2 ORCA^{2}Sat . . . 2
1.3 Literature Study . . . 3
1.4 Motivation and Goals . . . 4
1.5 Thesis Outline . . . 5

2 Theoretical Background **7**
2.1 Reference Frames . . . 7
2.1.1 Spacecraft Body Frame . . . 8
2.1.2 Geocentric Inertial Frame . . . 8
2.1.3 Earth-Centered/Earth-Fixed Frame . . . 8
2.1.4 Orbital Frame . . . 9
2.2 Power System . . . 9
2.2.1 Eclipse Phase . . . 9
2.2.2 Power Generation . . . 11
2.2.3 Power Storage . . . 12
2.3 Earth's Magnetic Field . . . 13
2.3.1 Attitude Determination and Control . . . 13
2.3.2 Orbital Impact . . . 14
2.4 Thermal Analysis . . . 15
2.4.1 Radiation . . . 15
2.4.2 Conduction . . . 19
2.4.3 Convection . . . 19
2.4.4 Internal Heat Generation . . . 19
2.4.5 Heat Balance . . . 19
2.4.6 Transient Thermal Analysis Simulation . . . 20
2.5 Dynamic Analysis . . . 20
2.5.1 Numerical Modal Analysis . . . 20
2.5.2 Experimental Modal Analysis . . . 23

3 Orbital Mechanics **25**
3.1 Orbital Elements . . . 25
3.2 Access Time . . . 27
3.3 Impact on Satellite's Subsystems . . . 29
3.3.1 Perturbative Forces . . . 29
3.3.2 Perturbative Torques . . . 32

4 ORCA^{2}Sat **35**
4.1 Mission . . . 35
4.1.1 ALTAIR Payload . . . 35
4.1.2 SFU Payload . . . 37
4.2 Requirements . . . 37
4.3 Structure Subsystems . . . 38
4.4 Electronic Subsystems . . . 39

5 Orbital Model **43**
5.1 Access Time . . . 43
5.2 Power Generation . . . 46
5.3 Magnetic Field . . . 50
5.4 Orbital Decay . . . 53

6 Thermal Analysis **55**
6.1 Finite Elements Analysis . . . 56
6.1.1 Structure Idealization . . . 56
6.1.2 Finite Elements Model . . . 56
6.1.3 Boundary Conditions and Loads . . . 59
6.2 Results . . . 59
6.3 Thermal Control System . . . 61

7 Dynamic Analysis **65**
7.1 Finite Elements Analysis . . . 65
7.1.1 Structure Idealization . . . 66
7.1.2 Finite Elements Model . . . 66
7.1.3 Boundary Conditions and Loads . . . 68
7.1.4 Results . . . 69
7.2 Experimental Modal Analysis . . . 70

8 Conclusions **73**
8.1 Overview . . . 73
8.2 Achievements . . . 74
8.3 Recommendations and Future Work . . . 74

Bibliography **77**

A FEM Solution Convergence Study **83**

B Thermal cycles for the different components **87**

List of Figures

1.1 Multiple units CubeSats [1]. 1

2.1 Relevant reference frames. Adapted from [2]. 7
2.2 Representation of the eclipse phase [3] 9
2.3 Variation of solar declination and right ascension throughout the year. Adapted from [4]. 10
2.4 Projection of surface area normal to the direction of radiation. Adapted from [5]. . 11
2.5 Solar Flux variation throughout a year. 16
2.6 View factor associated with radiation exchange between two surfaces [5]. 17

3.1 Illustration of the semi-latus rectum, p. Adapted from [6]. 26
3.2 Orbital elements. Adapted from [6]. 27
3.3 Azimuth and Elevation angles. Adapted from [7]. 28
3.4 Satellite to ground station geometry. Adapted from [8]. 29
3.5 Drag coefficients for different body geometries and altitudes [9]. 30
3.6 Types of spherical harmonics. Adapted from [10]. 32

4.1 ALTAIR payload with photodiodes from [11]. 36
4.2 Sequential operation of the ALTAIR payload. 36
4.3 Components of ORCA^{2}Sat's outer structure. 39
4.4 ADCS sensors [12–16]. 41
4.5 30% Triple Junction Solar Cell 3G30A. Adapted from [17]. 42
4.6 Deployment switches' mechanism. 42
4.7 ORCA^{2}Sat configuration without the radiator panel. 42

5.1 ORCA^{2}Sat ground tracking for one orbit. 44
5.2 STK 3D scenario. 44
5.3 Total number of accesses and respective total duration for each ground station in a year. 45
5.4 Two different flight attitudes respecting nadir pointing. 46
5.5 β angle variation in a year (September 2020 to September 2021). 47
5.6 Power generation for flight Attitude 1. 47
5.7 Power generation for flight Attitude 2. 47
5.8 Power budget over a year for Attitude 1. 49
5.9 Power budget over a year for Attitude 2. 49
5.10 Daily power generation comparison. 50
5.11 Earth's magnetic field intensity variation. 51
5.12 Torques generated by the magnetorquers. 52
5.13 Orbital decay of Flight Attitude 1. 54
5.14 Orbital decay of Flight Attitude 2. 54

6.1 Thermal Finite Elements Model. 58
6.2 Heat map for the different components' extreme temperatures. 60
6.3 Thermal behavior of batteries in both cases. 60

6.4 Heat map for the different components' extreme temperatures after black coating the structure. 62
6.5 Thermal behavior of batteries in both cases before and after applying TCS. 62
6.6 Minimum temperature on batteries' elements during Cold Case of a black structure. 63

7.1 Modal Finite Elements Models. 67
7.2 NRCSD Axial Cross-Section (+X view). Adapted from [18]. 68
7.3 First modes of vibrations of each FEM. 69
7.4 Accelerometers locations in *Homathko*. 70
7.5 Fundamental frequency taken from the measurement of the accelerometer **(4)**. . . 71

A.1 Thermal analysis convergence study. 84
A.2 Dynamic analysis convergence study. 85

B.-1 Thermal cycles for the different components. 89

List of Tables

2.1 Typical maximum power budget's range [19]. 11
2.2 Comparison of battery technologies [20] 12
2.3 Typical control modes for CubeSats. Adapted from [21]. 13
2.4 Sensors used in the ACDS. 13
2.5 Actuators used in the ADCS. 13
2.6 Bond albedo for different materials. Adapted from [22]. 17

4.1 Payloads and respective ground observatories. 35
4.2 Thermal and mechanical properties of selected alloys [5], [23], [24]. 38
4.3 Thermal and mechanical properties of FR-4 [25]. 39
4.4 Properties of each battery cell [26], [27]. 40
4.5 ADCS components with respective dimensions, mass and operating temperature range. 41
4.6 Mechanical, thermal and optical properties of each solar cell [17]. 41

5.1 ORCA^{2}Sat's orbital elements. 43
5.2 Number of accesses and respective total duration per month for each ground station. 45
5.3 Average accesses and each duration for the different ground stations. 45
5.4 Average and peak power generation for two flight attitudes. 48
5.5 ORCA^{2}Sat's systems power consumption. 48
5.6 Power system specifications. 48
5.7 Magnetorquers specifications with wire from [28]. 51
5.8 Perturbative torques range of values for a 2U CubeSat in ISS orbit. 52
5.9 Average values for the generated torques. 52
5.10 ORCA^{2}Sat parameters for orbital decay study. 53

6.1 Cold Case characteristics. 55
6.2 Hot Case characteristics. 56
6.3 2D meshes used in the thermal FEM model with properties from Table 4.6. 57
6.4 3D meshes used in the thermal FEM model. 57
6.5 Thermal-optical properties of different components. 58

7.1 1D meshes used in the modal FEM model. 67
7.2 2D meshes used in the modal FEM model. 67
7.3 3D meshes used in the modal FEM model. 67
7.4 Measured mass, FEM model components mass and change in density value to match values. 68
7.5 Number of elements and first natural frequencies of each dynamical FEM. 69

Nomenclature

Greek Letters

α	Absorptivity
α_{Sun}	Geocentric equatorial right ascension of the Sun
β	Angle between the orbital plane of the satellite and the vector to the Sun
δ_{Sun}	Geocentric equatorial right declination of the Sun
ε	Emissivity
ζ	Modal damp ratio
η	Efficiency
θ	Spacecraft's true anomaly
θ_S	Angle between the surface normal and the solar vector
λ	Longitude
μ	Earth's gravitational parameter
ν	Poisson's ratio
ρ	Density
ρ_s	Slant range between the satellite and the ground station
σ	Stefan-Boltzmann constant
τ	Satellite orbital period
ϕ	Latitude
φ	Phase angle
$\boldsymbol{\phi_v}$	Mode shape vector
$\boldsymbol{\omega}$	Angular velocity vector
ω	Argument of perigee
Ω	Right ascension of the ascending node
ϖ	Angular frequency
ϖ_d	Damped frequency

Roman Letters

$\mathbf{0}$	Null vector
a, $\ddot{\mathbf{x}}$	Orbit's semi-major axis
$\mathbf{a}$	Acceleration vector
A	Area
$\mathbf{A}_{\mathbf{a}}^{\mathbf{b}}$	Rotation matrix from frame $\mathbf{a}$ to $\mathbf{b}$
A_z	Azimuth
$\mathbf{B}$	Geomagnetic field vector
$\mathcal{B}$	Spacecraft body frame of reference
BA	Earth's bond albedo
$\mathbf{C}$	Damping matrix
C_D	Drag coefficient
C_r	Battery capacity
c_p	Specific heat capacity
$\mathbf{C_p}$	Heat capacity matrix

C_{SRP}	Solar radiation pressure coefficient
CTE	Coefficient of thermal expansion
e	Orbit's eccentricity
E	Young's modulus
$\hat{E}$	Eccentric anomaly
$\mathcal{E}$	Earth-Centered/Earth-Fixed frame of reference
E_l	Elevation
f	Natural frequency
$\mathbf{F}$	Force vector
F_i^j	View factor from surface i to surface j
G	Universal gravitational constant
$\mathbf{h}$	Angular momentum
$\mathbf{HL}$	Heat loads vector
i	Orbit's inclination
I	Electrical current intensity
$\mathbf{I}$	Identity matrix
$\mathcal{I}$	Geocentric Inertial frame of reference
$\mathbf{J}_{\mathcal{B}}$	Spacecraft's inertia matrix
k	Thermal conductivity
$\mathbf{K}_e$	Stiffness matrix
$\mathbf{K}_t$	Heat conduction matrix
$\mathbf{L}$	Torque vector
L_d	Solar panel life degradation
m	Mass
$\mathbf{m}$	Commanded magnetic dipole moment from magnetorquers vector
$\mathbf{M}$	Mass matrix
n	Mean anomaly
$\mathbf{n}$	Normal unit vector
$\mathcal{O}$	Orbital reference frame
p	Semi-lactus rectum
P	Power
$\mathcal{P}_{Sun}$	Pressure from solar radiation
q	Satellite electrical charge
$\dot{q}$	Heat flux
$\dot{\mathbf{q}}$	Heat flux vector
r	Distance between the satellite and Earth's center
$\mathbf{R}$	Radiation exchange matrix
$\mathcal{R}$	Ratio between the Earth's equatorial radius and the geocentric radius of the satellite
$R_{contact}$	Thermal contact resistance between two surfaces
$\mathbf{r}_{cp}$	Vector from the spacecraft's center of mass to the center of pressure
R_E	Earth's equatorial radius
S	Solar irradiance
$\hat{\mathbf{s}}$	Sun line-of-sight vector
t	Time
T	Temperature
$\mathbf{T}$	Temperature vector
$\dot{\mathbf{T}}$	Temperature change with time vector

t_e	Eclipse phase duration
U	Electrical potential difference
$\mathbf{v}$, $\dot{\mathbf{x}}$	Velocity vector
$\mathbf{x}$	Displacement vector

Subscripts

1, 2, 3	Local reference frame components
i, j	Computational indexes or Iteration number
x, y, z	Global reference frame components

Superscripts

T	Transpose

List of Acronyms

ADCS	Attitude Determination and Control System
ALTAIR	Airborne Laser for Telescopic Atmospheric Interference Reduction
BOL	Beginning of Life
CAD	Computer Aided Design
CAE	Computer Aided Engineering
CHIME	Canadian Hydrogen Intensity Mapping Experiment
COTS	Commercial-Off-The-Shelf
CSA	Canadian Space Agency
CSDC	Canadian Satellite Design Competition
DOD	Depth of Discharge
ECEF	Earth-Centered/Earth-Fixed frame of reference
EOL	End of Life
EPS	Electrical Power System
ESO	European Southern Observatory
FEM	Finite Elements Model
FFT	Fast Fourier Transform
FRF	Frequency Response Functions
GCI	Geocentric Inertial frame of reference
GMST	Greenwich Mean Sidereal Time
ISS	International Space Station
LED	Light Emitting Diode
LEO	Low Earth Orbit
LSST	Large Synoptic Survey Telescope
NRC	National Research Council
NRCSD	NanoRacks CubeSat Deployer
OBC	On-Board Computer
ORCA^{2}Sat	Optical and Radio Calibration of Atmospheric Attenuation CubeSat
Pan-STARRS	Panoramic Survey Telescope and Rapid Response System
PCB	Printed Circuit Board
RAAN	Right Ascension of the Ascending Node
SFU	Simon Fraser University
SRP	Solar Radiation Pressure
SSL	Space Systems Loral
STK	Systems Tool Kit
TCS	Thermal Control System
UBC	University of British Columbia
UT	Universal Time
UVic	University of Victoria
WMM	World Magnetic Model

Chapter 1

Introduction

Since the beginning of the *Homo Sapiens Sapiens* dominion over the planet, humans have dreamed about spaceflight. That desire led to, on October 4^{th} of 1957, the launch of the first artificial satellite: the Russian *Sputnik 1*. Since then, space exploration has taken a huge step and witnessed an exponential growth and we reached a point where we already know, as humans, we will not remain bounded to Earth until the end of humankind.

1.1 Context

Even though we might not realize it, satellites play an important role in our daily lives. Year after year the use of satellites for either commercial, scientific or military purposes has been rising. Space-based observations have transformed our understanding of Earth, its environment, the solar system and the universe at large. Compared to ground-based (or even airborne) measurements, space-based ones cover larger areas with a relatively high temporal resolution.
Depending on their mass satellites can be sorted into different classifications but for the purpose of this thesis we will only focus on small satellites. Small satellites, or smallsats, are satellites ranging in mass between 500 kg to 0.1 kg - from microsatellites (100 kg to 10 kg), nanosatellites (10 kg to 1 kg) and even picosatellites (1 kg to 0.1 kg) [29]. These smallsats provide means to answer specific science questions in a rapidly and more affordable manner.
Regarding nanosatellites, Stanford University in collaboration with California Polytechnic State University, introduced to the world the CubeSat [30]. According to [31], the purpose of the project is to provide standards in nanosatellites' design in order to reduce costs and development time while increasing accessibility to space: achieve more with less.
CubeSats are measured in units called *U's*. Each *U* consists of a 10 cm cube with a mass up to 1.33 kg. As represented in Figure 1.1 CubeSats can be formed by combining several *U's*, each respecting the original volume and mass constraint.

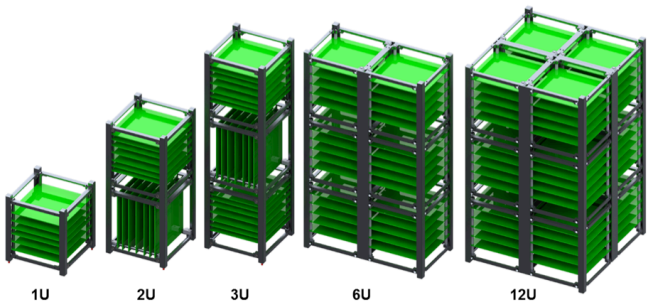

Figure 1.1: Multiple units CubeSats [1].

Historically, CubeSats were developed as training projects to expose students to the challenges of real-world engineering practices and system design. Yet, in less than a decade Cubesats evolved from purely educational tools to a standard platform for technology demonstration and scientific instrumentation. Mainly due to the use of Commercial-Off-The-Shelf (COTS) components and

the ongoing miniaturization of several technologies, Cubesats find applications, amongst others, in environmental monitoring, physics and biological sciences, communications and agriculture [32].
From this outline, it becomes evident that CubeSats are subjected to strict mass, volume, power and cost constraints. Such limitations should be addressed throughout the entire project. For starters, the orbit selection should concern several studies like the power generation, Earth's magnetic field variation, thermal impact and de-orbiting strategy.
In this thesis these studies are performed regarding ORCA^{2}Sat and it's launch from the International Space Station (ISS). ORCA^{2}Sat is idealized through an international partnership, led by University of Victoria (UVic) in collaboration with Simon Fraser University (SFU), University of British Columbia (UBC), Technical University of Lisbon, Harvard University, Space Systems Loral (SSL) and the National Research Council (NRC).

1.2 ORCA^{2}Sat

As said before CubeSats were developed with an academic purpose but soon those boundaries were surpassed. Their potential to perform more complex missions with scientific and technological interest on a small budget is very appealing to several industries. Thus, CubeSat design competitions started to emerge all around the globe aiming specific goals in diversed areas of study. One of those competitions is the Canadian Satellite Design Challenge (CSDC) [33] in which UVic already proved its worth and capabilities in designing an entire CubeSat and its mission. Based on the experience of the collaborative members referred in the previous section, and due to the multidisciplinary nature of their team members, the ORCA^{2}Sat project was born: Optical and Radio Calibration of Atmospheric Attenuation CubeSat.
The CubeSat is being developed under a contest held by the Canadian Space Agency (CSA), termed *Canadian CubeSat Project*, which aims to increase student's interest and develop their expertise in space domains and give hands-on experience in order to prepare students to enter the job market [34]. Thus, each collaborative teams were granted both funds and workshops provided by the CSA in order to get a flight-ready CubeSat by the end of 2020.
According to [35], ORCA^{2}Sat will represent the British Columbia province and aims to develop and test new advancements in technology to better understand "dark energy", an enigmatic form of energy making up 75% of the universe, believed to cause its expansion at an accelerating rate. Operating with two payloads, ORCA^{2}Sat will calibrate a number of both optical and radio observatories in an effort to reduce uncertainties associated with measurements of the universal expansion rate. These calibrated measurements may provide new insights into the nature of dark energy and the universal expansion rate.
For calibration of ground-based telescopes, one of the main techniques is photometric calibration using standard stars in the sky [36]. However, such approach is subject to several uncertainties like atmospheric extintion: the reduction in a celestial object's apparent brightness when its light passes through the atmosphere. According to professor Justin Albert [37], in order to calibrate groud-based telescopes, one could use dedicated visible light sources aboard satellites. In fact, photometric calibration can even be used in satellites for self-calibration purposes (*e.g.* Hubble Space Telescope [38]). By using an orbiting lamp for calibration, the majority of uncertainties lies in the difference between the onboard-monitored output and the ground-observed output. Both Light Emitting Diodes (LED) and laser lights have the benefit of being monochromatic, allowing for calibration of individual wavelengths. Therefore, an entire spectrum could be calibrated, removing the significant inherent uncertainties associated with comparing the spectra of astrophysical objects

with the spectrum of a calibration lamp [37].
Based on what was exposed in the previous paragraphs, ORCA^{2}Sat is a 2U CubeSat tasked with:

1. Supplying the Canadian Hydrogen Intensity Mapping Experiment (CHIME) observatory with valuable data by calibrating its observation antenna and characterizing the CHIME antenna via a consistent radio source on board the satellite;

2. Providing precise optical calibrations to the world's optical observatories through the novel technique of a visible known light source in Low Earth Orbit (LEO);

3. Making use of a reference light source for calibrating a network of Canadian star-photometers, enabling researchers to estimate night time optical depth and the presence of atmospheric aerosols at night more accurately.

1.3 Literature Study

As already stated, CubeSats have several restraints in terms of power, mass and volume. In addition, since the majority of CubeSats projects are from university groups, there are also budget constraints. Thus, several procedures have been studied in order to guarantee the mission's success even under said limitations.
As stated in [39], approximately 85% of all nanosatellites are equipped with solar panels in conjunction with rechargeable batteries. However, the power generation is strongly related to the orbit characteristics and the space environment itself, as shall be seen in the following chapters. Some techniques were tested in order to maximize power generation. In [40] and [41], the potential use of supercapacitors in the aerospace industry was assessed and it was concluded that the use of supercapacitors to power just a specific component during eclipse, specially ones with large spikes of power, is capable of extending greatly battery life. To increase power generation, it was assessed in [42], that using deployable panels increased the mean power generation in more than two times. Also, in the same source, by using small triangular solar cells, allowed to assemble a solar panel with a high number of cells, which can be used for more advanced interconnections of cells into several independent branches to avoid power generation failure from all cells on the same panel. A study of the feasibility of using thermoelectric generators for energy harvesting applications in CubeSats was conducted in [43], which produce a power output in the presence of a temperature difference. It was concluded that for CubeSats in LEO the efficiency of these devices falls below 1% due to low temperature gradients. A Fresnel lens technique was tested in [44], where lenses installed at the edge of the solar panels enhance power generation performance by concentrating and illuminating solar energy onto the solar panels. Such methodology increased the power generation in almost 35%.
In order to keep the components within safe temperature values the use of coat paintings and small heaters is widely known. A computational method which computes the critical segments of a surface that require coatings in order to keep subsystems safe was developed in [45]. The application of heaters in conjunction with multilayer insulation, to reduce excessive thermal flux from and to the components, proved to increase battery temperature in more than 5 °C [46]. An active thermal control system for small spacecraft was achieved in a practical and lightweight structure by circulating a coolant through embedded micro-vascular channels in deployable composite panels. The novel technique, detailed in [47], used a technique which allows miniature channels to be formed in structures made from composite materials through the use of a proprietary polymer which is embedded in the composite structure. After curing the composite, the polymer is removed through

a vaporization process and a void is left where the polymer used to be. Using this technique, complex networks of microvasculature can be embedded in composite radiator panels through which gases or liquids may be circulated. Other techniques for passive temperature control can be applied. The addition of lateral plates built from a material with high thermal inertia could be used in an effort to reduce the temperature gradients experienced by the different components, like it is presented in [64].
Shields are often used to protect the spacecraft from damaging radiations and are important for longer missions. A novel radiation shielding material is detailed in [48]. By layering metal materials it is possible to significantly reduce the effect of charging particles, thus, extending the effective life of typical CubeSat components.

1.4 Motivation and Goals

The space industry has suffered a huge growth in the past years and the tendency is to keep its development. The benefits are no longer just scientific or military. Space applications are able to develop new technologies which can improve life on Earth and predict crisis or help during them. Therefore, it is important to motivate younger people to pursue a path in the industry and acquire the skills so that innovation may take place.
The concept of CubeSats allowed for the development of space missions and to test new technologies for a small price. However, such missions are very constrained not only in terms of power, mass and volume but also on their orbits due to launch in piggyback as secondary payload. This thesis is result of some of the work that consists the process of mission analysis for CubeSats. Since the payloads are going to be tested in harsh conditions, the failure probability needs to be reduced to a minimum. Besides guarantying that the CubeSat has sufficient contact with the ground, it also studies the impact of the space environment on the satellite's subsystems for the mission lifetime in orbit. It includes studies related to power availability, magnetic field variation for active control, thermal impact on the systems and dynamic behavior in launch conditions for a deployment from the ISS. The studies, which aim to guarantee the mission's success, can be used for future mission planning of CubeSats under the same orbit conditions. This way, the goals of this master's thesis are summarized as follows:

I. Evaluate if the access time to the different ground observatories is enough to test the feasibility of the payloads;

II. Guarantee that the power generated is enough to keep the satellite operational through its mission even during worst case conditions;

III. Assess if the Earth's magnetic field is enough to be used to generate control torques capable of surpassing perturbative torques inherents of LEO environment;

IV. Predict the duration of the mission in order to design robust enough systems and maximize the payloads operation time;

V. Study the thermal impact of LEO environment and apply, if needed, changes in order to keep components within safe temperature values even during worst case conditions;

VI. Guarantee an adequate dynamic response from the structure to launching conditions in order to keep the integrity of the satellite before it becomes operating in orbit, applying changes as needed;

VII. Mitigate the risk of mission failure.

Goals I to VI lead, in their essence, to Goal VII. The development of the work in the scope of ORCA^{2}Sat shall ultimately give an answer to the question if whether or not the mission is feasible under a tight budget.

1.5 Thesis Outline

The structure of this thesis is mapped as follows:

Chapter 2 includes relevant concepts of the theoretical background for the current research. It includes a brief explanation of the different frames of reference used throughout the different analysis, followed by the impact of the space environment regarding power generation and use and the effect of the Earth's magnetic field. Theory regarding both thermal and modal analysis is also discretized in this chapter.

Chapter 3 characterizes the satellite's orbit. Besides presenting a description on how to define the orbital motion it also focus on how the access time to ground stations is affected and in the perturbative forces inherent to the orbit itself.

Chapter 4 provides an overview of ORCA^{2}Sat, namely its mission and correspondent payloads, the requirements its design is subjected to and the current configuration both in terms of structure and internal components.

Chapter 5 describes how orbit inherent from the launch impacts the access time to the different ground stations, the power generation, the control generated by manipulating Earth's magnetic field and the mission lifetime due to perturbations.

Chapter 6 provides the development of the thermal analysis from setting the simulation and the how the results affected the development of a thermal control system.

Chapter 7 details the evolution of the simulations used to compute the fundamental frequency of the satellite. The results are compared to experimental testing done to another CubeSat model.

Chapter 8 recaps the work performed with a conclusion and achievements while providing recommendations for future work.

Chapter 2

Theoretical Background

In this chapter, a brief explanation regarding several important aspects of a CubeSat mission are discussed. An overview of the relevant reference frames is presented in Section 2.1. Section 2.2 deals with the power generation techniques for CubeSats. In Section 2.3 are presented concepts about magnetic attitude control, the method chosen for ORCA^{2}Sat. Section 2.4 refers to the thermal study and, lastly, Section 2.5 deals with the basis of a dynamic analysis.
Due to the complexity of the environment and the structure to be analyzed one must resort to modern Computer Aided Engineering (CAE) software. In order to achieve accurate results and interpret them the user must understand what is behind the user interface and which type of results are produced. Thus, this chapter presents relevant theoretical background and state of the art techniques which will be the base of future decision making throughout the thesis.

2.1 Reference Frames

In the aerospace field, attitude can be defined as the orientation of a rigid spacecraft relative to a certain reference frame. Several reference frames in three dimensions are of special interest for attitude analysis and the most relevant ones for this work will be addressed in this section.
Generally speaking a reference frame is specified by the location of its origin and the orientation of its coordinate axes [10]. The reference frames used throughout this thesis are represented in Figure 2.1 and discussed in the following subsections.

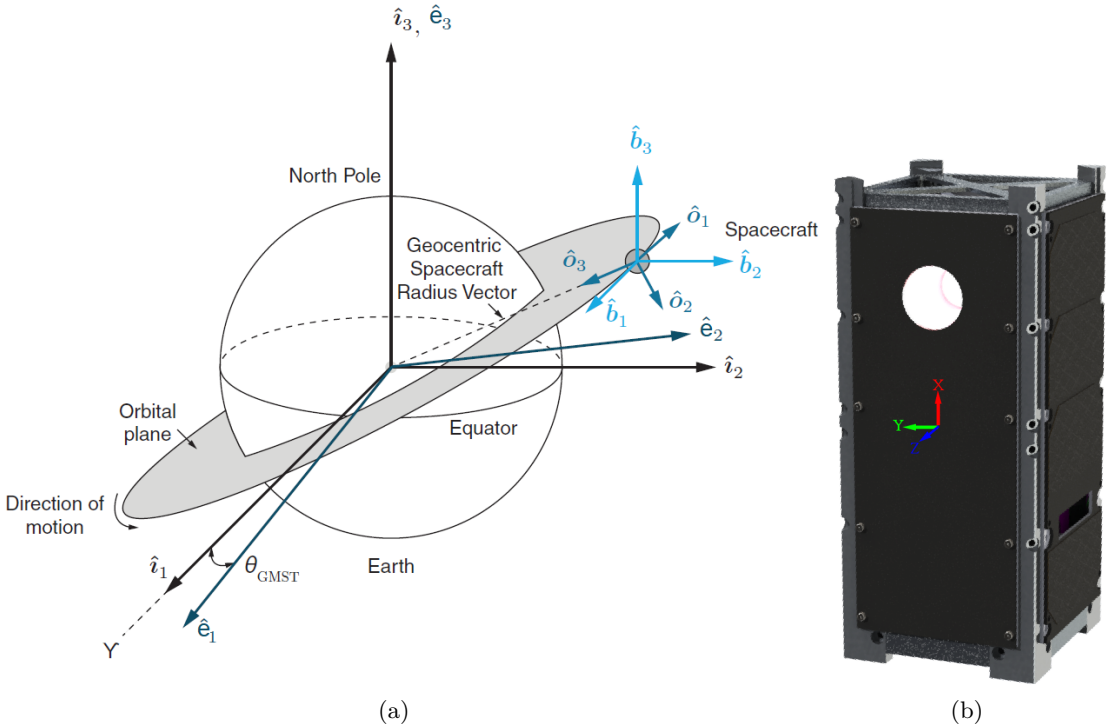

(a) (b)

Figure 2.1: Relevant reference frames. Adapted from [2].

2.1.1 Spacecraft Body Frame

A spacecraft body frame is defined by an origin at a specified point in the spacecraft body and three Cartesian axes [10]. Due to the possibility of components shifting (*e.g.* thermal deformation), is quite common to define this frame as the orientation of some sufficiently rigid navigation base. The spacecraft body frame is defines by $\mathcal{B} = \{\hat{b}_1, \hat{b}_2, \hat{b}_3\}$. For ORCA^{2}Sat the origin is the center of mass obtained from the Computer Aided Design (CAD) model and the axes rotate with it. The orientation defined points $\hat{b}_3$ in the *nadir* direction (along the direction of the integrating sphere output port), $\hat{b}_1$ is normal to the end caps and points from the base to the top of the satellite and $\hat{b}_2$ completes the right-handed triad, as illustrated in Figure 2.1b.

2.1.2 Geocentric Inertial Frame

An inertial reference frame is a frame in which Newton's laws of motion are valid. According to [49], inertial frames are any reference frames that move at constant velocity, and without rotation, relative to frames in which the universe appears spherically symmetric. Bearing this in mind, is reasonable to consider a celestial reference frame with its axes fixed relative to a distant "fixed" star as an inertial frame.

The Geocentric Inertial (GCI) frame is an approximate inertial frame with its origin at the center of mass of the Earth. Its z axis is aligned with the Earth's North pole, the x axis coincides with the *Vernal Equinox*[1] and the y axis completes the right-handed triad. Albeit, neither the polar axis nor the orbit plane are inertially fixed. To overcome this problem the axes are defined as mean values of the pole and *Vernal Equinox* at a designated epoch time [10]. The most commonly used GCI frame considers the current standard epoch, J2000, with positions referents to January 1^{st} of 2000 at 12:00 Terrestrial Time. This reference frame is denoted by $\mathcal{I} = \{\hat{i}_1, \hat{i}_2, \hat{i}_3\}$ where $\hat{i}_1$ is aligned with the *Vernal Equinox* direction, $\hat{i}_3$ coincides with the Earth's North Pole and $\hat{i}_2$ completes the right-handed system.

2.1.3 Earth-Centered/Earth-Fixed Frame

Contrary to the GCI frame, the Earth-Centered/Earth-Fixed (ECEF) frame rotates with the Earth. This frame is designated by $\mathcal{E} = \{\hat{e}_1, \hat{e}_2, \hat{e}_3\}$ where $\hat{i}_3 = \hat{e}_3$, $\hat{e}_1$ points in the direction of the Earth's prime meridian $\hat{e}_2$ completes the right-handed triad. The angle between $\hat{i}_1$ and $\hat{e}_1$ is called Greenwich Mean Sidereal Time (GMST) angle and is denoted by θ_{GMST} [10].

The θ_{GMST} angle, in degrees, is given by:

$$\theta_{GMST} = 100.4606184 + 36000.77004T_0 + 0.387933 \times 10^3 T_0^2 - 0.2583 \times 10^{-9} T_0^3 + 15.041068635\, UT \tag{2.1}$$

where UT is the Universal Time in hours, determined by the Sun's passage across the Greenwich meridian, and T_0 is the number of Julian centuries elapsed from the J2000 epoch [6]. It is possible for the computed value of θ_{GMST} to exceed 360º. If so, it must be reduced to within that limit by adding or subtracting the appropriate integer multiple of 360º.

[1] Intersection of the Earth's equatorial plane with the plane of the Earth's orbit around the Sun, in the direction of the Sun's position relative to the Earth on the first day of spring. Denoted by γ in Figure Figure 2.1

2.1.4 Orbital Frame

This frame, also denoted by Local-Vertical/Local-Horizontal (LVLH), is designated by $\mathcal{O} = \{\hat{o}_1, \hat{o}_2, \hat{o}_3\}$ and is particularly useful for Earth-pointing spacecrafts. Attached to its orbit, $\hat{o}_3$ points along the nadir vector towards the center of the Earth, the $\hat{o}_2$ is aligned with the negative orbital plane normal and $\hat{o}_1$ completes the right-handed triad.

2.2 Power System

Satellite power requirement is a crucial parameter for its in-orbit operation. The Electrical Power System (EPS) provides, stores, distributes and controls the spacecraft electrical power [21]. As shall be seen in Chapter 3, the orbital parameters are deemed to affect the determination of the satellite power profile. In order to sustain its life in space, and assure the mission is accomplished, ORCA^{2}Sat needs to fulfill its power requirements.

2.2.1 Eclipse Phase

Typical satellites use photovoltaic cells to generate electric power. Thus, its exposure to sunlight plays a crucial role. Regarding this matter, the satellite is either exposed to sunlight or in eclipse phase. As per Figure 2.2 a satellite can either be in partial eclipse, penumbra, or total eclipse, umbra. Reasonably, when the satellite is in umbra, there is no power generation, making the power profile dictated by the satellite's position.

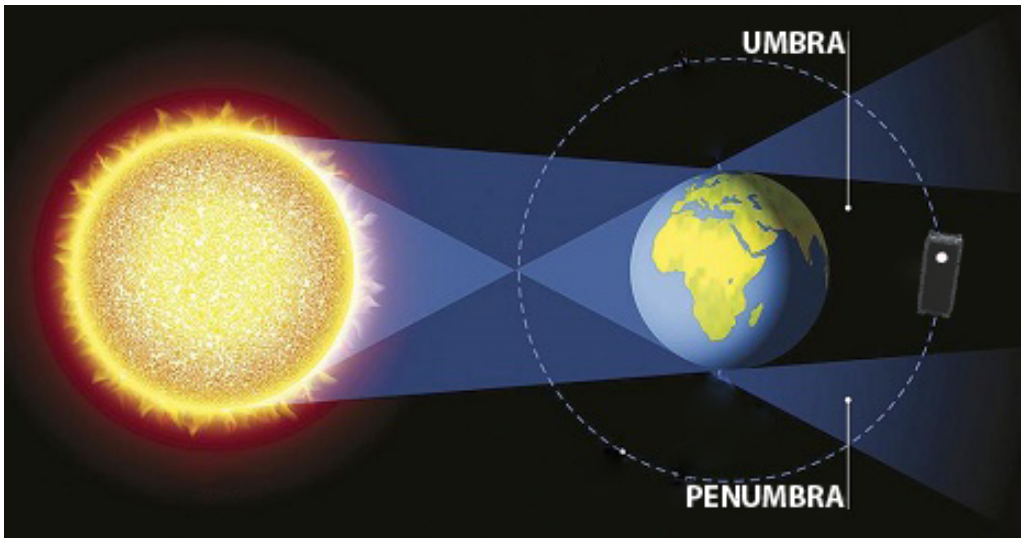

Figure 2.2: Representation of the eclipse phase [3]

An estimation of the eclipse phase duration can be obtained with Eq. (2.2):

$$t_e = \frac{\tau}{\pi} \cos^{-1}\left(\frac{\sqrt{1-\mathcal{R}^2}}{\cos\beta}\right) \tag{2.2}$$

where $\mathcal{R}$ is the ratio between the Earth's equatorial radius, R_E with a value of 6378 km [6], and the geocentric radius of the satellite[2], r, τ is the orbital period of the spacecraft and β is the angle between the geocentric unit position vector to the Sun and the satellite's orbit plane [19].

[2]Satellite's radius variation is presented in Chapter 3.

The orbital period, for an elliptical orbit, can be calculated by recurring to the following equation:

$$\tau = \frac{2\pi}{\sqrt{\mu}} a^{\frac{3}{2}} \tag{2.3}$$

where a is the orbit's semi-major axis (see Chapter 3) and μ is the Earth's gravitational parameter which is equal to $398600\,km^3/s^2$ [6].

In order to calculate the β angle Eq. (2.4) can be used:

$$\beta = \sin^{-1}(\mathbf{r_{sun}} \cdot \mathbf{h_{sat}}) \tag{2.4}$$

where $\mathbf{r_{sun}}$ and $\mathbf{h_{sat}}$ are, respectively, the geocentric unit position vector of the Sun and the unit angular momentum vector of the satellite:

$$\mathbf{r_{sun}} = [\cos\delta_{sun}\cos\alpha_{sun} \quad \cos\delta_{sun}\sin\alpha_{sun} \quad \sin\delta_{sun}]^T \tag{2.5a}$$

$$\mathbf{h_{sat}} = [\sin\Omega\sin i \quad -\cos\Omega\sin i \quad \cos i]^T \tag{2.5b}$$

where α_{sun} is the geocentric equatorial right ascension of the Sun, δ_{sun} is the geocentric equatorial right declination of the Sun [19] and Ω and i are, respectively, the satellite's orbit right ascension of the ascending node and inclination (refer to Chapter 3). According to [4], α_{sun} is the angle measured positively eastward along the celestial equator to the meridional plane which passes through the Sun and δ_{sun} is measured positively northward from the celestial equator. Using more intuitive terms, α_{sun} can be perceived as the counterpart of terrestrial longitude and δ_{sun} as the counterpart of geocentric latitude. Both angles vary throughout the year as is illustrated in Figure 2.3.

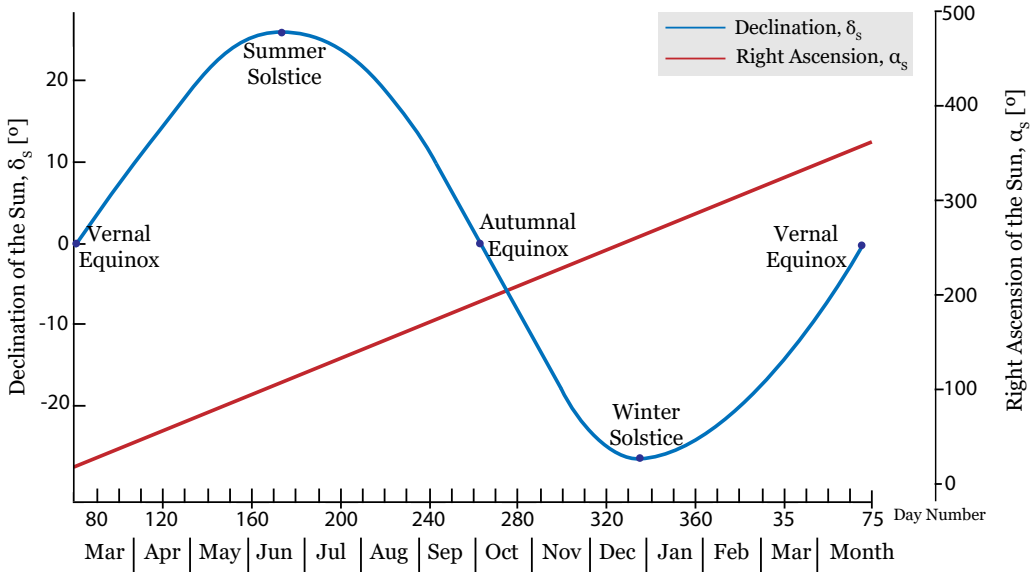

Figure 2.3: Variation of solar declination and right ascension throughout the year. Adapted from [4].

2.2.2 Power Generation

A CubeSat power budget defines the maximum combined power consumption of all the subsystems based on the satellite's total power generation. A positive power budget means that there is available energy to charge the batteries while a negative power budget means there isn't enough energy supplied to recharge the batteries to 100% in a single orbit. Table 2.1 sumarizes the maximum power budget range for typical CubeSats without deployable solar panels (*i.e.* only solar panels on the satellite's faces).

Table 2.1: Typical maximum power budget's range [19].

CubeSat type	**Power range [W]**
1U	1 - 2.5
2U	2 - 5
3U	7 - 20

The power output from the panels can be calculated with Eq.(2.6)

$$P = \eta_{sp}\, S\, A \cos\theta_S \tag{2.6}$$

where η_{sp} is the solar panel efficiency, S is the Solar Irradiance, A is the solar panel's surface area and θ_S is the angle between the surface normal and the solar vector in the spacecraft body frame [50], as can be seen in Figure 2.4.

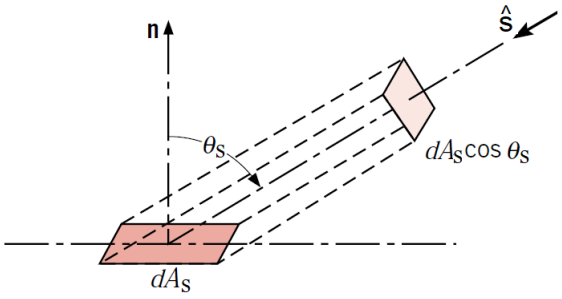

Figure 2.4: Projection of surface area normal to the direction of radiation. Adapted from [5].

According to [51], new studies show that the Solar Irradiance has a range of $1360.8 \pm 0.5\, Wm^{-2}$, lower than the precious value of $1365.4 \pm 1.3\, Wm^{-2}$. Although not as strong as sunlight, other sources of radiation include the Earth's *Albedo* and infrared radiation. Due to lower magnitude and adding to the fact that there isn't any solar panels on $ORCA^2Sat$'s Earth facing face we can neglect the *Albedo* contribution in power generation [52]. However, it plays a more important role regarding the thermal analysis, as shall be seen ahead in section 2.4.
One important aspect about Eq.(2.6) is the efficiency η_{sp} which, due to material degradation, can decrease throughout the mission [53]. Thus distinction between Beginning of Life (BOL) and End of Life (EOL) should be made. Considering that Eq.(2.6) refers to BOL efficiency, in order to calculate the power generated for EOL, one needs to consider the life degradation L_d. Power generation can decrease as much as $3\%/year$ for triple junction solar cells [54]. Hence, the life degradation can be estimated by:

$$L_d = (1 - degradation/year)^{satellite\ life} \tag{2.7}$$

Thus, power generation at BOL and EOL can be obtained, respectively:

$$P_{BOL} = \eta_{sp}\, S\, A \cos\theta_S \tag{2.8a}$$

$$P_{EOL} = L_d \times P_{BOL} \tag{2.8b}$$

2.2.3 Power Storage

Due to size constraints, the power generated by CubeSats is very limited, making imperative the use of energy storage methods. In fact, any spacecraft that uses photovoltaic cells as a power source requires a system to store energy for peak-power demands eclipse periods [21]. Once again, size restrictions in nanosatellites, dictates the need for rechargeable batteries (secondary batteries) in order to fulfill energy storage requirements. Secondary batteries include nickel-cadmium (NiCd), nickel-hydrogen (NiH_2), lithium-ion (Li-ion) and lithium polymer (Li-po), all which have been extensively used in CubeSats. The relevant properties of said batteries can be found in Table 2.2.

Table 2.2: Comparison of battery technologies [20]

	Battery chemistry			
	$NiCd$	NiH_2	$Li-ion$	$Li-po$
Discharge terminate voltage [V]	1.00	1.25	2.80	2.80
Charge terminate voltage [V]	1.55	1.55	4.20	4.20
Nominal discharge voltage [V]	1.25	1.25	3.70	3.70
Operational temperature [°C]	[-20;50]	[-20;30]	[-20;60]	[-20;60]
Sensitivity to overcharging	Medium	Very Low	Very High	Very High
Gravimetric energy [Wh/kg]	40-60	50-80	100-200	130-250
Volumetric energy [Wh/L]	50-150	60-180	150-250	150-300
Gravimetric power [W/kg]	150-200	200-270	200-500	>1000
Self-discharge [%/day]	1	10	0.3	0.3

From Table 2.2 is easy to conclude that Li-po batteries are more attractive to use in CubeSats. Their high values of both volumetric and gravimetric energy reduces, respectively, the space and mass needed to achieve a specific amount of energy. Considering the growing use of CubeSats, it's understandable that Li-po batteries are undergoing some improvements in order to make their use more safe over Li-ion batteries [55].

Battery capacity indicates the amount of energy the battery can store. Due to voltage variation throughout charging and discharging cycles, the common unit for capacity is Ah or mAh defined as the number of hours for which a battery can provide a current equal to the discharge rate at the nominal voltage of the battery. Dividing Eq.(2.9) by the bus voltage, one can obtain the battery capacity, C_r, in $Ah/battery$:

$$C_r = \frac{P_e\, t_e}{(DOD)\, N\, n} \tag{2.9}$$

where P_e is the average power required during eclipse, DOD is the Depth of Discharge, N is the number of batteries and n is the battery-to-load transmission efficiency. For the majority of batteries, they cannot be fully discharged without causing serious, and often irreparable, damage to the battery. Thus, the DOD of a battery determines the fraction of power that can be withdrawn from the battery and higher values imply shorter cycle life [21].

2.3 Earth's Magnetic Field

LEO satellites, due to their proximity to Earth, experience significant effects of its magnetic field. The geomagnetic field varies in time, height and coordinates having a mean surface value of 45 000 nT [56]. In order to study of its effect, the geomagnetic field is widely modeled as spherical harmonic model, as shall be seen in Section 3.3.2. As shall be seen in the following subsections, the geomagnetic field presence can be used to determine and control the satellite's attitude and can have an impact on the orbital motion.

2.3.1 Attitude Determination and Control

The Attitude Determination and Control System (ADCS) stabilizes the satellite and orients it in the desired direction throughout the mission despite the effect of external disturbance torques. In order to achieve stabilization, the external disturbances must be resisted by either external control torques or internal storage of the resulting momentum buildup without reorienting the spacecraft beyond it allowable limits [21].
The ADCS requirements are deeply connected to the mission needs and subsystems characteristics, which may vary considerably throughout different phases. Thus, is of extreme importance to define control modes. Table 2.3 shows the typical control modes for CubeSats.

Table 2.3: Typical control modes for CubeSats. Adapted from [21].

Control Mode	**Description**
Detumbling	Characterized by high angular rate of the satellite, usual after deployment.
Tracking	Used for the vast majority of the mission. Requirements for this mode should drive system design.
Pointing	When the spacecraft is required to point to *Nadir*, *e.g.*, point camera to specific region in Earth imaging missions.
Safe	Used in emergencies if regular mode fails or is disabled. May use less power or sacrifice normal operation to meet power or thermal constraints.

The ADCS make uses of two types of components: the sensors and the actuators. The former, listed in Table 2.4, measures the position of the satellite's center of mass while the latter, showed in Table 2.5, acquires or maintains a desired attitude.

Table 2.4: Sensors used in the ACDS.

Sensors					
Magnetometer	Sun Sensor	Earth Sensor	Star Tracker	GPS Receiver	Gyroscope

Table 2.5: Actuators used in the ADCS.

Actuators			
Magnetorquer	Reaction Wheel	Propulsion	Gravity Gradient Boom

Due to the content of this Thesis regarding ORCA^{2}Sat, here are only detailed the components affected by the geomagnetic field: magnetorquer and magnetometer. However, all the components of the ADCS are referred in Chapter 4.
Magnetic torquers use the Earth's magnetic field to produce a torque. Magnetic control torques have several advantages for near-Earth missions, including smoothness of application, essentially unlimited mission life (due to the absence of expendables), and absence of catastrophic failure

modes [57]. As described in Section 3.3.2, the magnitude of the field decreases as the inverse exponent of the distance from the center of the Earth. Thus, the magnetic torque will be several orders of magnitude smaller at high-Earth orbits, such as geosynchronous orbits, than at low-Earth orbits.

Another issue is that the torques are constrained to lie in a two-dimensional plane orthogonal to the magnetic field, so only two out of three axes can be controlled at a given time instant [10]. However, full three-axis control is available provided that the spacecraft's orbital plane does not coincide with the geomagnetic equatorial plane and does not contain the magnetic poles [58]. The torque generated by the magnetic torquers is given by:

$$\mathbf{L}_{mag} = \mathbf{m} \times \mathbf{B} \tag{2.10}$$

where $\mathbf{m}$ is the commanded magnetic dipole moment generated by the torquers, given by:

$$\mathbf{m} = \frac{k}{||\mathbf{B}||^2}\, \omega \times \mathbf{B} \tag{2.11}$$

where $\mathbf{B}$ is the local geomagnetic field expressed in body-frame coordinates, k is a positive scalar gain and ω is the angular velocity.

Activating a torquer aligned with a spacecraft's spin axis will cause it to precess about the direction of the magnetic field, when the field has a component that is perpendicular to the spin axis.

Most spacecraft magnetometers are fluxgate magnetometers, which are relatively small, lightweight, rugged, inexpensive, have no moving parts and do not require a clear field of view. However, they do require a well-modeled magnetic field if they are to be used as attitude sensors, which can compromise their use in LEO [10].

Magnetometers measure the sum of the ambient field that is of interest and any local fields produced by the spacecraft, *e.g.*, ferromagnetic materials or by current loops in attitude control torquers. If the local fields are known, they can be compensated for. If they are not known, the magnetometers can be located far from the sources of magnetic contamination, which can be challenging in a CubeSat.

2.3.2 Orbital Impact

The disturbing force due to the magnetic field in a satellite have the form

$$\mathbf{F}_B = q\mathbf{v}_O \times \mathbf{B} \tag{2.12}$$

where $\mathbf{v}_O$ is the satellite's velocity in the orbital frame of reference and q is the satellite's electrical

charge. According to [56], the variation in the orbital elements due to $\mathbf{F}_B$ is:

$$\frac{\partial a}{\partial t} = \frac{2e\sin\theta}{n\sqrt{1-e^2}}F_{B_1} + \frac{p}{r}F_{B_2} \tag{2.13a}$$

$$\frac{\partial e}{\partial t} = \frac{\sqrt{1-e^2}}{n\,a}[\sin\theta F_{B_1} + (\cos\theta + \cos\hat{E})F_{B_2}] \tag{2.13b}$$

$$\frac{\partial i}{\partial t} = \frac{r\cos(\theta+\omega)}{n\,a^2\sin i\sqrt{1-e^2}}F_{B_3} \tag{2.13c}$$

$$\frac{\partial \Omega}{\partial t} = \frac{r\sin(\cos+\omega)}{n\,a^2\sin i\sqrt{1-e^2}}F_{B_3} \tag{2.13d}$$

$$\frac{\partial \omega}{\partial t} = -\cos i\frac{\partial \Omega}{\partial t} + \frac{\sqrt{1-e^2}}{n\,a\,e}\Big[-cos\theta F_{B_1} + \Big(1+\frac{r}{p}\Big)\sin\theta F_{B_2}\Big] \tag{2.13e}$$

where n, p, $\hat{E}$ are the satellite's mean motion, the orbit's semi-latus rectum and eccentric anomaly, respectively, and a, e, i, Ω and ω are orbital elements. Such variables are detailed in Chapter 3.

2.4 Thermal Analysis

A complete thermal analysis on picosatellites is of most importance because it helps in the development of thermal control system that can protect the satellite's internal systems from the extreme condition of space.
In satellites, several processes of heat transfer are combined and the boundary conditions are time varying which require transient analysis to correctly predict the structures response. The different types of heat sources are sorted by the category they fit in and are listed below.

2.4.1 Radiation

Radiation results from the loss of internal energy in order to achieve thermal equilibrium with surrounding environment. This mode of heat transfer does not require matter to propagate and the three main sources are: solar radiation, Earth's albedo and radiation from Earth. When considering individually components of the satellite they too receive radiation from and irradiate to the surroundings.

Solar Radiation

The solar flux that reaches a satellite depends of the total emissive power of the Sun, which, considering the Sun as a black body[3], can be estimated by the Stefan-Boltzmann Law:

$$\dot{q}_{solar} = \sigma T_s^4 \tag{2.14}$$

where T_s is the Sun's effective temperature and σ is the Stefan-Boltzmann constant with a value of $5.6697 \times 10^{-8}\,\mathrm{W\,m^{-2}\,K^{-4}}$. The effective temperature of a body is the temperature of a black body that would allow to emit the same total amount of electromagnetic radiation [5]. In order to compute the total heat transfer rate emitted by the Sun, the heat flux emitted is multiplied by the Sun's surface area, idealized as a sphere of radius $r_s = 6.957 \times 10^8\,\mathrm{m}$:

[3] A black body is an idealized physical body that absorbs all incident electromagnetic radiation, regardless of frequency or angle of incidence [5].

$$\dot{Q}_{solar} = \dot{q}_{solar} \times 4\pi r_s^2 \tag{2.15}$$

Since the heat is spread over a wider area as the distance to the Sun increases, the heat flux that reaches the satellite changes throughout the year. Dividing the heat rate emitted by the Sun by the surface area of a sphere which radius, r_θ, is equal to the distance from the Sun to Earth in sequential positions, the maximum and minimum heat flux that reach the satellite can be estimated since we are in LEO. Bearing in mind that Aphelion refers to the point where the Earth is farthest from the Sun and Perihelion is the when the Earth is closest to the Sun, one can use Eq.(2.17) to obtain Figure 2.5.

$$\dot{q}_{solar_{Earth}} = \frac{\dot{Q}_{solar}}{4\pi r_\theta^2} \tag{2.16}$$

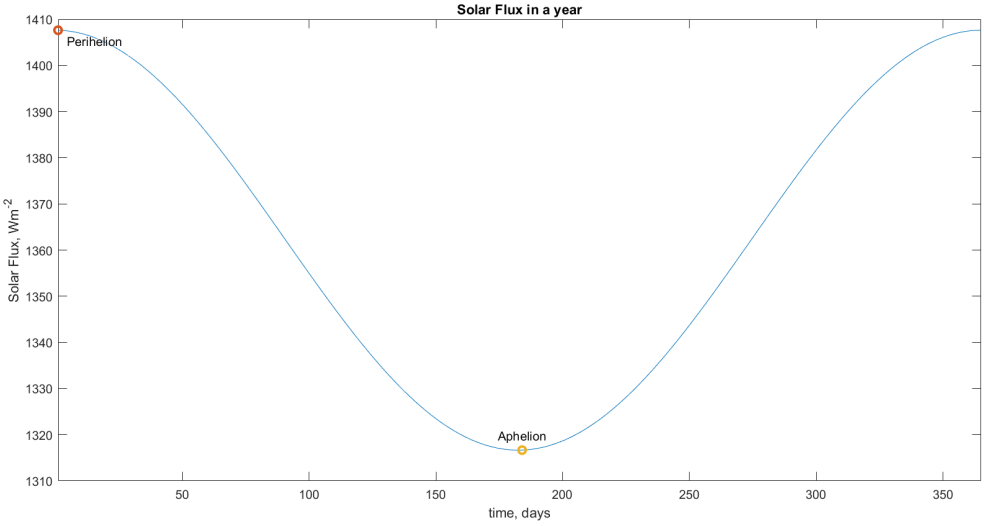

Figure 2.5: Solar Flux variation throughout a year.

The power absorbed, transmitted and reflected by each component of the satellite depends, respectively, on the materials' absorptivity, transmissivity and reflectivity and the component's area viewed by the Sun. The solar radiation absorbed by the spacecraft can be written as:

$$\dot{Q}_{\substack{\text{solar} \\ \text{absorbed}}} = \alpha_{solar} F_{Sun}^{component} A_{Sun} \dot{q}_{solar} \tag{2.17}$$

where α_{solar} is the component's absorptivity of solar radiation. The view factor, F_i^j, between two surfaces i and j is given by:

$$F_i^j = \frac{1}{A_i} \int_{A_i} \int_{A_j} \frac{\cos\theta_i \cos\theta_j}{\pi R^2} dA_i dA_j \tag{2.18}$$

As shown in Figure 2.6, θ_i and θ_j, are the angles between the line that connects both surfaces and the normal vector to surface i and j respectively [5].

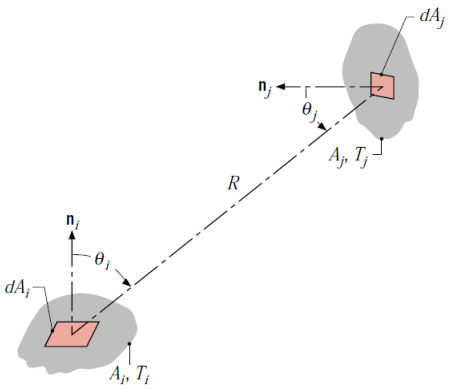

Figure 2.6: View factor associated with radiation exchange between two surfaces [5].

Due to the Sun's dimensions compared to the satellite's and assuming solar radiation isn't diffuse, Eq.(2.18) can be simplified:

$$F_{Sun}^{component} = \int_{A_{component}} \frac{\cos\theta_{component}}{\pi R^2} dA_{component} \tag{2.19}$$

Albedo

Albedo can be defined as the amount of solar radiation reflected by a celestial body back to space. According to [59], albedo is the integrated product of incident solar radiation spectral composition and the spectral reflectivity of the object. The problem with modeling albedo is due to different materials reflect different amounts of solar radiation. The atmosphere and weather themselves play an important role because different atmospheric layers have distinctive properties and the density of a cloud also has an impact on its reflectivity [60]. Thus, bond albedo, a value between 0 and 1 is usually used and typical values are listed in Table 2.6.

Table 2.6: Bond albedo for different materials. Adapted from [22].

Material	Water	Ice	Sand	Vegetation	Gravel	Concrete
Bond albedo	0.05	0.69	0.24	0.10	0.72	0.30

Including the fraction of solar radiation reflected by particles of the atmosphere, clouds and by the Earth's surface, the Earth's bond albedo is estimated to be $BA_{Earth} = 0.306$ [61]. Therefore, by applying Eq.(2.17) with the Earth's bond albedo, one can estimate the reflected heat flux:

$$\dot{Q}_{\substack{\text{solar reflected} \\ \text{by Earth}}} = BA_{Earth} F_{Sun}^{Earth} A_{Sun} \dot{q}_{solar} \tag{2.20}$$

Finally, the heat flux that reaches a satellite's component after the radiation from the Sun has been reflected by Earth is:

$$\dot{Q}_{albedo} = \alpha_{solar} F_{Earth_{sunlit}}^{component} A_{Sun} \dot{Q}_{\substack{\text{solar reflected} \\ \text{by Earth}}} \tag{2.21}$$

In this case, the view factor calculation can't be simplified, since the reflected solar radiation is diffuse. Thus, the reflected solar radiation incident on a component can have any direction.

Earth's Infrared Radiation

Due to Earth's temperature being much lower than the Sun's, the radiation emitted by the Earth is primarily located in the infrared zone of the electromagnetic spectrum [62]. By assuming Earth as a black body, the same set of equations presented to the solar radiation calculation may be applied. First, it is assumed that Earth is opaque: the heat flux that reaches it is either reflected back to space or absorbed. Then, the heat rate emitted by the Sun and absorbed by Earth is calculated, taking into account Earth's bond albedo and the solar radiative flux that reaches it [63].

$$\dot{Q}_{\substack{\text{solar absorbed} \\ \text{by Earth}}} = \alpha_{solar} F_{Sun}^{Earth} A_{Sun} \dot{q}_{solar} \tag{2.22}$$

where $\alpha_{solar} = 1 - BA_{Earth}$. Assuming Earth is in thermal equilibrium, the heat rate emitted by the Sun and absorbed by Earth must be equal to the infrared heat rate emitted by Earth [64]:

$$\dot{Q}_{infrared} = \dot{Q}_{\substack{\text{solar absorbed} \\ \text{by Earth}}} \tag{2.23}$$

Working on both sides of Eq.(2.23), the following expression is derived:

$$\dot{q}_{infrared} = \alpha_{solar} F_{Sun}^{Earth} \dot{q}_{solar} \tag{2.24}$$

And:

$$\dot{Q}_{\substack{\text{infrared} \\ \text{absorbed}}} = \alpha_{infrared} F_{Earth}^{component} A_{Earth} \dot{q}_{infrared} \tag{2.25}$$

where $\alpha_{infrared}$ represents the component's absorptivity of infrared radiation. Since Earth is provided with a significant atmosphere the sunlit and dark sides of the Earth are considered to emit the same infrared radiation [62].

Radiation to Space

Since the components cannot be approximated to a black body, in order to quantify their heat flux lost to the environment, one needs to modify the Stefan-Boltzmann Law and take into account the component's emissivity:

$$\dot{Q}_{emitted} = \sigma A_{component} \varepsilon_{component} T_{component}^4 \tag{2.26}$$

Radiation from the Surroundings

Each component being analyzed will be radiated from the surroundings' *i-th* component. This radiation can be considered exclusively from the infrared zone of the electromagnetic spectrum, due to low temperature of the components [64]. Thus, this radiation in the analyzed component is given by:

$$\dot{Q}_{\substack{\text{surroundings}\\\text{absorbed}}} = \alpha_{infrared} \sum_i F_i^{component} A_i \varepsilon_i \sigma T_i^4 \tag{2.27}$$

2.4.2 Conduction

Conduction may be defined as the transfer of energy from the more energetic to the less energetic particles of a substance due to interactions between the particles [5]. Besides the needing of matter, this mechanism can occur in either solids, liquids and gases, occurring along the direction of the negative temperature gradient *i.e.* from higher to lower temperatures.
According to [5] the heat flux resultant of heat conduction is a vector quantity and follows Fourier's Law:

$$\dot{\mathbf{q}}_{conduction} = -\Big(k_x \frac{\partial T}{\partial x}\mathbf{e}_x + k_y \frac{\partial T}{\partial y}\mathbf{e}_y + k_z \frac{\partial T}{\partial z}\mathbf{e}_z\Big) \tag{2.28}$$

Taking the scalar value and considering that two components of the satellite's can be made of different materials, the heat rate is:

$$\dot{Q}_{conduction} = -\sum_i \frac{T_{component} - Ti}{\frac{L_i}{k_i A} + R_{contact} + \frac{L_{component}}{k_{component} A}} \tag{2.29}$$

Eq.(2.29) assumes positive values if the heat is being transferred from the surroundings to the component analyzed. $R_{contact}$ refers to the contact resistance consequence of the imperfect contact between two surfaces, being determined empirically and k represents the thermal conductivity.

2.4.3 Convection

This mode of heat transfer can be defined as energy transfer between a surface and a moving fluid over the surface [5]. Due to the atmosphere rarefaction with altitude, this mode of heat transfer can be neglected when dealing with satellites.

2.4.4 Internal Heat Generation

Due to internal electric resistance, U, the satellite's electrical components dissipate energy, transforming electrical energy into thermal energy. Thus, this source of heat generation can be computed by [65]:

$$\dot{Q}_{internal} = U\, I \tag{2.30}$$

2.4.5 Heat Balance

For each component, the net heat rate is computed by solving the following differential equation:

$$\dot{Q}_{net} = \dot{Q}_{in} - \dot{Q}_{out} + \dot{Q}_{generation} \tag{2.31}$$

By taking into account the different heat exchange mechanisms and considering the component's mass, m, thermal capacity, c_p and temperature variation, Eq.(2.31) can be rewritten:

$$mc_p \frac{\partial T}{\partial t} = \dot{Q}_{\substack{\text{solar} \\ \text{absorbed}}} + \dot{Q}_{albedo} + \dot{Q}_{\substack{\text{infrared} \\ \text{absorbed}}} - \dot{Q}_{emitted} + \dot{Q}_{\substack{\text{surroundings} \\ \text{absorbed}}} + \dot{Q}_{conduction} + \dot{Q}_{internal} \tag{2.32}$$

2.4.6 Transient Thermal Analysis Simulation

According to [66], the general equation solved in transient thermal analysis has the form:

$$\mathbf{C_p}\dot{\mathbf{T}} + \mathbf{K_t}\mathbf{T} + \mathbf{R}\mathbf{T}^4 = \mathbf{HL}(t) + \mathbf{HL}(T) \tag{2.33}$$

where $\mathbf{C_p}$ is the heat capacity matrix, $\mathbf{K_t}$ is the heat conduction matrix, $\mathbf{R}$ is the radiation exchange matrix, $\mathbf{HL}(t)$ is a vector of applied heat loads that are constant or functions of time, but not functions of temperature and $\mathbf{HL}(T)$ is a vector of nonlinear heat loads that depend on temperature.
Eq.(2.33) is solved by Newmark's method with adaptive time stepping, and more information about it can be consulted in [66]. Although, as the solution progresses, the time steps are adjusted automatically, it is up to the user to specify a reasonable initial time step size. A conservative estimate can be determined as follows:

$$\Delta t_0 = \frac{\chi_{min}^2}{10\alpha_{max}} \tag{2.34}$$

where χ_{min} is the smallest element dimension in the model and α_{max} is the largest thermal diffusivity given by:

$$\alpha = \frac{k}{\rho c_p} \tag{2.35}$$

being ρ the density. The next time steps are calculated taking into account the relation between the maximum variations of temperature with time in the current time step and the previous one.

2.5 Dynamic Analysis

The majority of CubeSats are launched as secondary payloads [30]. Both the launch phase and the deployment one can be very aggressive in terms of vibration and loads applied on the structure. Therefore, a proper modal analysis and testing may establish the line between failure and success. As stated in [67], some examples are: expensive modification of design due to minimum frequency specification not satisfied, low frequency vibrations interference in on-board experiments due to coupling with the control system and orbital environment effects and failure due to fatigue caused by excessive vibration testing that caused resonance in the structure.

2.5.1 Numerical Modal Analysis

Modal analysis of a structure allows to evaluate its linear dynamic characteristics, *i.e.*, its goal is to determine the natural mode shapes and frequencies of a structure during free vibration. A natural mode of vibration is characterized by an harmonic motion of every point of the structure

around a point of equilibrium which is passed by ate the same instant for all the points [64]. The frequency of this harmonic motion is called the natural frequency.
The first of the natural frequencies of a structure is called fundamental frequency. The physical parameters that most influence the natural vibration modal data of a structure are the magnitude and distribution of masses and inertia, the elastic properties and the boundary conditions.
According to [68], the equations of motion of a multidegree-of-freedom system can be represented in matrix form as follows:

$$\mathbf{M}\ddot{\mathbf{x}} + \mathbf{C}\dot{\mathbf{x}} + \mathbf{K}_e\mathbf{x} = \mathbf{F} \tag{2.36}$$

where $\mathbf{M}$ is the mass matrix, $\mathbf{C}$ is the damping matrix, $\mathbf{K}_e$ is the stiffness matrix, $\mathbf{x}$, $\dot{\mathbf{x}}$ and $\ddot{\mathbf{x}}$ are the displacement, velocity and acceleration vectors, respectively and $\mathbf{F}$ is the force vector.
Since the goal of a modal analysis is to determine the natural modes of vibration, there's no force applied to the structure ($\mathbf{F} = \mathbf{0}$). Because natural frequencies correspond to the undamped case, $\mathbf{C}$ will not have influence in the calculation. Thus, Eq.(2.36) can be simplified to:

$$\mathbf{M}\ddot{\mathbf{x}} + \mathbf{K}_e\mathbf{x} = \mathbf{0} \tag{2.37}$$

Which corresponds to the undamped free vibration of the system. Assuming an harmonic solution:

$$\mathbf{x} = \phi_{\mathbf{v}} \sin(\varpi t + \varphi) \tag{2.38}$$

where $\phi_{\mathbf{v}}$ is the mode shape vector, ϖ is the angular frequency and φ is the phase angle. Substituting it in Eq.(2.37), the eigenequation is obtained:

$$(\mathbf{K}_e - \varpi^2\mathbf{M})\phi_{\mathbf{v}} = \mathbf{0} \tag{2.39}$$

The eigenvalues are the values ϖ^2 and the eigenvectors are $\phi_{\mathbf{v}}$. From the eigenvalues and eigenvectors, it is possible to obtain the natural frequencies and natural mode shapes, respectively. A non-trivial solution of the mode shapes is obtained for:

$$\det(\mathbf{K}_e - \varpi^2\mathbf{M})\phi_{\mathbf{v}} = \mathbf{0} \tag{2.40}$$

Expanding the equation above, one obtains the characteristic equation. Solving it for ϖ, the natural frequencies, in Hz, may be calculated from:

$$f_i = \frac{\varpi_i}{2\pi} \tag{2.41}$$

Substituting the natural frequencies, ϖ, in rad/s in Eq.(2.39) and choosing an arbitrary value for one of the components of the corresponding mode shape, all the other components of the mode shape are computed [68]. This can be done because the mode shape is intended to give information only about the shape of the vibration in each natural frequency, not the amplitude. It is usual to normalize the modes of shape in relation to the mass matrix by using the equation below:

$$\phi_{v_{i_n}}^T \mathbf{M} \phi_{v_{i_n}} = \mathbf{I} \tag{2.42}$$

The number of natural frequencies and corresponding mode shapes are equal to the number of degrees of freedom of the system. As stated in [68], when a linear elastic structure is in free or forced vibration, its vibration shape can be given by a linear combination of all its natural mode shapes.

If both $\mathbf{M}$ and $\mathbf{K_e}$ are symmetric and real, the mode shapes are orthogonal. This property means that each mode shape is unique and cannot be obtained by linear combination of the other modes and can be represented by:

$$\phi_{v_i}^T \mathbf{M} \phi_{v_j} = 0, \qquad i \neq j \tag{2.43a}$$

$$\phi_{v_j}^T \mathbf{K_e} \phi_{v_i} = 0, \qquad i \neq j \tag{2.43b}$$

By taking into account the ratio between stiffness and mass, it is possible to obtain Rayleigh's equation . This equation describes that the natural frequencies will be higher for a stiffer and lighter structure and is obtained from:

$$\varpi_i^2 = \frac{\phi_{v_i}^T \mathbf{K_e} \phi_{v_i}}{\phi_{v_i}^T \mathbf{M} \phi_{v_i}} \tag{2.44}$$

If the structure presents damping, each frequency of a damped vibration can be calculated by considering the following solution in each equation represented by Eq.(2.36) [64]:

$$x_i = C_i e^{s_i t} \tag{2.45}$$

where C_i is the amplitude of x_i and s_i is a complex number. Substituting the solution in each equation of the system, which represents each degree of freedom, the frequency of damped vibration, ϖ_d, can be obtained from:

$$\varpi_{d_i} = \varpi_i \sqrt{1 - \zeta_i^2} \tag{2.46}$$

Where ζ is the modal damping ratio and is given by:

$$\zeta_i = \frac{c_i}{2 m_i \varpi_i} \tag{2.47}$$

where c_i and m_i represent the damping and mass terms of the correspondent equation. An oscillatory motion only results if $\zeta < 1$, which corresponds to the underdamped case. In that situation, the frequency of the damped vibration is always lower than the natural frequency [64].

According to [69], NX NASTRAN has seven numerical methods to obtain the natural frequencies and corresponding mode shapes. The reason for seven different numerical techniques is because no one method is the best for all problems. While most of the methods can be applied to all problems, the choice is often based on the efficiency of the solution process.

The methods of eigenvalue extraction belong to one or both groups: transformation methods and tracking methods. In the former method, the eigenvalue equation is first transformed into a special form from which eigenvalues may easily be extracted while in the latter the eigenvalues are extracted one at a time using an iterative procedure.
The recommended real eigenvalue extraction method in NX NASTRAN is the Lanczos method, which combines the best characteristics of both the tracking and transformation methods. For most models the Lanczos method is the best method to use since it has a performance advantage over other methods. Therefore, the Lanczos method will be the one used in the modal analysis.

2.5.2 Experimental Modal Analysis

It is possible to obtain the natural frequencies and modes of vibration of a structure using experimental techniques. For that, the structure must be subjected to a certain input force and the output displacement, velocity or acceleration must be measured by the corresponding sensors in different points of the structure [70]. Two types of tests can be performed: impact testing or shaker testing.
The impact testing is the most popular method where an impact hammer to input the force in the structure is used. A cell load is attached to the hammer's head to measure the applied force and sensors measure the output in fixed directions and points of the structure. The input frequency range that is excited is controlled by the hardness of the hammer's head. The harder its tip, the wider the frequency range.
The shaker testing consists of attaching a shaker to the structure and input a force in the desired frequency range. The shakers are also provided with loads cells to control the input force and sensors are used to measure the output in the desired directions and points of the structure [71]. The shaker testing is usually chosen when the structure is large and heavier or when low frequencies are desired.
Both methods have disadvantages. For instance, in the impact testing, the hammer's impact in the structure may not be able to excite it uniformly and in the shaker method, the time duration must be long enough to be able to excite the structure at low frequencies. The obtained results from the modal tests are Frequency Response Functions (FRFs). These functions consist of the ratio of the output response of the structure due to the applied force, transformed from the time domain to the frequency domain using Fast Fourier Transform (FFT) algorithms. The frequency response is a complex number. The resonance frequencies of the structure are the peaks of its amplitude diagram [64]. When those peaks are hard to identify, the phase diagram may be used to help identify the resonance frequencies. The resonance frequencies are characterized by a shift in the phase angle. From displacement or acceleration outputs, the mode shape components are the peak values of the imaginary part, while for velocity outputs, they are the peak values of the real part [71]. Thus, from the FRF amplitude and phase diagrams and from the FRF real and imaginary parts, different information is obtained.
It must be noted that the resonance frequency is different from the natural frequency if the structure presents damping and, as seen before, the former will be lower than the latter.
Due to fact that the experimental testing was not performed by the author and was done for a 3U version of ORCA^{2}Sat (*Homathko*), further details about Experimental Modal Analysis theoretical background will not be provided in this work but may be consulted in the references listed throughout this subsection.

Chapter 3

Orbital Mechanics

Orbital mechanics is a core discipline within space mission design which focuses mainly on spacecraft trajectories under the influence of forces such as gravity, atmospheric drag and thrust. Section 3.1 is focused on how one can mathematically describe the spacecraft's orbit while Section 3.2 refers to the satellite-to-site visibility problem. Finally, Section 3.3 presents the outer space environment effects on the spacecraft's subsystems.

3.1 Orbital Elements

An orbit, or trajectory, can be defined as the path of an artificial or natural body through space [72]. In the 17^{th} century, during his work as director of the Prague Observatory, Johann Kepler formulated three laws using information from his predecessor about relative motion of Mars [4]:

1. Every planet moves in an orbit that is an ellipse, with the Sun at one focus of the ellipse;
2. The radius vector drawn from the Sun to any planet sweeps out equal areas in equal times;
3. The squares of the periods of revolution of the planets are proportional to the cubes of the semimajor axes of their orbits.

These laws were formalized later on when Newton's theory of gravitation produced a theoretical principle that explained the motions of the planets and laid the foundation for modern space flight. Thus, the motion of two celestial bodies with masses m_1 and m_2 orbiting their common center of mass is given by:

$$\ddot{\mathbf{r}} = -\frac{G(m_1 + m_2)}{||\mathbf{r}||^3}\mathbf{r} \tag{3.1}$$

where $\mathbf{r}$ is the position vector of m_2 relative to m_1, G is the universal gravitational constant and $\ddot{\mathbf{r}}$ is the acceleration vector. According to [10], both the position vector and its derivative must be measured in an inertial reference frame in order to validate Eq.(3.1).
The motion of a spacecraft under the influence of a celestial body can be approximated by Eq.(3.1), a Keplerian Orbit, when ignoring the non-spherical symmetry of the bodies, the perturbations due to other bodies, and non-gravitational forces. Referring to the motion of a spacecraft around the Earth, one can neglect the spacecraft's mass and consider the center of mass of the system coincides with the Earth's center of mass. Therefore, $\mathbf{r}$ is now the position of the spacecraft with respect to Earth's center of mass and we ca introduce a new term called standard gravitational parameter of the Earth and given by:

$$\mu = Gm_{Earth} \tag{3.2}$$

And Eq.(3.1) can be simplified to:

$$\ddot{\mathbf{r}} = -\frac{\mu}{||\mathbf{r}||^3}\mathbf{r} \tag{3.3}$$

The angular momentum of m_2 relative to m_1, $\mathbf{h}$, can be given by:

$$\mathbf{h} = \mathbf{r} \times \dot{\mathbf{r}} \tag{3.4}$$

where $\dot{\mathbf{r}}$ denotes the velocity vector. Taking the time derivative of Eq.(3.4) and by working on it, one concludes that it is zero *i.e.* the angular momentum is conserved [6]. This property is called the conservation of angular momentum and allows to conclude that the path of m_2 around m_1 lies in a single plane: the orbital plane, defined by:

$$r(\theta) = \frac{h^2}{\mu}\frac{1}{1 + e\cos\theta} \tag{3.5}$$

where e is the orbit's eccentricity and θ is the spacecraft's true anomaly. Since $\cos(-\theta) = \cos\theta$ the trajectory described by the orbit equation is symmetric about the apse line as shown in Figure 3.1. Thus, a new parameter called semi-latus rectum can be introduced and is given by Eq.(3.6).

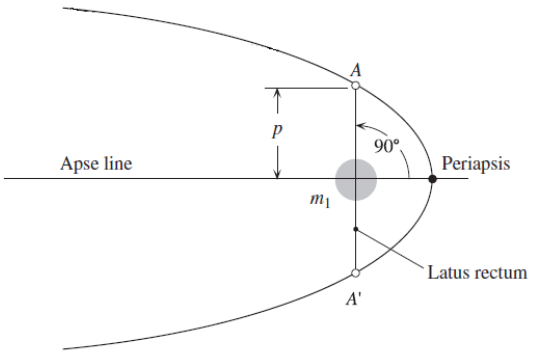

Figure 3.1: Illustration of the semi-latus rectum, p. Adapted from [6].

$$p = \frac{h^2}{\mu} \tag{3.6}$$

Therefore, Eq(3.5) can be rewritten:

$$r(\theta) = \frac{p}{1 + e\cos\theta} \tag{3.7}$$

To mathematically describe an orbit one must define six quantities: the orbital elements.

a The semi-major axis specifies the size of the orbit. This element is usually used for elliptical orbits instead of the angular momentum due to a more direct interpretation [6].

e The eccentricity specifies the shape of the orbit. Circular orbits have 0 eccentricity while elliptical ones assume a value between 0 and 1. An eccentricity of 1 corresponds to a parabolic orbit and values higher than that correlate to hyperbolic orbits.

i The inclination of the orbit is defined as the angle between the orbital plane and a reference plane (usually the Earth's Equatorial plane [4]) and assumes values in the range [0º,180º]. An inclination of 90º or less represents a *prograde* motion while values greater than that define a *retrogade* orbit. An orbit is termed *polar* if the inclination is either 90º or 270º and *equatorial* for the extreme values.

Ω The Right Ascension of the Ascending Node (RAAN)is measured counterclockwise in the equator plane, from the direction of the *Vernal Equinox* (denoted by γ in Figure 3.2 and introduced in Chapter 2) to the point at which the satellite makes it south-to-north crossing the Equator [4].

ω The argument of perigee is measured in the orbit plane along the direction of motion from the ascending node to the perigee.

θ The true anomaly is the angle between the spacecraft's position, **r**, and the direction of perigee in the direction of motion, defining the position of the satellite within the orbit.

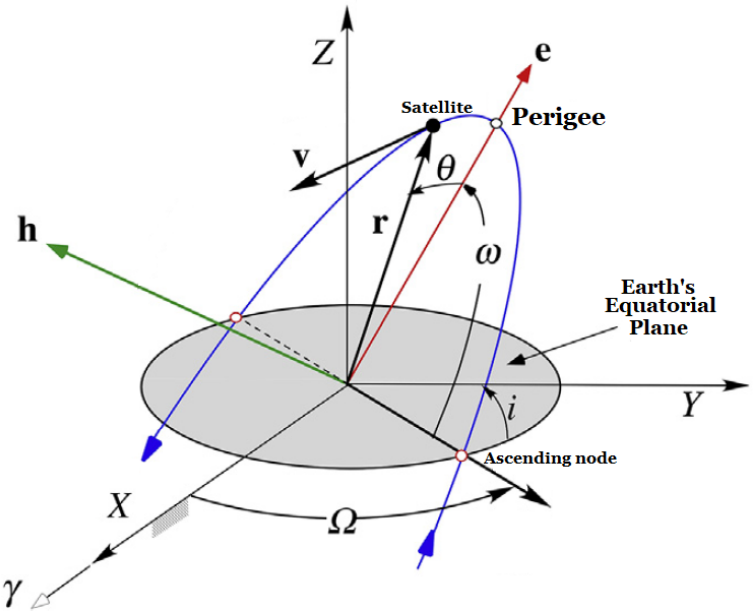

Figure 3.2: Orbital elements. Adapted from [6].

3.2 Access Time

The satellite-to-site visibility problem, which refers to the determination of opportunities for a satellite to observe or communicate with an object on the Earth's surface, plays an important role in coverage analysis of satellite orbits [73]. This study can be complicated by the fact that different parameters relate to different reference frames. The orbital elements are known with reference to the plane of the orbit while the location of the site is usually given in terms of the local geographic coordinates, which rotate with the Earth [7].
Rectangular coordinate systems are generally used in calculations of satellite's position and velocity in space, while the site's (usually a ground station) quantities of interest may be the azimuth and elevation angles and range.

The azimuth is the angle of the direction of the satellite, measured in the horizon plane from geographical north in clockwise direction. The range of azimuth is from 0° to 360° and is denoted by A_z in Figure 3.3. The elevation is the angle between a satellite and the observer's horizon plane. The range of elevation is 0° to 90° and is represented in Figure 3.3 by E_l.

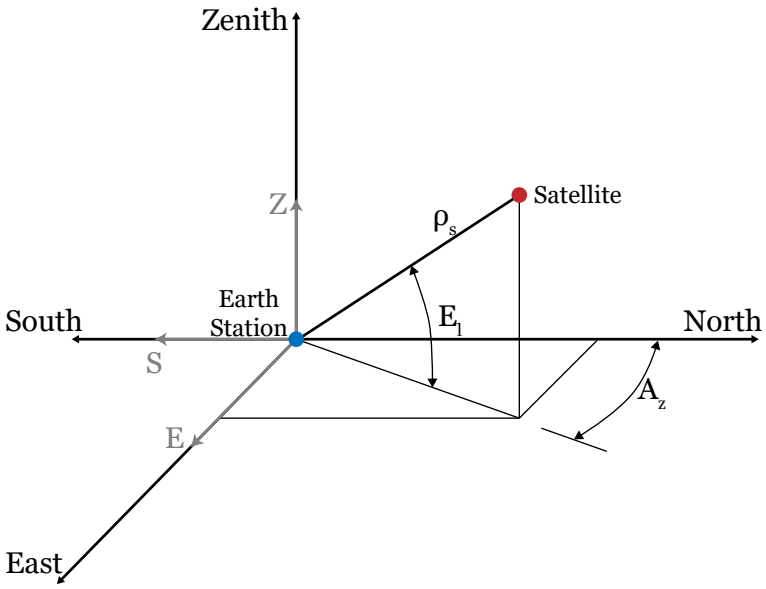

Figure 3.3: Azimuth and Elevation angles. Adapted from [7].

Every ground station has its visibility limits either for azimuth and elevation angles. According to the *Code of Federal Regulations*, title 47, sec. 25.205 [74] antennas must not transmit at elevation angles less than 5 measured from the horizontal plane to the direction of maximum radiation, in a frequency band shared with terrestrial radio services or in a frequency band with an allocation to space services operating in both the Earth-to-space and space-to-Earth directions. The east and west limits are set by both the coordinates of the earth station and the minimum antenna elevation, El_{min}, and can be approximated by Eq.(3.8) [7]:

$$E/W_{limits} = \lambda_S \pm \cos^{-1}\left(\frac{\sin\left(El_{min} - \sin^{-1}(\frac{R_E}{a}\cos El_{min})\right)}{\cos\phi_S}\right) \tag{3.8}$$

where ϕ_S and λ_S are the ground station's latitude and longitude, respectively.
In Figure 3.3, distance ρ_s represents the slant range between the satellite and the ground station, which changes over time, and can be computed by [8]:

$$\rho_s = R_E\left(\sqrt{\left(\frac{r}{R_E}\right)^2 - \cos^2 El} - \sin El\right) \tag{3.9}$$

where r is the distance between the satellite and the Earth's center. Figure 3.4 introduces a new angle, the nadir angle, defined as the angle under which the satellite sees the ground site. The nadir angle can be calculated with the following expression:

$$\alpha_0 = \sin^{-1}\left(\frac{R_E\,\sin\beta_0}{\rho_s}\right) \tag{3.10}$$

where β_0 is the Earth central angle, measured at the center of the Earth from the subsatellite[1] point to the target, and calculated with:

$$\sin \beta_0 = \frac{\rho_s \cos El}{r} \tag{3.11}$$

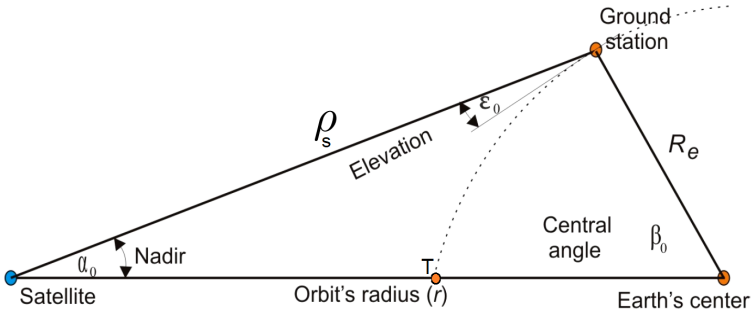

Figure 3.4: Satellite to ground station geometry. Adapted from [8].

3.3 Impact on Satellite's Subsystems

Spacecraft perturbations can be defined as any contribution to either perturbative accelerations (induced by perturbative forces) or perturbative torques. The former causes fluctuations in the orbital elements making the orbit to deviate from a Keplerian model while the latter cause an unintentional change in the spacecraft's angular rate.

3.3.1 Perturbative Forces

According to [21], perturbative forces can be split into four categories: non-gravitational forces, third-body interactions, nonspherical mass distribution and relativistic mechanics. The primary non-gravitational forces are atmospheric drag and solar radiation pressure. As stated in [10], for most applications relativist mechanics can be completely neglected and for spacecrafts in LEO third-body interactions are not significative. Thus, these effects are not mentioned in this thesis and Eq.(3.3) assumes a new form:

$$\ddot{\mathbf{r}} = -\frac{\mu}{||\mathbf{r}||^3}\mathbf{r} + \mathbf{a}_{drag} + \mathbf{a}_{solar} + \mathbf{a}_{gravity} \tag{3.12}$$

where each perturbative acceleration is related to it's perturbative force, applied on the spacecraft of constant mass m, through Newton's Second Law:

$$\mathbf{F}_{perturbative} = m\,\mathbf{a}_{perturbative} \tag{3.13}$$

Atmospheric Drag

Drag is a force due to atmospheric friction and it's direction is contrary to the body's velocity. This force is proportional to the atmospheric density, which decreases with altitude, making it

[1] Point where the joining line of the satellite and Earth's center intersect the Earth's surface. Denoted by T in Figure 3.4.

more severe at the orbit's perigee. This condition reduces the spacecraft's velocity at each perigee passage, reducing the apogee height and, consequently, both the semi-major axis and eccentricity. However, according to [10], both the perigee height and argument of perigee remain approximately the same. Due to this effect, atmospheric drag plays the most important rule in the orbit's lifetime and is given by:

$$\mathbf{F}_{drag} = -\frac{1}{2}\rho C_D A||\mathbf{v}_{rel}||\mathbf{v}_{rel} \tag{3.14}$$

where ρ is the local atmospheric density, C_D is a dimensionless drag coefficient, A is the spacecraft area projected along the direction of motion and $\mathbf{v}_{rel}$ is the relative velocity of the spacecraft with respect to the atmosphere.

The drag coefficient is a function of the shape of the spacecraft, it's orientation with respect to $\mathbf{v}_{rel}$, its surface properties and the composition of the atmosphere. Usually, this value is obtained through experimental and/or finite element analysis. Some reference values can be found in the literature, like Vallado's work represented in Figure 3.5.

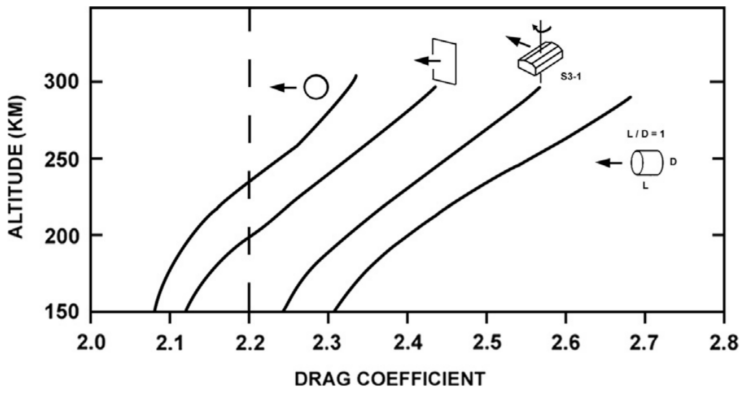

Figure 3.5: Drag coefficients for different body geometries and altitudes [9].

Since A depends on the spacecraft attitude (except for spherical spacecrafts), it's typical to model it's geometry as a collection of N flat plates of area A_i and outward normal unit vector $\mathbf{n}^i_{\mathcal{B}}$ expressed in the spacecraft body frame [10]. Therefore, the inclination of the i^{th} plate to the relative velocity is given by:

$$\cos\theta^i_{drag} = \left(\mathbf{A}^T\mathbf{n}^i_{\mathcal{B}}\right)^T\left(\frac{\mathbf{v}_{rel}}{||\mathbf{v}_{rel}||}\right) \tag{3.15}$$

where $\mathbf{A}$ is the attitude matrix that rotates the GCI frame to the spacecraft body frame. Finally, the drag force can be modeled:

$$\mathbf{F}_{drag} = -\frac{1}{2}\rho C_D A||\mathbf{v}_{rel}||\mathbf{v}_{rel}\sum_{i=1}^{N}{}'A_i\cos\theta^i_{drag} \tag{3.16}$$

where the prime on the sum indicates that only plates with $\cos\theta^i_{drag} > 0$ are included in the summation.

Lastly, the atmospheric drag-induced acceleration $\mathbf{a}_{drag}$ can be computed through Eq.(3.13).

Solar Radiation Pressure

Momentum exchange between the spacecraft and incident photons on its surface define the effect of the solar radiation pressure (SRP). Unlike atmospheric drag, SRP only affects the spacecraft when it's not in eclipse and also causes variations in all of the orbital elements [21]. For LEO this force is dominated by the atmospheric drag but for higher altitudes ($\geq 800\,km$) SRP will generally outweigh drag.
The pressure from radiation originating from the Sun, $\mathcal{P}_{Sun}$, is essentially constant in the vicinity of the Earth assuming an average value of $4.56\,\mu\mathrm{N\,m^{-2}}$ [75]. Thus, the force exerted on the spacecraft due to $\mathcal{P}_{Sun}$ is:

$$\mathbf{F}_{solar} = -\mathbf{A}_{\mathcal{B}}^{\mathcal{I}} \mathcal{P}_{Sun} A_S \, \hat{\mathbf{s}} \tag{3.17}$$

where $\mathbf{A}_{\mathcal{B}}^{\mathcal{I}}$ is the rotation matrix from frame $\mathcal{B}$ to $\mathcal{I}$, $\hat{\mathbf{s}}$ is a unit vector pointing from the sun to the spacecraft (the Sun line-of-sight vector) and A_S is the Sun-facing area of the spacecraft. Both variables are represented in Figure 2.4.
Ultimately, the perturbative acceleration induced by the solar radiation pressure, $\mathbf{a}_{solar}$ can be computed through Eq.(3.13).

Nonspherical Mass Distribution

The Earth is not a perfect sphere but rather has a slight pear shape with a bulge at the Equator, flattening at the poles and several minor mass anomalies like mountains and continents [76].
The Earth's oblateness causes an effect termed the regression of the nodes, which is the motion of the line of nodes opposite the direction of the spacecraft's motion. The other main oblateness perturbation is the motion of the line of apsides. This is equivalent to a cumulative, secular variation of the elements ω and Ω, while a, e and i undergo short period variations that average to zero over an orbit [77]. According to the same source, due to the conservative nature of the gravitational field, the vector form of Eq.(3.3) may be rewritten as the gradient of a scalar potential:

$$\ddot{\mathbf{r}} = -\nabla U \tag{3.18}$$

where ∇U is the gradient of the potential function U. Due to the approximate spherical symmetry of the Earth, it is convenient to develop the expression for U in spherical coordinates. Being $\mathbf{r}_{\mathcal{E}} = [r \;\; \phi \;\; \lambda]^T$ the position of the spacecraft in rotating frame $\mathcal{E}$, U is then expressed as:

$$U = -\frac{\mu}{r} + B(r, \phi, \lambda) \tag{3.19}$$

where $B(r, \phi, \lambda)$ is the spherical harmonic expansion that corrects the previous term for the Earth's asymmetric mass distribution given by [76]:

$$B(r, \phi, \lambda) = -\frac{\mu}{r}\left[\sum_{n=2}^{\infty} J_n \left(\frac{R_E}{\mu}\right)^n P_n(\sin\phi) + \sum_{n=2}^{\infty}\sum_{m=1}^{n} J_{nm}\left(\frac{R_E}{\mu}\right)^n P_{nm}(\sin\phi)\cos(m\Delta\lambda)\right] \tag{3.20}$$

Here, r, ϕ and λ are the spacecraft's radius, latitude and longitude, respectively and $\Delta\lambda = \lambda - \lambda_{nm}$. The quantities J_n, J_{nm} and λ_{nm} are numerical coefficients. The functions $P_n(x)$ and $P_{nm}(x)$ are,

respectively, Legendre's polynomial of degree n and the associated Legendre function of degree n and order m given by [10]:

$$P_n(x) = \frac{1}{2^n\, n!}\frac{d^n}{dx^n}(x^2-1)^n \tag{3.21a}$$

$$P_{nm}(x) = (-1)^{-m}(x^2-1)^{m/2}\frac{d^m}{dx^m}P_n(x) \tag{3.21b}$$

The terms related to Legendre's polynomials constitute the zonal harmonics, which describe deviations in the north-south direction of the gravitational potential from the Newtonian one of $-\mu/r$ and are represented in Figure 3.6a. The terms having J_{nm}, $n \neq m$, as factors are the tesseral harmonics and those having J_{nm}, $n = m$, are the sectorial harmonics. Both the tesseral and sectorial harmonics represent deviations in an east-west direction as illustrated in Figure 3.6b and Figure 3.6c, respectively.

(a) Zonal harmonics (b) Tesseral harmonics (c) Sectorial harmonics

Figure 3.6: Types of spherical harmonics. Adapted from [10].

According to [10], the strongest perturbation due to the shape of the Earth, closely related to its oblateness, arises from the J_2 zonal coefficient, with J_3 being more than 400 times smaller.

Finally, taking the gradient of U in spherical coordinates in Eq.(3.18) yields the inertial perturbative acceleration due to the non-spherical Earth as:

$$\mathbf{a}_{gravity} = \mathbf{A}_{\mathcal{E}}^{\mathcal{I}}\left[-\frac{\partial B}{\partial r} \qquad -\frac{1}{r}\frac{\partial B}{\partial \phi} \qquad -\frac{1}{r\sin\phi}\frac{\partial B}{\partial \lambda}\right]^T \tag{3.22}$$

where $\mathbf{A}_{\mathcal{E}}^{\mathcal{I}}$ is the rotation matrix from frame $\mathcal{E}$ to $\mathcal{I}$.

3.3.2 Perturbative Torques

Perturbative torques may be classified as being either internal or external. Internal perturbative torques are typically caused by the pointing rotation of solar arrays, antennas or cameras; the deployment of antennas, solar arrays, instruments or booms; propellant slosh; flexible appendages; and reaction wheel imbalances [2]. Generally, internal torques are much smaller than external ones, needing only to be accounted for in high-precision pointing systems. As such, they are not detailed in this work. According to [78], the principal external torques acting on a spacecraft are the aerodynamic torque, the SRP torque, the gravity gradient torque and the magnetic torque.

Aerodynamic Torque

Aerodynamic torque is a consequence of the atmospheric drag force already described in Section 3.3.1. Thus, in order to compute this torque, the same assumptions that were used to model the atmospheric drag force are used. By modeling the spacecraft as a collection of N plates, the drag force acting on the i^{th} plate is given by a variation of Eq.(3.16):

$$\mathbf{F}^i_{drag} = -\frac{1}{2}\rho C_D A ||\mathbf{v}_{rel}|| \mathbf{v}_{rel} A_i max(\cos\theta^i_{drag}, 0) \tag{3.23}$$

Therefore, the aerodynamic torque on the spacecraft is:

$$\mathbf{L}_{aero} = \sum_{i=1}^{N} \mathbf{r}^i_{cp} \times \mathbf{F}^i_{drag} \tag{3.24}$$

where $\mathbf{r}^i_{cp}$ is the vector from the spacecraft's center of mass to the center of pressure of the i^{th} plate. Note this algorithm does not account for potential self-shielding that would exist on concave spacecrafts. In principle, aerodynamic torques could be used for attitude control, either for passive control like the feathers on an arrow, or even for active control by providing movable surfaces [10].

Solar Radiation Pressure Torque

To model the torque caused by SRP, the same assumptions as those made in Section 3.3.1 for the SRP force are taken. Also considering the same assumptions used previously for the aerodynamic torque, we can compute the SRP force acting on the i^{it} plate:

$$\mathbf{F}^i_{solar} = -\mathbf{A}^{\mathcal{I}}_{\mathcal{B}} \mathcal{P}_{Sun} A^i_S \, \hat{\mathbf{s}}_i \tag{3.25}$$

where $\mathbf{A}^{\mathcal{I}}_{\mathcal{B}}$ is the rotation matrix from frame $\mathcal{B}$ to $\mathcal{I}$, $\hat{\mathbf{s}}_i$ is a unit vector pointing from the sun to the i^{th} plate and A^i_S is the Sun-facing area of said plate. Both variables are represented in Figure 2.4. Finally, the torque caused by the SRP can be modeled has:

$$\mathbf{L}_{solar} = \sum_{i=1}^{N} \mathbf{r}^i_{cp} \times \mathbf{F}^i_{solar} \tag{3.26}$$

where $\mathbf{r}^i_{cp}$ is the vector from the spacecraft's center of mass to the center of pressure of the i^{th} plate.

This formulation has several limitations. First, it ignores other radiation sources like Earth's infrared radiation and Albedo. Secondly, the torque due to thermal radiation emitted from the spacecraft has been ignored. Thermal radiation torque can usually be neglected because the thermal flux is emitted roughly equally in all directions, so that the net torque is small [10]. Finally, potential self-shadowing of concave spacecraft is also ignored. If the configuration of the spacecraft is known *a priori*, self-shadowing can be taken into account by replacing A^i_S with the area of the flat plate that is visible to the Sun after accounting for shadowing.

Gravity Gradient Torque

The non-uniformity of the gravitational field over a rigid body in space leads to a torque about its center of mass. In order to model this torque, the following assumptions are taken [78]: only the influence of the Earth needs to be considered; the Earth possesses a spherically symmetrical mass distribution; the spacecraft is small compared to its distance from the the Earth's center of mass; and the spacecraft consists of a single body.
Contrary to what was done in Section 3.3.1 to model the nonspherical mass distribution force, the Earth is assumed to have a spherically symmetrical mass distribution for gravity gradient torque considerations. This assumption is valid considering the magnitude of the gravity gradient torque compared to the magnitude of the other external torques [77].
Thus, the expression for the gravity gradient torque is given by:

$$\mathbf{L}_{gravity} = 3\left(\frac{\mu}{r^3}\right)(\hat{\mathbf{o}}_{\mathbf{3}})_{\mathcal{B}} \times \mathbf{J}_{\mathcal{B}} \tag{3.27}$$

where $\mathbf{J}_{\mathcal{B}}$ is the inertia matrix of the spacecraft in components of frame $\mathcal{B}$ and $(\hat{\mathbf{o}}_{\mathbf{3}})_{\mathcal{B}}$ is the representation of $\hat{\mathbf{o}}_{\mathbf{3}}$ in frame $\mathcal{B}$.

Magnetic Torque

As stated in Subsection 2.3.1, the magnetic torque can be computed with Eq.(2.10).
Similarly to the gravitational potential described in Section 3.3.1 the magnetic flux density generated by the Earth may be computed through the gradient of a scalar potential [78]:

$$\mathbf{B} = -\nabla V \tag{3.28}$$

The scalar potential V may be written as [76]:

$$V(r,\phi,\lambda) = R_E\left[\sum_{n=1}^{\infty}\sum_{m=0}^{n}(g_{nm}\cos(m\lambda) + h_{nm}\sin(m\lambda))\left(\frac{R_E}{r}\right)^{n+1}P_{nm}(\cos\phi)\right] \tag{3.29}$$

where r, ϕ and λ are the spacecraft's radius, latitude and longitude, respectively; g_{nm} and h_{nm} are termed Gauss coefficients and describe internal sources (*e.g.* current loops); and $P_{nm}(x)$ is the associated Legendre function given by Eq.(3.21a).
Taking the gradient of V in spherical coordinates in Eq.(3.28) yields the magnetic flux density generated by the Earth represented as:

$$\mathbf{B} = \left(\mathbf{A}_{\mathcal{E}}^{\mathcal{I}}\mathbf{A}_{\mathcal{B}}^{\mathcal{E}}\right)^{-1}\left[-\frac{\partial V}{\partial r} \quad -\frac{1}{r}\frac{\partial V}{\partial \phi} \quad -\frac{1}{r\sin\phi}\frac{\partial V}{\partial \lambda}\right]^T \tag{3.30}$$

where $\mathbf{A}_{\mathcal{B}}^{\mathcal{E}}$ is the rotation matrix from frame $\mathcal{B}$ to $\mathcal{E}$.

Chapter 4

ORCA^{2}Sat

This chapter is intended to introduce to the reader the overall of ORCA^{2}Sat, including its mission, external structure and internal accommodation of its components, subsystems and payloads. Notably, UVic is known for, rather than purchasing existing hardware and adopting third party software, develop in-house the mechanical structure, the On-Board Computer (OBC), the power system, the payload, Printed Circuit Board (PCB) design, communications system, small hardware (*e.g.* magnetorquers and earth-sensors) and even the ground station.

4.1 Mission

ORCA^{2}Sat is a 2U CubeSat carrying two different payloads design to calibrate ground observatories. The first payload, develop in-house by the UVic team, is termed the Airborne Laser for Telescopic Atmospheric Interference Reduction (ALTAIR) and is responsible for the optical calibration of the following stations: the European Southern Observatory (ESO), the Large Synoptic Survey Telescope (LSST), the Panoramic Survey Telescope and Rapid Response System (Pan-STARRS) and UVic. The second payload, developed by SFU, is responsible for the radio calibration of the CHIME observatory. Table 4.1 summarizes the ground observatories that each payload is responsible to calibrate.

Table 4.1: Payloads and respective ground observatories.

Payload	**Ground Station**	**Latitude** [°]	**Longitude** [°]	**Country**
ALTAIR	ESO	−24.5772	−70.404167	Chile
	LSST	−30.244638	−70.74942	Chile
	Pan-STARRS	20.7072	−156.2558	USA (Hawaii)
	UVic	48.4634	−123.3117	Canada
SFU Payload	CHIME	50.5914369	−118.2373525	Canada

4.1.1 ALTAIR Payload

The ALTAIR payload has the goal of being a precision light source above the atmosphere. This could be achieve thanks to an integrating sphere [37].The function of an integrating sphere is to spatially integrate radiant flux, where light incident on a diffuse surface creates a virtual light source by reflection [79]. According to the same reference, due to multiple reflections inside the cavity, the total flux incident on the sphere surface is higher than the input flux.
The integrating sphere of the ALTAIR payload as a diameter of 5 cm, eliminating directionality of the light source (sphere measurements not dependent on viewing angle) while maintaining output intensity and wavelength. As illustrated in Figure 4.1a, the sphere is composed by nine LEDs[1] to offer light over the visible spectrum and near infrared and one laser to provide monochromatic light at 635 nm. The sphere's inside will be coated with *Spectralon* in order to increase its reflectivity and

[1]Each of the three following combinations of wavelength and power output will have three LEDs: 560 nm and 30 mW, 630 nm and 50 mW and 470 nm and 30 mW.

two photodiodes will measure the intensity and wavelength of the LEDs, which are integrated into a special PCB. The first prototype of the integrating sphere 1U module is shown in Figure 4.1b.

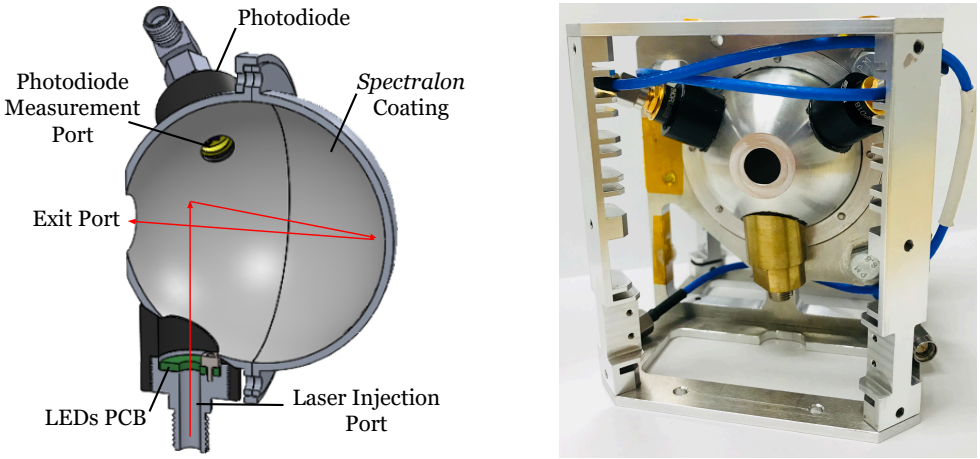

(a) Integrating sphere model

(b) First prototype

Figure 4.1: ALTAIR payload with photodiodes from [11].

Based on the tasks referred in Section 1.2, the operation of ORCA^{2}Sat can be summarized:

1. Launch from the ISS into orbit at an altitude of 405 km and a speed of around 27 600 km h^{-1};
2. Once the satellite is over the target region, the payload will sequentially flash a red laser and LEDs in the visible spectrum, while onboard sensors measure the real output of each pulse;
3. Concurrently, the observatories record their own measurements of the satellite's emitted light;
4. Information about the intensity and wavelength of each pulse is transmitted to ground observatory being calibrated;
5. By comparing these two measurements, investigators can determine localized attenuation due to atmospheric and instrumental interference;
6. With this knowledge, researchers can reduce the uncertainties associated with measuring the total luminous output of stellar objects.

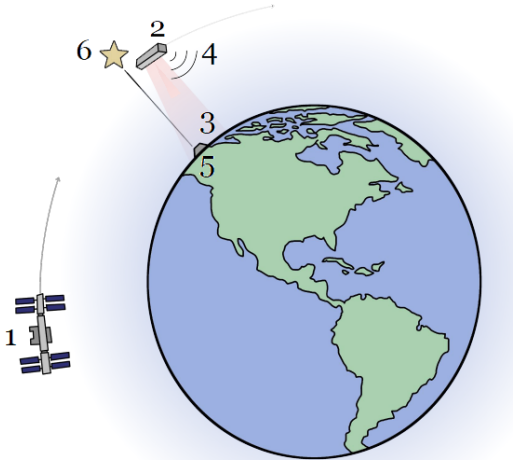

Figure 4.2: Sequential operation of the ALTAIR payload.

4.1.2 SFU Payload

The SFU payload can be described as an orbiting transponder broadcasting a predefined bit string on multiple frequencies within the operating range of the CHIME telescope (400-800 MHz) [80]. CHIME requires a characterization of the telescope's complex gains, which is currently performed with natural astronomical sources sweeping the sky east to west for the longitudinal axis. It is however difficult to use a similar source to characterize the complex gain along the latitudinal axis. A orbiting artificial source with knowledge of signal characteristic moving with a longitudinal component relative to the telescope can provide the additional information needed to fully characterize CHIME's performance.
The payload will consist of a radio transmitter with one or more carriers in the 400 MHz to 800 MHz frequency bandwidth. The carriers will be modulated with a predefined binary sequence with a bounded small cross-correlation within a set that will be used by CHIME to isolate the payload signal from other sources [80]. The transmitter will operate continuously while within line of sight of the telescope and fall silent when not. Finally, the ground segment will take this data and compute the time dependent power density received at the telescope, which will then be handed of to CHIME researchers for use in calibrating their telescope.

4.2 Requirements

Regarding CubeSats, there are several constraint that need to be fulfilled. Those requirements could be for CubeSats in general [31], from the launcher [18], the payload carried and, if applied, the program under which the CubeSat is being made (in this case is the Canadian CubeSat Project [34]). The complete requirement list can be consulted on the previous references. The relevant constraints regarding this thesis' scope are presented below:

- The spacecraft configuration and dimensions shall be of a 2U ($10 \times 10 \times 22.7$ cm);
- Aluminum 7075, 6061 or with hardness equal to or greater than hard anodized aluminum hall be used for both the main spacecraft structure and the corner rails;
- The spacecraft shall have 4 rails, one per corner, along the Z axis, with edges rounded to a radius of at least 0.5 ± 0.1 mm, minimum width of 6.0 mm and ends with a minimum surface area of 4.0×4.0 mm^2 contact area;
- The spacecraft mass shall not exceed 5.657 kg;
- The CubeSat center of gravity shall be within 2cm of its geometric center;
- CubeSats shall be designed to withstand overall temperature range of -40 °C to +65 °C;
- CubeSats shall comply with NASA guidelines for hazardous materials;
- CubeSats shall have a minimum of three mechanical deployment switches corresponding to inhibits in the main electrical system;
- A *Remove Before Flight* pin is required and shall preclude any power from any source operating any satellite functions with the exception of pre-integration battery charging;
- The CubeSat operations shall not begin until a minimum of 30 minutes after deployment from the ISS.

Related to the scientific mission designed for ORCA^{2}Sat there is also the requirement that the output port from the integrating sphere must be pointing in the Nadir direction while passing over the groundstations from Table 4.1 at local night time, and must not be obstructed by any other component. Also, the SFU payload may have pointing requirements itself that could affect the entire design, but since it's still not defined from the SFU team, those constraints aren't listed here. Adding to these requisites, there are also dynamic requirements that must be satisfied, but can only be verified after the first design of the ORCA^{2}Sat has been decided. It is crucial that the decisions made in terms of arrangement and accommodation in the satellite take into account that the manufacturing, assembly and wiring harness are possible, facilitated and logical. Furthermore, one must keep in mind that the decisions made will then affect static, dynamic and thermal behavior.

4.3 Structure Subsystems

Regarding the structure function, its main goal is to accommodate the needed subsystems and payloads to correctly operate the satellite and perform the proposed scientific missions. It also unites all the components and provides rigidity to the satellite. As seen in the previous section, there's some flexibility in terms of the structure configuration and how it's machined.

Aluminum 7075 T6 was chosen for the main parts of the outer structure: external rails, end caps and side panels, as shown in Figure 4.3a. Besides combining good mechanical and thermal properties with low density, this type of aluminum has a higher strength-to-weight ratio over a 6061 alloy. The material should be black anodized in order to facilitate the thermal control of the structure, assuring passive thermal control [81]. However, the decision to use a black paint in the aluminum or not will be taken after the first thermal simulations, to determine if it is indeed necessary.

Regarding both internal structural components and the integrating sphere, Aluminum 6061 T6 was selected as the material. Since said components don't withstand higher loads than the external components, one can still have good mechanical properties from this cheaper alloy based on the components' function. Thus, for the internal rails from both the payload module and the electronic stack Aluminum 6061 T6 was used while for the integrating sphere a polished version was selected in order to increase its reflective capacity. Some properties of said alloys without black coating can be found in Table 4.2.

Table 4.2: Thermal and mechanical properties of selected alloys [5], [23], [24].

	Al7075 T6	**Al6061 T6**	**Al6061 T6 (polished)**
Density, ρ [$\mathrm{kg\,m^{-3}}$]	2810	2700	2700
Young's Modulus, E [GPa]	71.7	68.9	68.9
Thermal Conductivity, k, [$\mathrm{W\,m^{-1}\,K^{-1}}$]	130	167	167
Specific Heat Capacity, c_p [$\mathrm{J\,kg^{-1}\,K^{-1}}$]	960	896	896
Emissivity, ε	0.1	0.1	0.05

As for the way the primary structure is built, it was decided to assemble the structure from multiple aluminum panels, since they are easily machined, their price is lower and produce less waste material. Another main concern when choosing this method was to ensure modularity of the structure. By having separate rails from the side panels, one can assemble the outer structure and slide in the 1U modules as represented in red in Figure 4.3b. That way each module could be removed without disassembling the entire structure.

(a) Outer structure parts (b) Internal modules (c) Final structure

Figure 4.3: Components of ORCA^{2}Sat's outer structure.

This structural design philosophy allows to incorporate different payloads into 1U modules rather than redesigning the entire structure for every new payload. It also allows for easy access of internal components and and each could design their own systems independently of the structure team. A final representation of ORCA^{2}Sat's structure can be found in Figure 4.3c.

4.4 Electronic Subsystems

In order to guarantee that the satellite is capable of completing its mission several electronic systems must be developed. An electronic stack was designed in order to fit ORCA^{2}Sat's bottom unit. This stack consists of a series of PCBs connected in parallel to a perpendicular backplane, forming a computer system. Each PCB has a specific function according to the integrated circuits and components mounted in it. The distance between each board is keep by the electronic stack rails, where the PCB is slid in and epoxied, dictated by the minimum distance between the backplane slots set by the manufacturer.

Each PCB is made of a layered laminate of FR-4 and copper along a total thickness of 1.6 mm. FR-4 is a composite material of fiberglass and epoxy resin, where FR stands for Flame Retardant and the type 4 indicates woven glass reinforced epoxy resin. After reaching to the manufacturer [25] the properties of said orthotropic material are presented in Table 4.3. Regarding the copper layers there are 4, each with a thickness of 35 µm.

Table 4.3: Thermal and mechanical properties of FR-4 [25].

	Length Direction	Cross Direction
Density, ρ [kg m^{-3}]	1900	
Specific Heat Capacity, c_p [J kg^{-1} K^{-1}]	840	
Young's Modulus, E [GPa]	25.5	22.9
Poisson's Ratio, ν	0.137	0.133
Coefficient of Thermal Expansion, CTE [K^{-1}]	55×10^{-6}	16×10^{-6}

Since the design is in its initial phase, it was decided to save space for a total of 6 PCBs. In the next paragraphs, the most important components are described and the number denoted within brackets is the correspondent number in Figure 4.7.

Backplane (15) Physically connects all the PCBs to an easier mounting and dismounting of the electronics stack, allowing for the formation of a computer bus.

Payload PCB (2) Responsible of dictating the behavior of the ALTAIR payload. It drives both the laser and the LEDs through a programmed constant current and converts from analog to digital the output of the measured light by the photodiodes.

Spare PCB (3) Has no specific function but can be used to integrate circuits or sensors from other systems that won't fit in their designated board.

OBC PCB (4) Supports the OBC in order for it to retain all the processing capabilities making possible to operate the satellite. It was decided to choose the MIT Free Real Time Operating System kernel, FreeRTOS [82], mainly due to its low computational intensity, intrinsic software timer and Cyclic Redundancy Check (CRC) error checking method. The microcontroller selected by the software team is the TMS570LS Safety MCU [83] because it has already been used in previous CubeSats developed at UVic, has voltage and clock internal management, built-in temperature sensor, external debugger and provides an easy integration.

Communications PCB (5) Allows the connection between the satellite and the ground component for information exchange. Therefore, makes t possible to control the satellite mode of operation from Earth. It's also responsible to integrate the electronics necessary to characterize the CHIME ground segment.

Power PCB (6) Provides the physical support to connect the solar boards, deployment switches and the *Remove Before Flight* switch. It also supports the batteries that store the power generated by the solar panels and regulates and distributes it by the rest of the subsystems that require electric energy. To store the energy generated, a total of 4 Lithium Ion NCR18650B 3350mAh batteries provided by Panasonic was chosen by the power team lead. Each battery **(11)** has the properties presented in Table 4.4 and are all integrated in the battery holder **(10)**.

Table 4.4: Properties of each battery cell [26], [27].

Mass, m [g]	48.5
Height [mm]	65.3
Diameter [mm]	18.5
Nominal Voltage, V [V]	3.6
Thermal Conductivity, k, [$\mathrm{W\,m^{-1}\,K^{-1}}$]	21.7
Specific Heat Capacity, c_p [$\mathrm{J\,kg^{-1}\,K^{-1}}$]	675
Charging Temperature Range [°C]	0 to +45
Storage Temperature Range [°C]	-20 to +60

ADCS PCB (8) Provide physical support for the Z **(14)** and Y **(7)** axis magnertorquers[2] and respective connections. Since a 2U is very limited in terms of space, the magnetorquers are the only actuators of the ADCS system. This PCB can also be used to support some the referred system sensors.

[2]The X axis magnetorquer **(9)** is located behind the integrating sphere in the ALTAIR payload module.

All three magnetorquers are actuators part of the ADCS system which is responsible to or determining the satellite orientation and position and for maintaining it with the desirable orientation, even if external disturbances are applied. In order to perform such task, besides said actuators, some sensors are also required. An example of such sensors are a GPS receiver, magnetometers, gyroscopes, sun sensors and horizon sensors. Although the specific parts for each system were not decided to the date, some of the considered possibilities by the ADCS team leader are listed in Table 4.5 and represented in Figure 4.4. It is important to know their operating temperature range so that the thermal control system to be developed can maintain each component within its safe temperature range.

Table 4.5: ADCS components with respective dimensions, mass and operating temperature range.

Component	Model	Quantity	Dimensions [mm]	Mass [g]	Temperature [°C]
GPS	Venus838FLP [12]	1	$10 \times 10 \times 1.3$	0.3	-40 to +85
Magnetometer	LIS3MDL [13]	1	$2 \times 2 \times 1$	0.008	-40 to +85
Gyroscope	FXAS21002C [14]	1	$4 \times 4 \times 1$	0.038	-40 to +85
Sun Sensor	NANO-60 [15]	6	$18 \times 18 \times 3.85$	10	-40 to +85
Horizon Sensor	TPA 32.16C [16]	4	$47 \times 26 \times 9.9$	-	-20 to +80

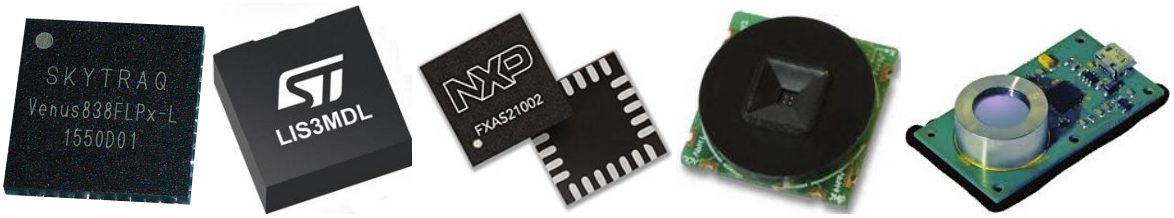

(a) GPS receiver (b) Magnetometer (c) Gyroscope (d) Sun sensor (e) Horizon sensor

Figure 4.4: ADCS sensors [12–16].

To operate the satellite, it is mandatory to generate electric power that can be used. Therefore, a total of 12 solar cells were distributed in 3 PCBs each fixed on the satellite's lateral faces, except the face pointing in nadir direction. The chosen solar cells are the 30% Triple Junction GaAs Solar Cell Assembly 3G30A provided by AZUR SPACE Solar Power GMBH [17] **(1)**. The dimensions, in millimeters, and some mechanical and thermal properties can be found in Figure 4.5 and , respectively. For the state of the project while writing this thesis, the radiator panel placed on the nadir face, as shown in Figure 2.1b, has no specific function. However, since it is also a PCB, can be used to embed sensors for other subsystems or even attach a patch antenna.

Table 4.6: Mechanical, thermal and optical properties of each solar cell [17].

Base Material	GaInP/GaAs/Ge on Ge substrate
Anti-Reflective Coating	TiO_x/Al_2O_3
Surface Area, A [cm^2]	30.18
Mass, m [g]	3.56
Thickness, h [µm]	280 ± 25
Thermal Conductivity, k, [$W\,m^{-1}\,K^{-1}$]	57
Specific Heat Capacity, c_p [$J\,kg^{-1}\,K^{-1}$]	325
Coefficient of Thermal Expansion, CTE [K^{-1}]	6.03×10^{-6}
Emissivity, ε	0.88
Absorptivity, α	0.9

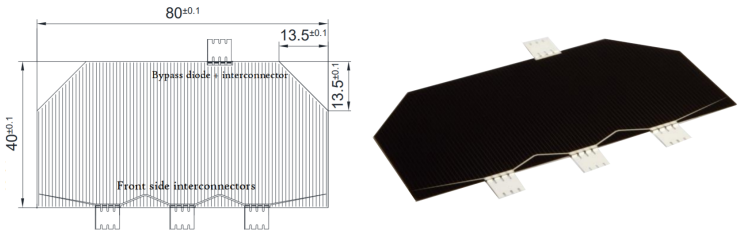

Figure 4.5: 30% Triple Junction Solar Cell 3G30A. Adapted from [17].

As stated in Section 4.2, some switches are required. A *Remove Before Flight* pin **(12)** is used to cut all the power from the satellite while allowing to recharge the batteries. This technique is adopted to protect the operators who integrate the spacecraft into the rocket's payload bay and removed at the end of the process. The deployment switches **(13)** are responsible for turning on the satellite after deployment from the ISS. In order to change the state of the switches and activate the electronics, deployment pins are required and their mechanism is illustrated in Figure 4.6.

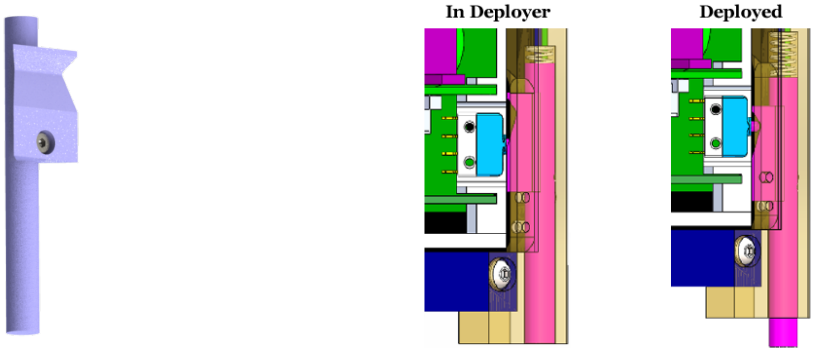

(a) Deployment pin shape

(b) Deployment switches' states

Figure 4.6: Deployment switches' mechanism.

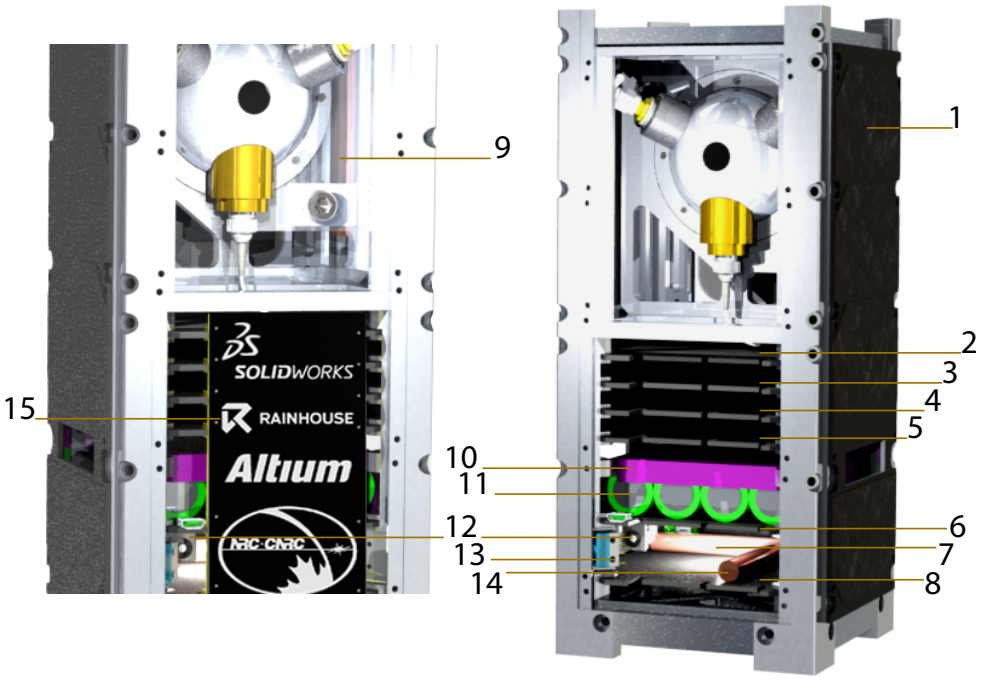

Figure 4.7: ORCA^{2}Sat configuration without the radiator panel.

Chapter 5

Orbital Model

This chapter takes into account the effect of an orbit generated by an ISS deployment. In order to have a complete mission design such study should be performed. Thus, Section 5.1 presents a study related to the ORCA^{2}Sat's access time to each ground station, Section 5.2 compares two flight attitudes in order to optimize the power generation and a preliminary power budget is also performed, Section 5.3 shows the Earth's magnetic field variation which is going to be used to control the satellite with the magnetorquers and in Section 5.4 the orbital decay is presented, setting the mission lifespan. The thermal impact, however, is not presented in this chapter due to its extensiveness. Instead, it is detailed in Chapter 6.
As referred in [34], cubesats developed under the *Canadian Cubesat Project* are granted a launch from the ISS as soon as the satellite gets *space ready*. This launch condition restricts the satellite's to an orbit similar to the ISS'. Since cubesats have several restrains, is of major interest to maximize power generation. Sun-synchronous orbits keep the satellite in the Sun throughout its life time, maximizing power generation. Sun-synchronous orbits are nearly polar orbits [6], meaning its inclination should be around 90°, while the ISS orbit inclination is about 51.6412° [84]. In order to change a satellite's inclination to a polar orbit, Eq.(5.1) should be computed with an ISS velocity of $7.6725\,\mathrm{km\,s^{-1}}$ [84].

$$\Delta v_i = 2\,\sin\left(\frac{\Delta i}{2}\right) \tag{5.1}$$

An increment of at least $5\,\mathrm{km\,s^{-1}}$ perpendicular to its trajectory when the satellite is at perigee is needed to perform such maneuver. Therefore, a change of inclination is completely unsustainable and ORCA^{2}Sat will be deployed from the ISS in a way that its apogee coincides with the ISS' perigee. The orbital elements of such orbit can be found in Table 5.1 bearing in mind that the initial true anomaly, θ_0, was set to 0°.

Table 5.1: ORCA^{2}Sat's orbital elements.

a [km]	e	i [°]	Ω [°]	ω [°]
6768.24	0.00005	51.6409	117.7634	34.8042

With the elements from Table 5.1, a orbital period of 92.66 minutes was computed through Eq.(2.3).

5.1 Access Time

As per Table 5.1 the latitude coverage for ORCA^{2}Sat is between ±51.6409°. Furthermore, bearing in mind that a satellite spends much of its time near the extreme latitudes and analyzing the ground stations' coordinates from Table 4.1, we could expect much lower access times for the ESO, LSST and Pan-STARRS observatories. A representation of the ground track for one orbit can be seen in Figure 5.1.
The access time for ORCA^{2}Sat was done with the *Systems Tool Kit 11* (STK) software from Analytical Graphics, Inc. The simulation was done for a year from September 1^{st} 2020 until

September 1^{st} 2021. As stated in Section 3.2, according to [74], the minimum elevation angle for each observatory to be able to track the satellite was set to 5°. However, due to a different payload type and more complex viewing requirements, the minimum elevation angle for CHIME was set at 20°. Also, according to the payload team, it was defined a viewing cone with an half-angle of 30° for the ALTAIR payload. The final scenario is represented in Figure 5.2.

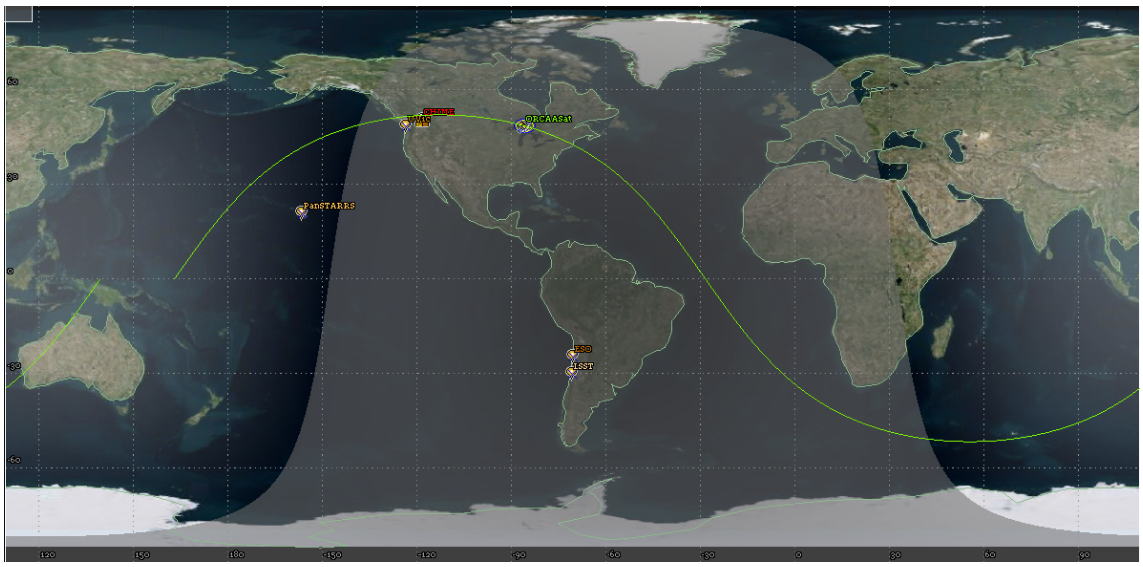

Figure 5.1: ORCA^{2}Sat ground tracking for one orbit.

The results for both the total number of accesses, a_n, and cumulative access duration for each month, Δa in minutes, can be found in Table 5.2 for each individual ground observatory. The total access time and number of accesses is represented in Figure 5.3 and Table 5.3 shows the average number of access per month and duration of an ORCA^{2}Sat's access to each ground station. The results correspond to an orbital epoch set to September 1^{st} 2020 at 00:00:00 h.

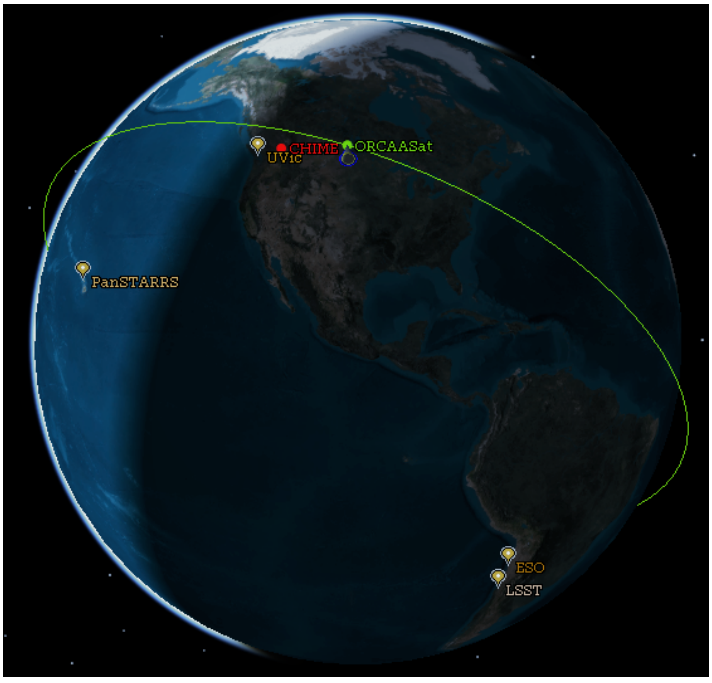

Figure 5.2: STK 3D scenario.

Table 5.2: Number of accesses and respective total duration per month for each ground station.

	ALTAIR								SFU Payload	
	ESO		LSST		Pan-STARRS		UVic		CHIME	
Month	a_n	Δa	a_n	Δa	a_n	Δa	a_n	Δa	a_n	Δa
Sep	17	15.33	18	16.12	15	12.72	50	45.73	60	30.53
Oct	16	13.99	17	15.25	15	13.53	50	45.37	57	28.51
Nov	16	13.76	17	15.29	16	13.75	50	43.36	59	28.23
Dec	17	15.64	19	17.50	15	14.30	50	44.79	59	30.56
Jan	17	15.08	18	15.79	16	13.55	52	47.29	58	28.15
Feb	15	13.34	18	15.67	13	12.72	42	38.44	54	27.78
Mar	16	14.26	17	15.09	17	14.33	52	46.80	58	28.58
Apr	17	14.45	17	14.92	13	12.79	46	43.07	58	29.39
May	17	14.99	18	16.94	17	14.44	51	45.23	60	30.09
Jun	16	14.49	18	16.64	14	13.16	45	41.41	54	26.52
Jul	16	14.17	17	15.16	17	14.51	53	48.57	62	32.28
Aug	17	15.35	17	15.20	14	13.13	48	43.01	55	26.94
Total	197	174.85	211	189.56	182	162.96	589	533.06	694	347.56

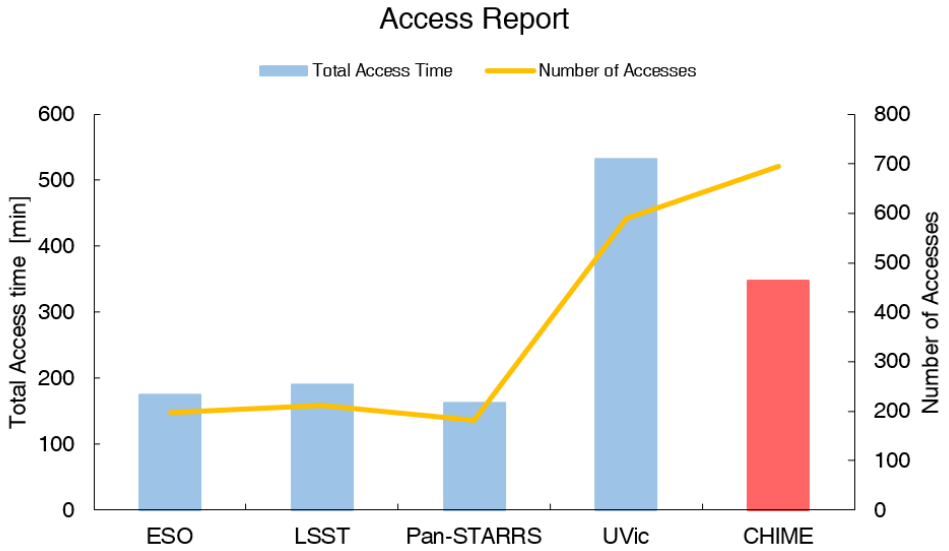

Figure 5.3: Total number of accesses and respective total duration for each ground station in a year.

Table 5.3: Average accesses and each duration for the different ground stations.

	ESO	LSST	Pan-STARRS	UVic	CHIME
$\overline{a_n}$ [month^{-1}]	16	18	15	49	58
$\overline{\Delta a}$ [s]	53.26	53.90	53.72	54.30	30.05

As expected, due to the orbital elements, UVic and CHIME have higher access from ORCA^{2}Sat than the other ground stations. All the observatories outside Canada have less than 20 access per month, meaning the satellite won't be able to calibrate them every day and further planning must be defined in order to guarantee the mission's success. The average duration of each access is almost one minute for every ground station with a minimum elevation angle of 5°. Also, even though CHIME as the biggest amount of access, the total access duration is not the maximum of the all the observatories. This is due to the bigger elevation angle defined for said ground station. Other factors can also affect this access duration, like the link budget and the minimum signal to noise ratio from the SFU payload. However, such values aren't yet defined at the time of this thesis but, as soon as defined, another access time study should be performed.

5.2 Power Generation

As already mentioned, CubeSats have several constraints regarding power generation. One way of maximizing the power generation is using orientable solar panels which provide constant power during the orbit daylight [85]. However, having moving mechanisms also decrease the reliability of the system, and the ORCA^{2}Sat decided to avoid such alternative. Thus, since fixed panels cannot be continuously oriented towards the Sun, two flight attitudes were studied in order to maximize the power generation.

The first attitude is set as a nadir pointing satellite with the X^+ face along the velocity vector. The second attitude is defined as a nadir pointing satellite with the Y^- face aligned with the spacecraft's trajectory. Both attitudes were considered static in. This means that the satellite is not rotating along any other axis except the one that allows a constant nadir pointing (denoted as *Body Y* in Figure 5.4). The first attitude is represented in Figure 5.4a and the second in Figure 5.4b.

Since *STK* only provides 2U CubeSat models with deployed solar arrays, the simple model in Figure 5.4 had to be exported through another software. A simple ORCA^{2}Sat model was built in *SketchUp* where the blue surfaces had to be identified as solar cells with 30% efficiency by altering the model code. However, some factors could not be taken into account. One example is the reflectivity of the solar cells which can decrease significantly the amount of power generated at certain angles [42].

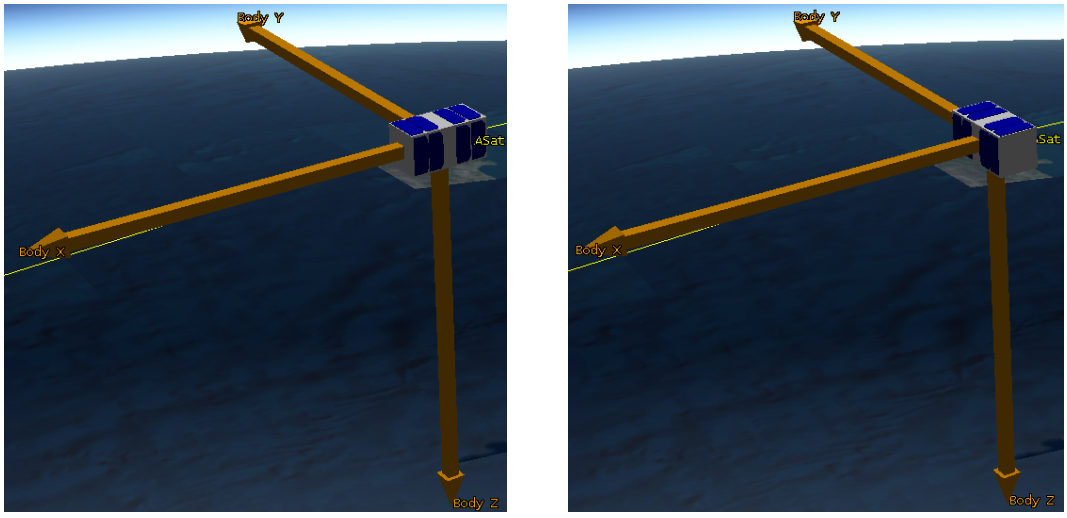

(a) Flight Attitude 1. (b) Flight Attitude 2.

Figure 5.4: Two different flight attitudes respecting nadir pointing.

Before performing a power generation analysis, the β angle was computed for a year through Eq.(2.4). The value of β is directly linked to the amount of time a spacecraft spends in sunlight, giving us a prediction of the power generation distribution. The results are presented in Figure 5.5. The β angle has a variation of roughly $\pm 75°$ and peak power regions are expected to fall within these extreme angles. The first extreme is reached around mid December, which matches with the December Solstice. The second extreme is reached about the ending of May and beginning of June, matching the June Solstice. The last peak happens in mid July. Also, is expected that the least amount of power generation coincides with close to zero values of the β angle.

The results about the power generation for the first attitude is represented in Figure 5.6 and for the second one in Figure 5.7. Table 5.4 shows both the average and peak power generation.

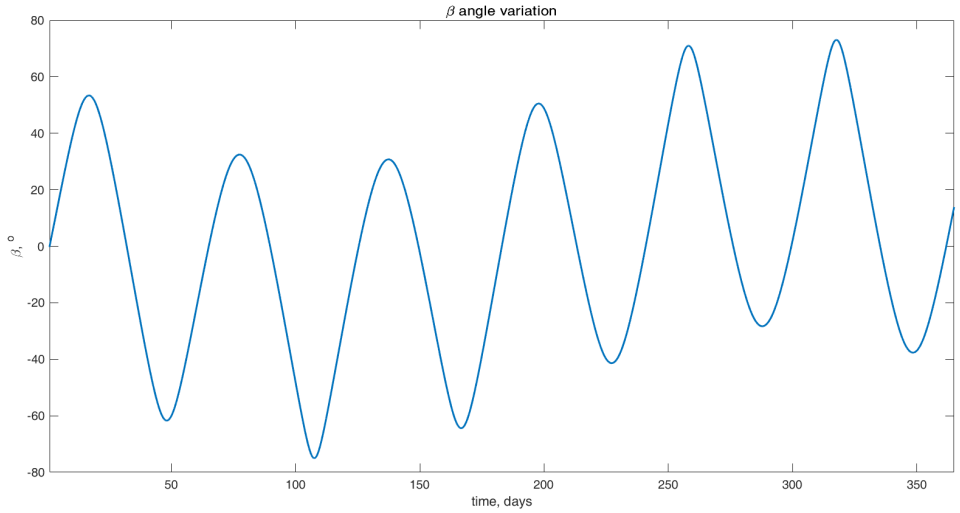

Figure 5.5: β angle variation in a year (September 2020 to September 2021).

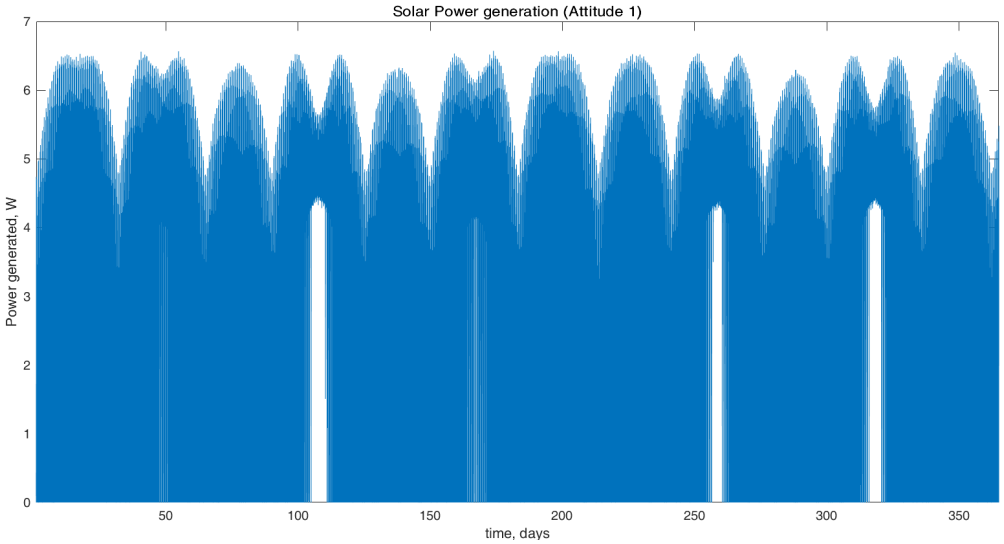

Figure 5.6: Power generation for flight Attitude 1.

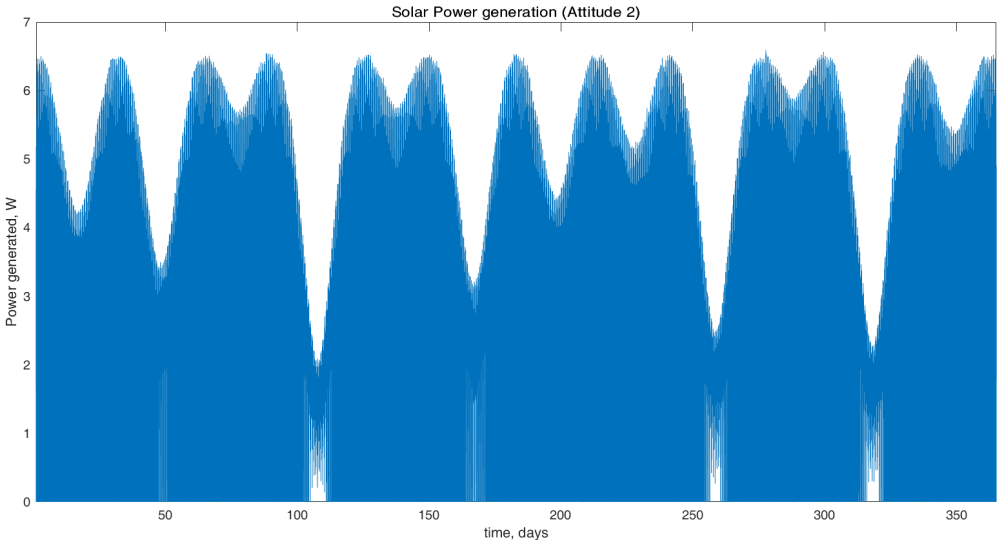

Figure 5.7: Power generation for flight Attitude 2.

Table 5.4: Average and peak power generation for two flight attitudes.

	Average Power [W]	Peak Power[W]
Attitude 1	2.5786	5.914
Attitude 2	2.6917	5.929

As shown in Table 5.4, both the average and peak power are higher for the second flight attitude. However, the increase in those values is almost indistinguishable: around 4% for the average power and less than 0.3% for the peak power. It can also be checked, in Figure 5.7, that are several moments where the power generation is below average, which is not an ideal situation.

Furthermore, having a larger face along the flight direction has an impact on other subsystems and mission aspects. One problem is the increase in drag forces on the satellite shortening its lifetime in orbit. However, the magnitude of such reduction will only be quantified in Section 5.4. After discussions with the ADCS team, it was also concluded that the second flight attitude is not adequate for a system using only magnetorquers. The larger face along flight direction requires larger torques to control both roll and yaw motions, compromising pointing and power requirements. Therefore, in order to find a balance between the several ORCA^{2}Sat's subsystems, the first flight attitude seems a more logical choice. However, before making the final decision, it is necessary to evaluate how the different power generation patterns will influence systems' activity.

In order to ensure mission success, one critical aspect of mission design is the power budget. The power budget helps setting limits for components consumption and designing the power system itself. However, such analysis should be made over a long period of time because only analyzing over a short period can give false robustness of the power system.

Since all the systems aren't yet defined, some values had to be assumed for the different power consumptions. Such values can be found in Table 5.5.

Table 5.5: ORCA^{2}Sat's systems power consumption.

System	Power Consumption [W]
Bus	1.4
ALTAIR	1.0
Communications	3.3

The value defined for the bus consumption includes the OBC consumption, EPS and typical attitude determination sensors consumption. ALTAIR consumption contains the laser, LED's and photodiodes power needs. The communications system consumption was set to a value agreed upon with the SFU team.

The bus is a constant consumption throughout the mission in order to keep the satellite functioning. Both ALTAIR and the communications system will only be fired when flying over the assigned ground stations from Table 4.1. The ADCS system was defined to have an 80% duty cycle. All the values are rough approximations and can be reduced in the future of the design process.

The power budgets in Figure 5.8 and Figure 5.9 were done for the course of one year for the power system designed by the power team leader with the specs found in Table 5.6.

Table 5.6: Power system specifications.

Net Power [W]	90% of the power generated
Total battery capacity [Wh]	40
Battery charging efficiency [%]	90
Battery discharging efficiency [%]	90

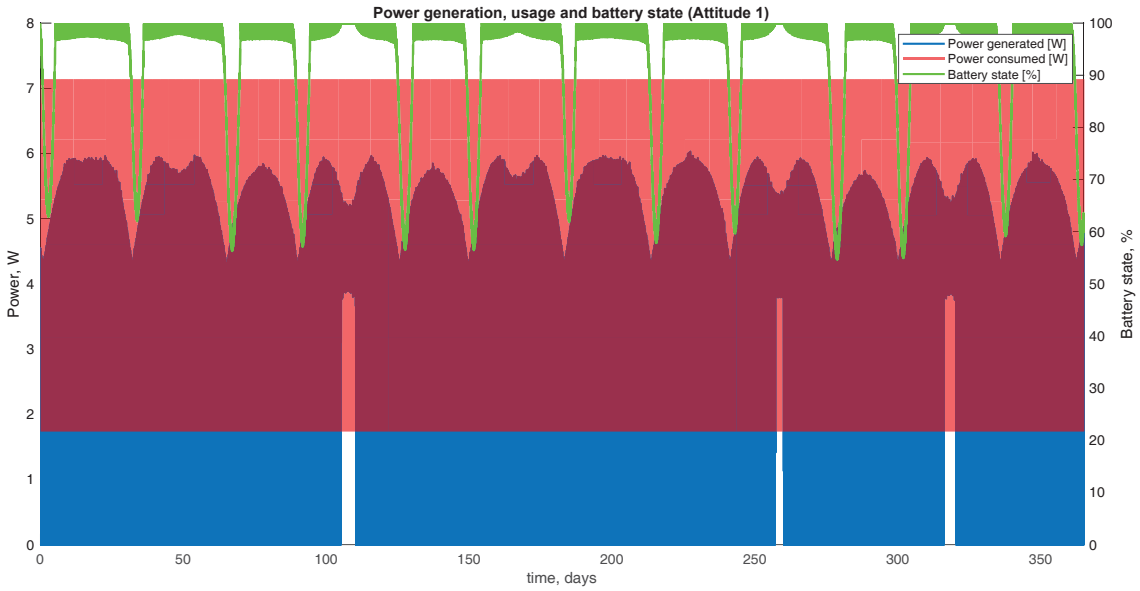

Figure 5.8: Power budget over a year for Attitude 1.

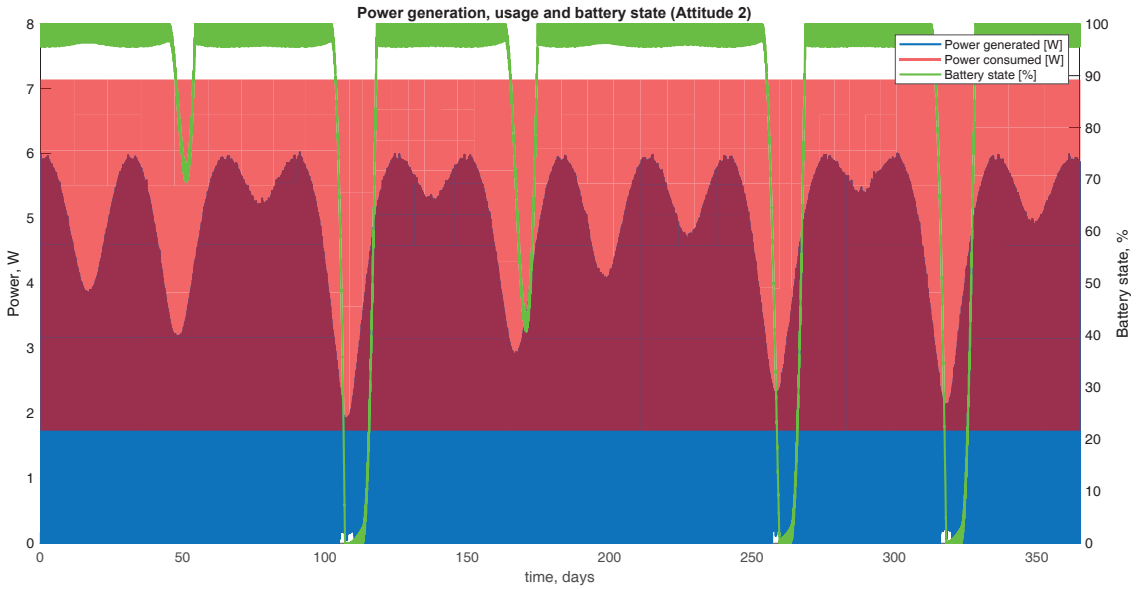

Figure 5.9: Power budget over a year for Attitude 2.

The power system is designed in a way that any power required to power the systems is drawn from the batteries and the power generated by the solar cells is used to recharge the batteries. As can be seen in Figure 5.9, the DOD of the batteries is 100%, meaning that the batteries fully discharge for Attitude 2. For Attitude 1, the DOD is around 45%. Although this value is not ideal, the batteries don't completely discharge, case which would set an end to the mission. It can also be seen that the batteries take about 10 days to fully recharge after reaching a minimum.

Since the data presented in Figure 5.8 and in Figure 5.9 is plotted along a large period of time, making it hard to interpret it, was decided to make a more clear graph. Thus, the daily average power generation was computed for both attitudes and plotted against the yearly average power generation. The results are represented in Figure 5.10. Even though Attitude 2 generates more power than Attitude 1 for around 62% of the time, the first flight attitude assumes a more desirable

power generation pattern, based on the results for the power budget.

Based on the results, it was decided to select flight Attitude 1 for ORCA^{2}Sat. The deciding factor was the batteries being completely drain for Attitude 2. According to the team, the ADCS system is the one accounting for the major power drain from the batteries. Thus, this system should be one of the main concerns for the next steps of the project. Also, according to the responsible team members, the OBC consumption can also be reduced, which will reduce the DOD of our batteries. Other measures that can be used to improve our power budget can be only firing the payloads if the batteries are above a certain limit or applying a passive attitude stabilization (*e.g.* spinning stabilization [10]) to decrease both the ADCS consumption and duty cycle.

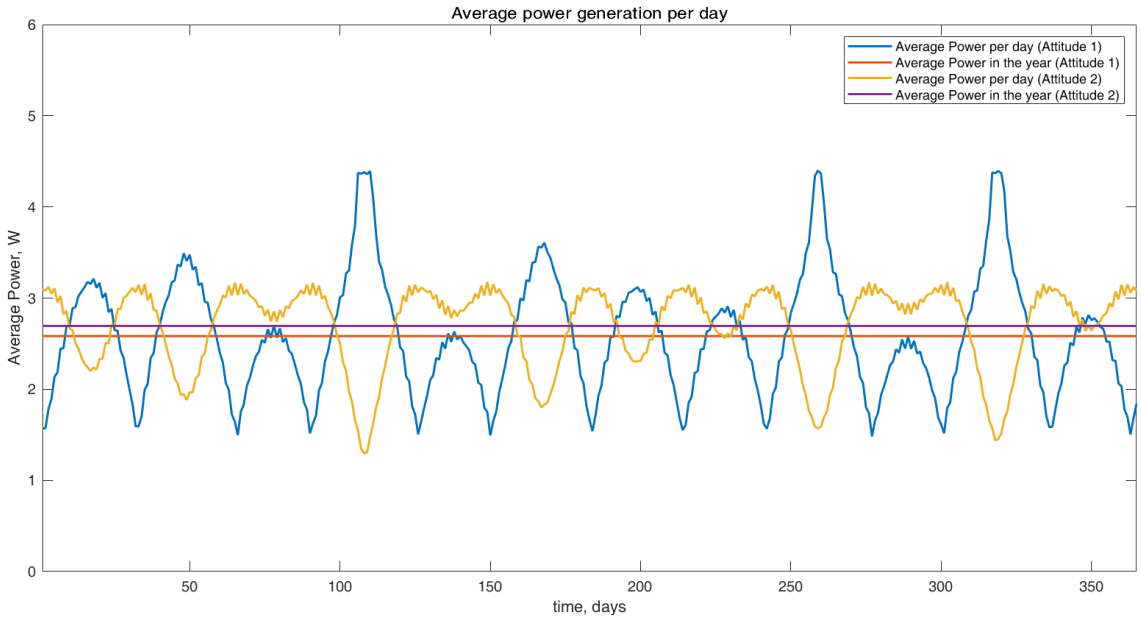

Figure 5.10: Daily power generation comparison.

5.3 Magnetic Field

As stated before, the Earth's magnetic varies in time, height and coordinates. However, for satellites in LEO, the magnetic field of Earth has enough intensity to control the satellite through magnetorquers. In order to study the Earth's magnetic field variation, a study was conducted for an entire year of mission. Eq.(3.28) was computed trough an intrinsic *MATLAB* function termed *wrldmagm* based on *The World Magnetic Model* (WMM) [86].

As expected, this model has several limitations. The WMM specification produces data that is only reliable five years after the epoch of the model, which begins January 1, of the model year selected. Since the latest epoch available is 2015, only values between September 1^{st} 2020 and December 31^{st} 2020 were considered as reliable results. The WMM describes only the long-wavelength spatial magnetic fluctuations due to the Earth's core, neglecting intermediate and short-wavelength fluctuations, contributed from the crustal field. Also, the substantial fluctuations of the geomagnetic field, which occur constantly during magnetic storms and almost constantly in the disturbance field (auroral zones), are not included.

By providing the location of the spacecraft in geodetic coordinates, the *wrldmagm* function computes the unnormalized associated Legendre polynomials and derivatives via recursion relations and returns the magnetic field intensity. The results for an entire day are represented in Figure 5.11.

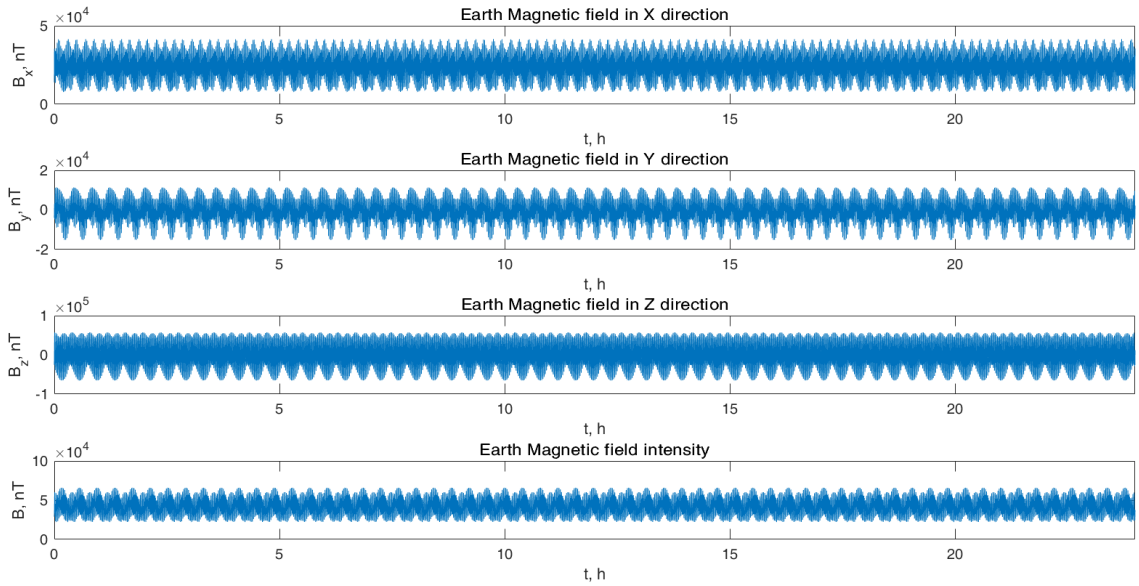

Figure 5.11: Earth's magnetic field intensity variation.

In order to know the magnitude of the torque produced by ORCA^{2}Sat's magnetorquers with the available magnetic field one can use Eq.(2.10). Since the scope of this thesis does not includes a detailed modeling of the ADCS system some simplifications are done in order to compute the commanded magnetic dipole moment, $\mathbf{m}$. This way, the team can have a general idea of the satellite control efficiency. By estimating values of the generated torques and comparing to values of disturbing torques values, one can see the feasibility of the ADCS system.
Table 5.7 summarizes the variables used, in cooperation with the ADCS team, in order to calculate the magnetorquers' magnetic dipole moment. The value of the power used for the magnetorquers is lower than the one used in the power budget analysis. Such conservative value was chosen to illustrate a worst case scenario and order to show how much the ADCS system can be improved in the future steps of ORCA^{2}Sat's project. A final value of $0.206\,\mathrm{A\,m^2}$ for the magnetorquers' dipole moment, m, was computed for each magnetorquer.

Table 5.7: Magnetorquers specifications with wire from [28].

Selected Wire	American Wire Gauge 32
Bus Voltage [V]	3.3
Available Power [W]	0.6
Electrical Current [A]	0.1818
Core Radius [mm]	4
Core Length [mm]	70
Number of wire turns	360

With the magnetorquers represented in Figure 4.7, the vector $\mathbf{m}$ can be simplified for the magnetorquers denoted by **(9)**, **(7)** and **(14)**:

$$\mathbf{m_{(9)}} = [m \quad 0 \quad 0] \tag{5.2a}$$

$$\mathbf{m_{(7)}} = [0 \quad m \quad 0] \tag{5.2b}$$

$$\mathbf{m_{(14)}} = [0 \quad 0 \quad m] \tag{5.2c}$$

The environmental torques in Table 5.8 were provided by the ADCS team and, as expected, the

Aerodynamic Torque is at least one degree of magnitude higher than the remaining. At the time of this thesis, the magnetic torque is not yet computed. However, a value of $4.5 \times 10^{-7}\,\mathrm{N\,m}$ for the average residual magnetic moment was found in [87].

Table 5.8: Perturbative torques range of values for a 2U CubeSat in ISS orbit.

Torque Nature	Torque Range [Nm]
Aerodynamic	$[2.174 \times 10^{-6}\ ;\ 6.519 \times 10^{-6}]$
Solar Radiation Pressure	$[4.5 \times 10^{-8}\ ;\ 1.349 \times 10^{-7}]$
Gravity Gradient	$[5.0 \times 10^{-8}\ ;\ 5.0 \times 10^{-7}]$

Defining pitch, roll and yaw rotations about the Y, X and Z axis, respectively, the following torques were computed. The average values are summarized in Table 5.9.

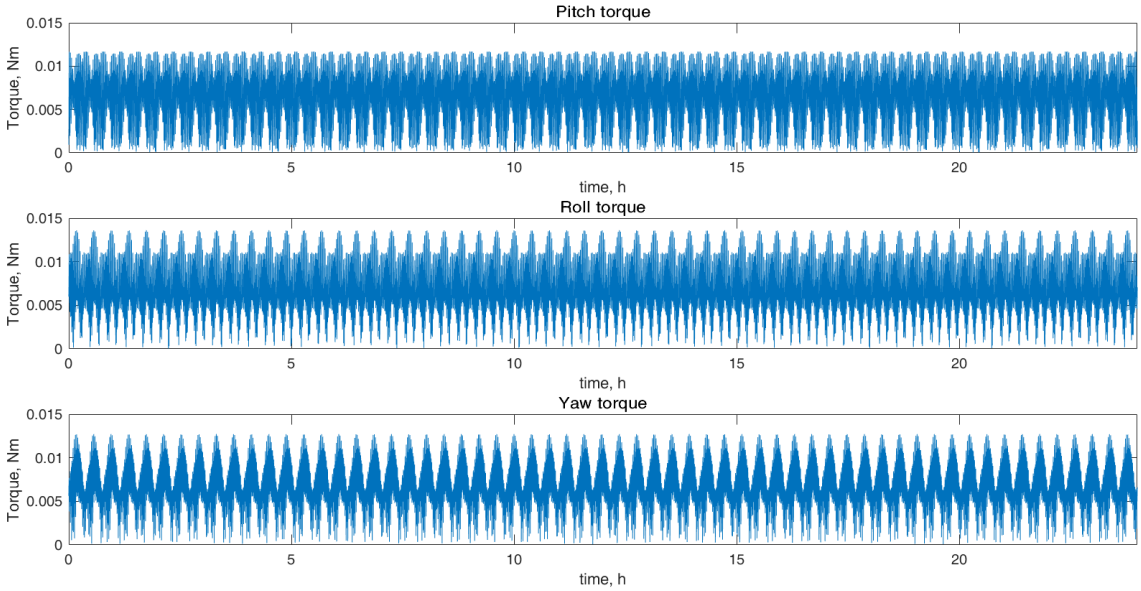

Figure 5.12: Torques generated by the magnetorquers.

Table 5.9: Average values for the generated torques.

Torque	Average Value [Nm]
Pitch	0.0064
Roll	0.0070
Yaw	0.0069

Even though the values calculated for the generated torques are rough approximations, it is possible to see that the values are few magnitudes above the perturbative environmental torques. Some magnetorquers specs can be improved, namely the amount of power allocated for them, their length and number of turns, which can increase the value for the magnetic dipole moment and, thus, the generated torque.

In conclusion, although magnetorquers aren't the ideal actuators for cubesat control, it was checked that they are able to generate enough control torques to overcome the disturbing ones. However, these values need to be refined and computed bearing in mind the pointing accuracy from the payloads, integration in the overall structure and control algorithms, in order to guarantee the mission success.

5.4 Orbital Decay

Since the launch of *Sputnik I*, space activities have created an orbital debris environment that poses increasing impact risks to existing space systems, including human space flight and robotic missions [88]. Since CubeSats have several constraints, a de-orbiting strategy can easily be neglected, contributing to the increase of space debris.
In order to mitigate this problem some regulation has already been established. According to NASA-STD-8719.14A, *Process for Limiting Orbital Debris*, requirement 4.6-1, a spacecraft in LEO shall be disposed of by one of three methods [89]:

(a) Atmospheric reentry option:

- Leave the space structure in an orbit in which natural forces will lead to atmospheric reentry within 25 years after the completion of mission but no more than 30 years after launch; or
- Maneuver the space structure into a controlled de-orbit trajectory as soon as practical after completion of mission.

(b) Storage orbit option: Maneuver the space structure into an orbit with perigee altitude greater than 2000 km and apogee less than geostationary orbit - 500 km.

(c) Direct retrieval: Retrieve the space structure and remove it from orbit within 10 years after completion of mission.

Regarding ORCA^{2}Sat, since it has no propulsion system, the de-orbiting strategy shall be compliant with the first option in the method (a). In LEO, atmospheric re-entry is mainly due to Earth's gravitational attraction and drag forces, with a small contribution of both solar radiation pressure and geomagnetic activity.
Mission lifetime was predicted using *STK 11 Lifetime* tool. In order to correctly predict ORCA^{2}Sat's reentry some parameters need to be specified. The first one is termed the Drag Coefficient, C_D, taken from Figure 3.5. Another coefficient is the Solar Radiation Pressure Coefficient, C_{SRP}, where a value of 0 indicates that the satellite is transparent to solar radiation, a value of 1 indicates that it is perfectly absorbing and a value of $^4/_3$ means that it is flat and specularly reflecting. The Drag Area, A_D, is the mean cross-sectional area of the satellite perpendicular to its direction of travel. The Area Exposed to Sun, A_S, is the satellite's mean area projected perpendicular to the Sun's direction. Since the total mass for ORCA^{2}Sat is not yet defined, the maximum defined in Section 4.2 of 5.657 kg is used in the study. The selected Atmospheric Density Model was the *Jacchia-Roberts* model, yielding a value of $9.158 \times 10^{-12}\,\mathrm{kg\,m^{-3}}$ for the atmospheric density at the initial altitude of 380 km. The defined parameters of the two attitudes from Figure 5.4 are summarized in Table 5.10 and the results for both attitudes are represented in Figure 5.13 and Figure 5.14.

Table 5.10: ORCA^{2}Sat parameters for orbital decay study.

Parameter	Attitude 1	Attitude 2
C_D	2.5	2.5
C_{SRP}	$^4/_3$	$^4/_3$
A_D [m^2]	0.01	0.2
A_S [m^2]	0.2	0.2

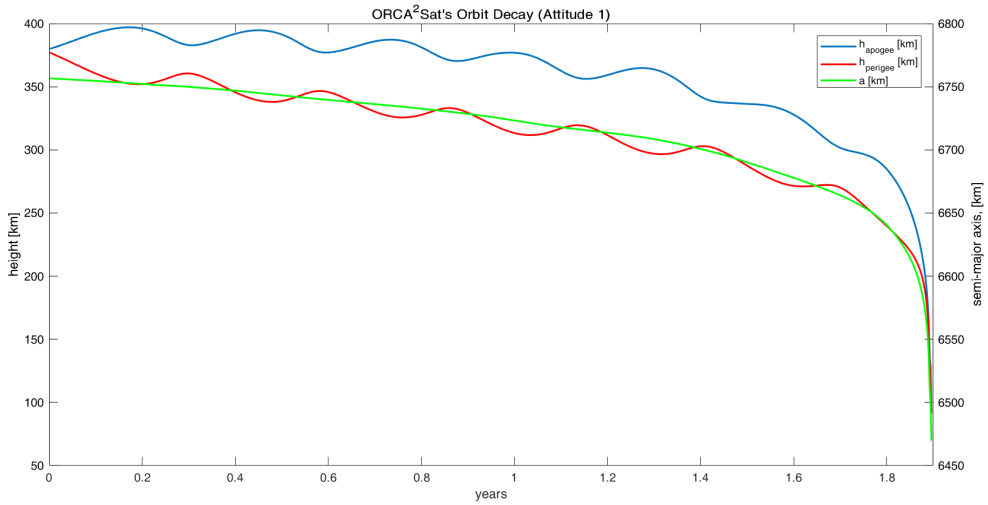

Figure 5.13: Orbital decay of Flight Attitude 1.

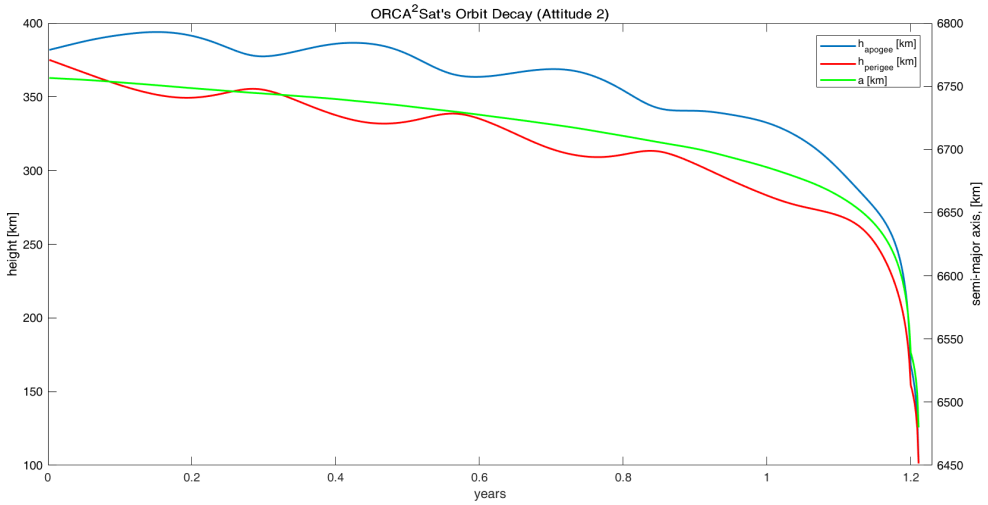

Figure 5.14: Orbital decay of Flight Attitude 2.

As expected, due to a low altitude, ORCA^{2}Sat is within accordance of a 25 years atmospheric reentry. Since the second flight attitude exposes a larger surface area to drag forces, the mission lifetime is about 30% longer for the first attitude. In fact, the lifetime of the first flight attitude is almost two years (1.8 years), opposed to less than 1.2 years from the second flight attitude.
A recommended value for the mission's lifetime regarding ALTAIR payload was set to be at least one year. However, a threshold was not defined yet for the SFU payload, meaning that the second flight attitude could not satisfy the desired time in orbit.
In conclusion, it was decided to choose the first flight attitude. Besides having a more constant power generation, it also allows for a longer time in orbit, assuring that the minimum time required for both payloads fulfill their purposes is attained.

Chapter 6

Thermal Analysis

Another aspect of vital importance in a mission design is the thermal impact of the space environment. This analysis is even more important for CubeSats due to their several restrictions. A smaller structure is linked to lower thermal inertia and poorer heat dissipation, while the weight limits prevents the use of certain materials with better thermal properties.
The main purpose of a thermal analysis is to evaluate if the temperatures of different components are within the operational ranges when in orbit. A certain structure can experience thermal stresses under uniform temperature if it's made of different materials due to the differences in the materials coefficients of thermal expansion, which produce incompatible strains. One possible scenario is, if the thermal loads reach a point where the materials of a component begin to buckle or if it is subjected to many cycles of thermal loading such that it can fail due to fatigue, the whole structure is compromised [90]. Regarding space missions, some of the risks related to an inadequate thermal system, which can lead to mission failure are:

- High temperature peaks: produce high thermal stresses reducing components safe life and can induce thermal deflections that lead to attitude and pointing errors;
- High temperature deltas: cyclic thermal stresses may lead to failure due to fatigue;
- Components outside temperature limits [21]:
  (i) Operating temperature range: the maximum and minimum temperature limits between which components successfully and reliably meet their specified operating requirements;
  (ii) Turn-on temperature: the maximum and minimum temperature limits between which components are able to be turned on without experiencing any damage or malfunction;
  (iii) Non-operating temperature range: temperature limits within which components are able to survive while in a power off mode, and subsequently perform as required in the previous modes.

The two worst cases regarding the spacecraft's temperature must be analyzed. Said cases are antagonistic to one another: in one case an idle power consumption is considered with minimum solar flux and in the other case it is considered the systems are all operating at full power and with maximum solar flux. These two cases are known as the Cold Case and the Hot Case, respectively. The Cold Case was simulated for the June Solstice and the parameters, including the components' heat dissipation, are summarized in Table 6.1. The Hot Case is set during the December Solstice and its characteristics are listed in Table 6.2.

Table 6.1: Cold Case characteristics.

Solar Flux [$\mathrm{W\,m^{-2}}$]	1323.872
Power PCB [W]	0.1
OBC PCB [W]	0.1
Backplane [W]	0.1
Batteries [W]	0.03

Table 6.2: Hot Case characteristics.

Solar Flux [W m^{-2}]	1411.862
All PCB's [W]	0.15
Backplane [W]	0.15
Solar Cells [W]	0.1
Magnetorquers [W]	0.15
Batteries [W]	0.05
LED's and laser [W]	0.05

If the thermal analysis reveals the existence of systems in poor thermal condition for its normal operation, or if the temperature peaks and deltas need further improvement, the thermal design will be re-iterated presenting solutions for the detected problems. The thermal control subsystem will then ensure that each subsystem will operate within its safe operating temperature range. The next sections describe all the steps and results obtained from the thermal simulations.

6.1 Finite Elements Analysis

The simulations were done with *NX Space Systems Thermal Solver* from *Siemens NX 9* software. Thus, a Finite Elements Model (FEM) of the satellite structure had to be developed in order to predict its behavior in the LEO environment. Since the model of the satellite is very detailed, it must be simplified to be less time consuming to perform simulations.

6.1.1 Structure Idealization

Structure idealization is necessary to remove unnecessary details in the geometry, allowing for more uniform meshes and avoiding the use of a great number of elements to represent small details. The idealizations made are listed below:

- **1U modules' rails:** chamfered and round edges and fasteners' holes removed;
- **1U modules' caps:** round edges and counterbore removed;
- **End caps:** removal of round edges and counterbore;
- **Batteries and magnetorquers:** removal of small design features;
- **Outer rails:** chamfered and round edges and counterbore removed;
- **Side panels and solar boards:** round edges eliminated;
- **Solar cells:** transformation to 2D surfaces due to their thickness;
- **Integrating sphere:** removal of photodiodes, laser input and fasteners' holes;
- **Backplane:** removal of small design features.

6.1.2 Finite Elements Model

The FEM model used to simulate ORCA^{2}Sat's thermal behavior is composed only of 2D and 3D elements. Only the solar cells were modeled with 2D elements meshes due to their negligible thickness when compared to the remaining dimensions. Some properties of such elements are listed in Table 6.3. All the remaining components were modeled with 3D elements. It was decided to not simplify those since the temperature distribution in each of the components is very important to

represent their cyclic thermal behavior during consecutive orbits allowing to identify the critical components from the thermal point of view. The 3D meshes used are cataloged in Table 6.4.

Table 6.3: 2D meshes used in the thermal FEM model with properties from Table 4.6.

Part	Element Type	Thickness [mm]	Material
Solar cells	CQUAD8	0.28	GaInP/GaAs/Ge

Table 6.4: 3D meshes used in the thermal FEM model.

Part	Element Type	Material
Outer rails	TET4	Aluminium 7075-T6
1U modules rails	TET4	Aluminium 6061-T6
End caps	TET4	Aluminium 7075-T6
1U modules caps	HEXA8	Aluminium 6061-T6
Solar boards	HEXA8	FR-4 and Copper laminate
Radiator panel	HEXA8	FR-4 and Copper laminate
Backplane	HEXA8	FR-4 and Copper laminate
Side panels	HEXA8	Aluminium 7075-T6
Battery holder	TET4	Aluminium 6061-T6
PCBs	TET4	FR-4 and Copper laminate
Magnetorquers	HEXA8	Ferrite
Batteries	HEXA8	Properties from Table 4.4

Since the PCBs are made of layers of FR-4 and copper, it is very important to correctly model this laminate. This importance is based on the fact that the thermal conductivity within the plane will be much different from the conductivity through plane.
One simple way of modeling this behavior is to determine those thermal conductivity values. That way, it is not necessary to model the laminate structure, reducing the computational time. Based on experimental measurements, a model to estimate the different conductivities can be found in [91]. The expressions to estimate the in-plane (planar) and through-plane (normal) thermal conductivities, respectively, are:

$$k_{planar} = 385\frac{h_{Cu}}{h} + 0.87 \tag{6.1a}$$

$$k_{normal} = \left[3.23\left(1 - \frac{h_{Cu}}{h}\right) + 0.0026\frac{h_{Cu}}{h}\right]^{-1} \tag{6.1b}$$

where h_{Cu} is the total thickness of the copper layers and h is the total thickness of the PCB. Each PCB, the backplane, solar boards and the radiator panel[1] are composed of four copper layers with a thickness of 35 µm each. With a total thickness of 1.6 mm for each of the boards, the resulting thermal conductivities are: $k_{planar} = 34.5575\,\mathrm{W\,m^{-1}\,K^{-1}}$ and $k_{normal} = 0.3393\,\mathrm{W\,m^{-1}\,K^{-1}}$.
In order to account for radiation exchange, it is fundamental to define the thermal-optical properties of the different components. Such properties depend on both the material and the surface finishing, and were assigned to the correspondent meshes. To reduce the computational weight of the simulation, only external surfaces were considered to participate in the radiation exchange with the space environment: end caps, outer rails, solar boards, radiator panel, solar cells, integrating sphere's front hemisphere, ADCS PCB, battery holder, ALTAIR's module top cap and PCBs' module bottom cap. The remain components radiate to each other, internally.

[1] An ideal material for the radiator would be a Phase Changing Material. However, the one available for the temperature range of interest was toxic, thus, not allowed to be launched from the ISS [92].

For the first analysis, none of the components was treated with surface coatings. However, the effect of adding such features will be analyzed after the worst case conditions are established. In the conditions described, the thermal-optical properties defined for the external surfaces of each component are presented in Table 6.5, where ε is the emissivity and α the absorptivity.

Table 6.5: Thermal-optical properties of different components.

Component	ε	α
Outer rails [5]	0.1	0.14
End caps [5]	0.1	0.14
Solar boards [25]	0.88	0.8
Radiator panel [25]	0.88	0.8
Solar cells [17]	0.88	0.9
Integrating shpere [5]	0.05	0.09
PCBs [25]	0.88	0.8
1U modules [5]	0.1	0.14
Battery holder [5]	0.1	0.14
Batteries [27]	0.3	0.4
Magnetorquers [5]	0.56	0.56

One way of taking into account the conduction through the bolts is defining thermal couplings in connection elements. An example is defining the conductance between the holes: heat rate that passes through a certain area and length, when the temperature difference between each end is 1K. However, after some iterations, and based on the work developed in [64], it was concluded that such variable would not significantly change the results. Thus, in order to reduce the complexity of the model, it was decided to ignore the bolts' conductance in the final model.
The final FEM obtained is represented in Figure 6.1.

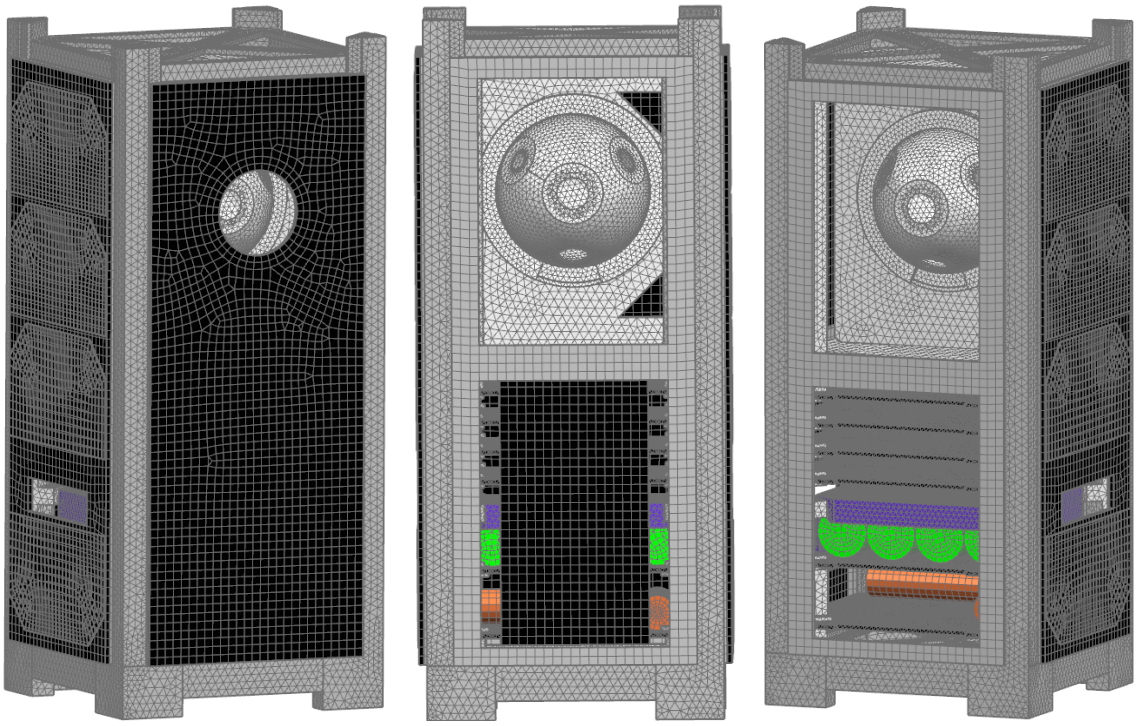

(a) (b) (c)

Figure 6.1: Thermal Finite Elements Model.

6.1.3 Boundary Conditions and Loads

The solver used, *NX Space Systems Thermal*, allows to simulate heat loads from celestial corps, mimicking the loads a satellite experiences in orbit. Instead of applying thermal loads and constraints for each component of the satellite, *Simulation Objects*, *Constraints* and *Thermal Loads* are created. The solar flux, Earth's infrared radiation and albedo are modeled by the *Orbital Heating Simulation Object*, the radiation exchange with the space environment is modeled with the *Simple Radiation to Environment Constraint* while the internal radiation between the components is modeled through the *Radiation Simulation Object*, the conduction between components is simulated with the *Surface-to-Surface Contact Simulation Object* and the heat generated by the electronics stack and other electric components is modeled with the *Heat Load Thermal Load*.
Regarding the solar flux that reaches ORCA^{2}Sat in each case, presented in Table 6.1 and Table 6.2, the software makes use of Eq.(2.15) to compute it for the orbit's characteristics from Table 5.1. The date selected for the Cold Case was June 20^{th} 2021 at 23:30:00 GMST and for the Hot Case was December 21^{th} 2020 at 14:00:00 GMST [93]. To account for the infrared radiation, the software uses the flux that leaves Earth instead of the flux that reaches the satellite, with a predefined value of $237.04\,\mathrm{W\,m^{-2}}$. Finally, the predefined value for the bond albedo is 0.306.
Besides requiring the values for both emissivity and absorptivity, the *Simple Radiation to Environment Constraint* requires a reference value for the radiative environment temperature. Based on ORCA^{2}Sat's orbit, a value of 4K was selected [76]. The *Radiation Simulation Object* computes the view factors between the different components through Eq.(2.18).
For the *Surface-to-Surface Contact Simulation Object*, all components were assumed to be in perfect contact. Besides reducing the complexity of the model is also a valid approximation, since the satellite will be completely epoxied before launch.
Finally, defining the heat loads, because the circuits to be used are not determined yet, neither their location in each PCB, it was chosen to simplify the thermal model and consider the thermal loads correspondent to each circuit are applied to all of the lower area of the corresponding PCB where it should be mounted. This may result in a loss of accuracy of the model, leading to lower temperature peaks, since the same thermal load is being spread over a wider area than the area of the circuit itself.
For the Cold Case, the thermal simulations start with the assumption that the satellite is at a uniform temperature of 8 °C while, for the Hot Case, the value was set to 15 °C. Although this value does not affect the final results, it may influence the elapsed time in each simulation. If it is a bad initial guess of the satellite's temperature, it will increase the computational times, because more iterations will be needed to achieve the final result. The convergence criterion was chosen to be a temperature change less than 0.1 °C between two consecutive orbits.

6.2 Results

Even with the simplifications adopted for the simulations, the time elapsed to get results was in the order of hundreds of hours. Based on the work developed in [64], some guidelines were used in order to ensure an adequate model was being simulated. The two most important parameters in order to get accurate results and a converged solution are the adequacy of the mesh and the number of positions along the satellite's orbit where temperatures are computed. Based on the convergence study presented in Appendix A, a total number of 152080 nodes is an adequate number regarding convergence behavior, as well as 12 orbital positions for temperature computing.
To evaluate the thermal cycling of the components and verify temperature peaks and deltas, the

two worst cases were selected and the average nodal temperature of each component was plotted against time. This allowed to obtain the maximum and minimum temperatures and temperature deltas of each component.

An heat chart with the maximum and minimum temperatures that each component reaches in both the Cold and Hot Case can be found in Figure 6.2. However, due to extensive amount of results, the temperature plots along the different orbits can be found in Appendix B. Only the batteries' thermal behavior is represented in since they are the most critical component.

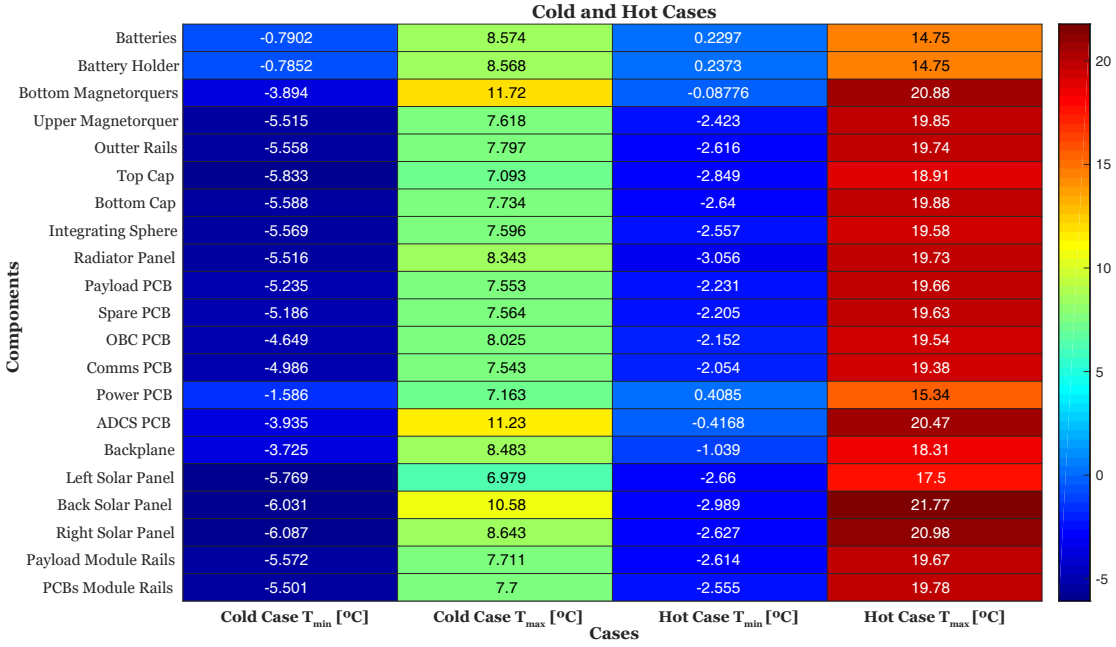

Figure 6.2: Heat map for the different components' extreme temperatures.

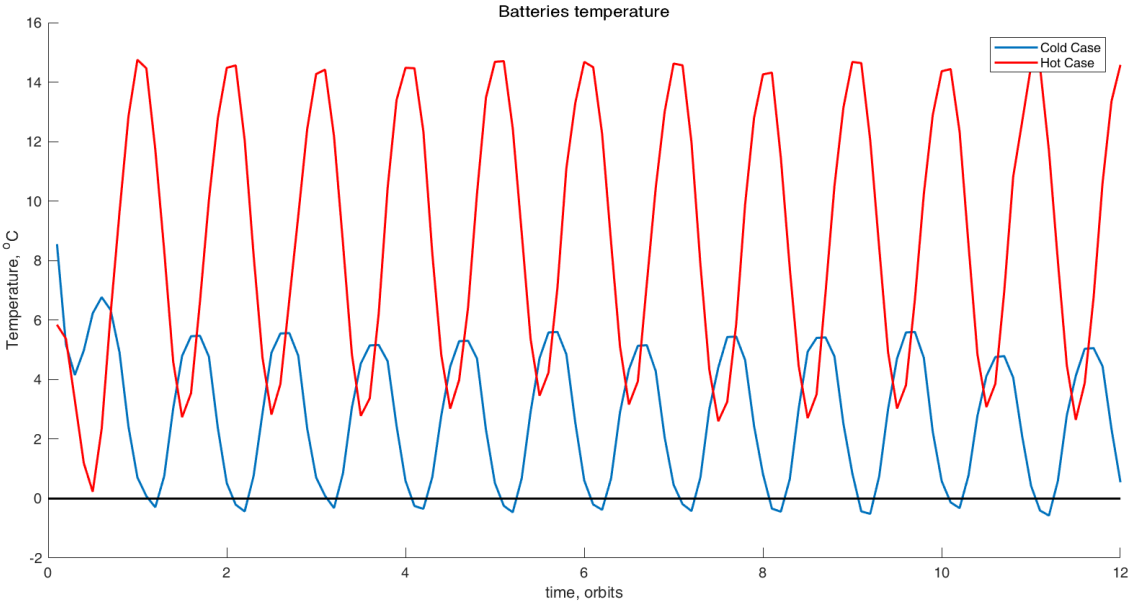

Figure 6.3: Thermal behavior of batteries in both cases.

As can be seen in Figure 6.2, both the minimum temperature of the Cold Case and the maximum temperature of the Hot Case don't reach extremely low or high values. This is due to the very low

altitude of ORCA^{2}Sat's orbit, exposing it to a strong influence of Earth's infrared radiation. In addition, the size of the spacecraft and the amount of time it spends in eclipse (around 35 minutes) allows it to not dissipate large amounts of heat. Furthermore, since there is no surrounding fluid to produce convection cooling, the vacuum environment has a similar effect as thermal isolation itself. Regarding temperature deltas, they are about two times higher for the Hot Case ($\bar{\Delta}t \approx 20.9\,^{\circ}\mathrm{C}$) when comparing with the Cold Case ($\bar{\Delta}t \approx 12.0\,^{\circ}\mathrm{C}$).
According to the results, the batteries' temperature hits values below the limit of $0\,^{\circ}\mathrm{C}$ which allow for them to safely recharge, during the Cold Case. Because of this, it is necessary to develop a Thermal Control System (TCS).

6.3 Thermal Control System

Since power availability is one of the main concerns for this mission, and noting that the batteries' temperature fall outside the range which allows them to recharge, a Thermal Control System must be implemented. The solution of a TCS is preferred over changing the satellite's configuration, since that would affect connections and wirings, deployment switches configuration and the overall operation of other systems.
The implementation of a TCS in small satellites is more challenging than in larger ones. The former suffer high temperature changes in a small time period while the latter tend change their temperature in a much slower rate due to their higher mass, providing an higher thermal inertia. To guarantee the survivability and functionality of the satellite during its on-orbit mission lifetime under the space harsh environment, proper thermal design is important for maintaining all on-board equipment within their acceptable operating temperature ranges. There are two types of thermal control systems: passive and active.
Passive systems don't require a power source to work and don't have moving parts or fluids. They incorporate, among other techniques, multi layer insulation surfaces which minimize temperature gradients by absorbing or reflecting external radiation; the heat dissipated by the on-board components is rejected into space via specific radiator surfaces coated with selective thermal coatings or second-surface mirrors; coatings or paints are applied to increase the emissivity or absorptivity of surfaces and heat spreaders which conduct heat from a small spot to larger heat sinks, which experience lower temperature deltas.
Active systems are typically used when sudden changes of temperature or high temperature deltas may occur. The most common approaches are heaters and heat pipes triggered by sensors. The goal of heaters is to replace the the heat dissipated by the component when it is switched off, warming it up until is turned on again, thus reducing temperature deltas. They are usually electrical resistances that generate heat through Joule effect represented by Eq.(2.30). Heat pipes are sealed tubes through which a fluid passes. The fluid is such that its boiling point matches the controlled unit temperature range. In the hot end of the tube, the fluid boils. The vapor expands into the pipe, carrying the heat, and when reaches the cold end, it condenses, releasing the heat and returning to the initial point, the hot end, to initiate the cycle again.
Although passive systems are simple, highly reliable, lighter, cheaper and easy to integrate, they have lower heat transfer capacity than active systems. In particular, passive thermal design is suitable for thermal control of CubeSats considering their restrictions in power, mass, and volume. Therefore, a passive TCS is the first solution for ORCA^{2}Sat thermal behavior improvement. However, if such solution proves insufficient, an active TCS shall be implemented.
Considering that the batteries' minimum temperature reached is very close to the lower limit

of 0 °C, the first option is the simple use of black dye in the external surfaces to increase both absorptivity and emissivity. This way, a bigger portion of radiation is absorbed by the satellite, and less is reflected, increasing the overall temperature of the components. Thus, the outer rails, end caps, side panels and the battery holder were coated with black paint assuming the values of 0.9 and 0.87 for emissivity and absorptivity, respectively [5]. The obtained results for the minimum and maximum temperatures in worst case conditions are presented in Figure 6.4. A comparison of the batteries' thermal cycle during both the Cold and Hot cases before and after applying the black coat on the structure can be found in Figure 6.5. A similar comparison for the remaining components can be found in Appendix B.

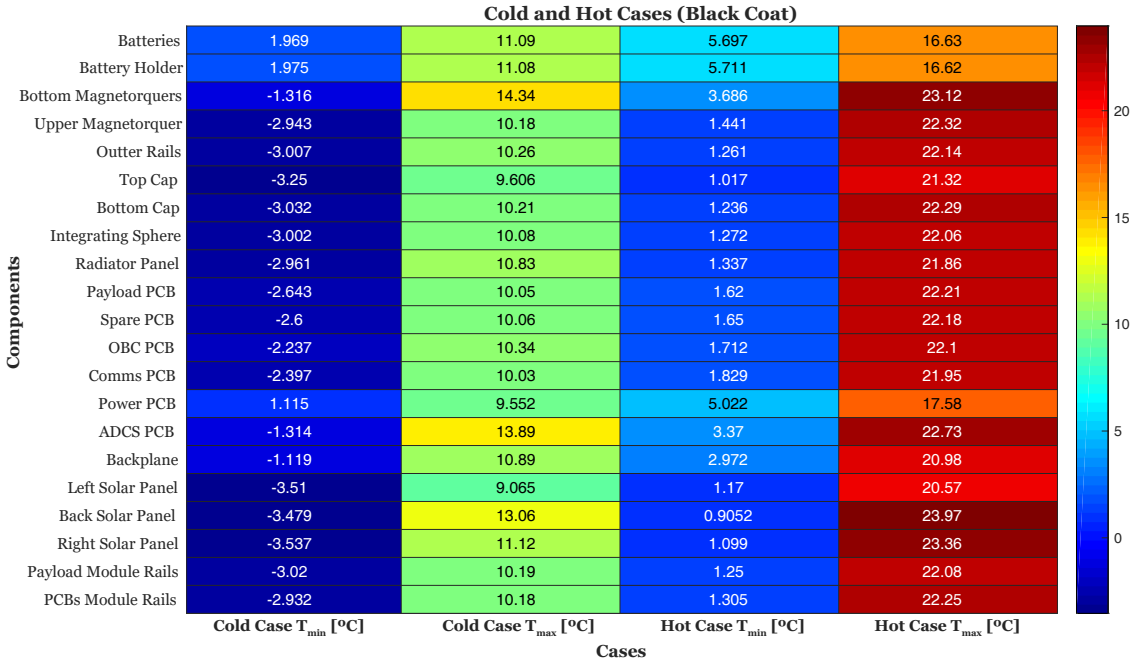

Figure 6.4: Heat map for the different components' extreme temperatures after black coating the structure.

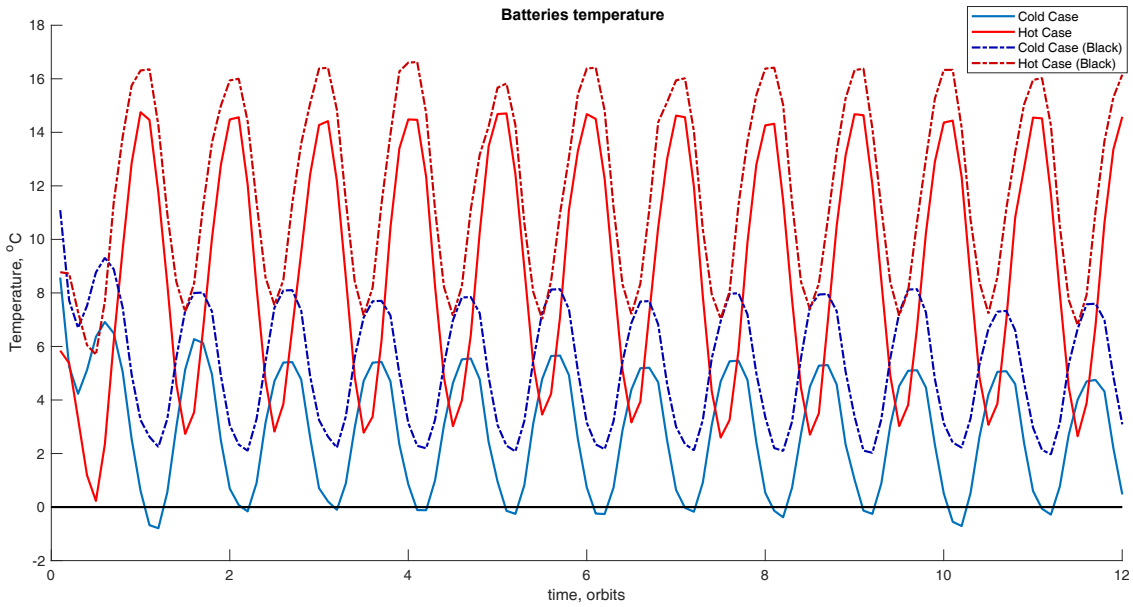

Figure 6.5: Thermal behavior of batteries in both cases before and after applying TCS.

As can be verified, the batteries are now within a safe temperature range that allows them to recharge. The minimum temperatures reached are represented in Figure 6.6. In fact, it can be seen that the minimum temperature reached by the different components has increased after coating the structure. It is also notorious the decrease in the temperature gradient for the hot case. Since the batteries temperature wouldn't go far below 0 °C, applying black dye on the satellite is enough to satisfy the components' safe temperature range. Also, the temperatures ORCA^{2}Sat experiences allow for a freely choosing of sensors, since space graded components have a wider temperature range than the ones exposed in Figure 6.4 [21].
The temperature gradients could be improved by increasing the thermal inertia of the satellite. One way of doing it is by applying panels of a material with low thermal conductivity on the sides of the satellite. However, according to the work done in [64], the temperature gradients were not reduced by a significant amount. In addition, such technique would have a great impact over the the connections of the different systems, specially the wiring from the solar panels to the power board. Therefore, this solution was rejected.
In conclusion, there is no need to change the materials, apply heaters or other insulation components in order to guarantee a safe mission for ORCA^{2}Sat.

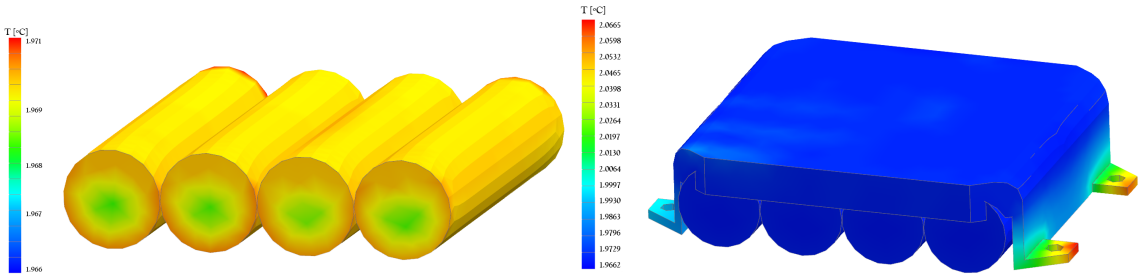

(a) (b)

Figure 6.6: Minimum temperature on batteries' elements during Cold Case of a black structure.

Chapter 7

Dynamic Analysis

Another critical aspect of the mission, is to assure that the satellite is able to withstand induced disturbances. Such disturbances can occur in orbit, on the launch or during transportation of the satellite.

In orbit, the major disturbance source is rotor imbalance from rotating devices (*e.g.* reaction wheels and gyroscopes) due to manufacturing tolerances, followed, followed by lubrication degradation which can increase noise or change the noise performance of different components, release of strain energy at structural interfaces like joints due to thermal snaps, bending of solar arrays or antennas due to temperature gradients, translating parts from cooling systems and electromagnetic forces between wires and heaters [94]. These type of vibrations is termed micro-vibration, occurring at frequencies up to 1000 Hz, although passable of amplification by structural resonances. Micro-vibration generally cannot be controlled or reduced by the ADCS system because they usually involve the flexible modes of the spacecraft structure, rather than its rigid body motion, causing problems for sensitive payloads like high resolution cameras [94].

From the launch until the deployment, the launch vehicle will also induce vibrations on its payload of high amplitude, being structurally more challenging. The strength of these levels of vibration or shock can be higher or lower depending on the specific launch vehicle and the dispenser mounting configuration [95]. The more common sources of vibrations come from the vehicle's engines, either from thrust generation, extinction or sound pressure, stage separation, aerodynamic flows or wind gusts during the initial state of the launching procedure.

During the payload transportation to the launch site, the spacecraft is subjected to vibration loads. Such loads can be originated by the land vehicle transportation and integration in the deployer capsule. In fact, after all the vibration testing is done, making any physical changes to the hardware will invalidate the environmental test, and the mission integrator will require new tests.

One of the requirements for CSDC is that cubesats must have a fundamental frequency of 90 Hz in each axis, in order to prevent components' failure due to vibration loads. Even though ORCA^{2}Sat is not participating in the CSDC, such value shall be used as reference until more information is given by the *Canadian CubeSat Project* regarding this matter.

Similar to the thermal analysis made, modal analyses will also be performed using *Siemens NX 9* to evaluate the lowest natural frequencies and modes of the satellite. After obtaining the results from the modal analyses, the results will be compared with the results from experimental tests from David Florida Laboratory, located in Ottawa. However, since the satellite tested was a 3U participating in the CSDC, the results cannot be used to update the FEM in order to obtain a more reliable model. Therefore, it is only be used as a comparison and similar tests shall be made for ORCA^{2}Sat. If the satellite does not satisfy the requirements, a solution shall be developed.

7.1 Finite Elements Analysis

Similar to the work developed in [64], a bottom-up approach was chosen to produce the final model: a simplified model is simulated and it will progress to a more complex structure until the

final model is reached. In this section, the idealization process, the mesh types, the different FEMs and the results obtained will be described.

7.1.1 Structure Idealization

As in the case of thermal simulations, it is necessary to idealize some of the parts to obtain more uniform meshes and obtain results faster. The dynamic behavior of some of the simplified components shall be compared with the original one, to prove that the idealization process does not affect significantly the dynamic behavior. The idealizations made are listed below:

- **1U modules' rails:** chamfered and round edges removed;
- **1U modules' caps:** round edges removed;
- **End caps:** removal of round edges;
- **Batteries and magnetorquers:** removal of small design features;
- **Outer rails:** chamfered and round edges eliminated;
- **Side panels and solar boards:** round edges eliminated;
- **Solar cells:** transformation to 2D surfaces;
- **PCBs and backplane:** removal of small design features;
- **Integrating sphere:** removal of photodiodes, laser input and round edges in the junction panel;
- **Fasteners:** substitution by 1D beams due their length being much larger than their other dimensions.

Some components, like the PCBs, could be modeled as 2D surfaces because the copper layers weren't relevant in the modal analysis. However, since it was possible to chose how many CPU cores and the amount of memory allocated for the structural simulation, the simulations were done relatively fast. Also, the fasteners' holes couldn't be removed because in this case is important to model the bolts since they hold the structure together and provide overall stiffness.

7.1.2 Finite Elements Model

As stated before, a bottom-up approach was adopted in order to progress from a simple to a complex FEM model. Since the satellite consists of a large number of parts assembled together, this approach allowed to correctly define the contact and connections between components in an easier way. Three FEM models were developed:

- **FEM 1:** Composed of only the external structure, *i.e.*, outer rails, side panels and end caps.
- **FEM 2:** Both 1U modules were added including its internal components, *i.e.*, PCBs, backplane, magnetorquers, batteries, battery holder and ALTAIR payload.
- **FEM 3:** The radiator panel, solar panels and solar cells were finally included, representing a complete ORCA^{2}Sat.

Some properties of the 1D, 2D and 3D elements are listed in Table 7.1, Table 7.2 and Table 7.3, respectively. In Figure 7.1, the three different models are represented.

Table 7.1: 1D meshes used in the modal FEM model.

Part	Element Type	Material
Screws	CBAR	Stainless Steel
Connections	RBE2	-

Table 7.2: 2D meshes used in the modal FEM model.

Part	Element Type	Thickness [mm]	Material
Solar cells	CQUAD8	0.28	GaInP/GaAs/Ge

Table 7.3: 3D meshes used in the modal FEM model.

Part	Element Type	Material
Outer rails	CTETRA10	Aluminium 7075-T6
1U modules rails	CTETRA4	Aluminium 6061-T6
End caps	CTETRA10	Aluminium 7075-T6
1U modules caps	CTETRA4	Aluminium 6061-T6
Solar boards	CHEXA8	FR-4
Radiator panel	CHEXA8	FR-4
Backplane	CHEXA8	FR-4
Side panels	CHEXA8	Aluminium 7075-T6
Battery holder	CTETRA10	Aluminium 6061-T6
PCBs	CTETRA10	FR-4
Magnetorquers	CTETRA10	Ferrite
Batteries	CTETRA10	-

(a) FEM 1 (b) FEM 2 (c) FEM 3

Figure 7.1: Modal Finite Elements Models.

In order to have a more accurate model the mass of the real components was measured and corrected, if necessary, the density of the FEM components. It is important to have the correct mass in the FEM model, since it affects greatly the natural frequencies of the structure. Regarding the battery holder, the one used at testing was just a 3D printed mock up just to demonstrate how it works and, since the final one shall be made of black coated aluminum, the mass was not corrected. The outer rails, end caps, side panels and solar boards used at testing were for a 3U cubesat, so their mass in the ORCA^{2}Sat model was also not corrected. In Table 7.4, the measured masses and the corresponding masses in the FEM model components are listed. The initial density of the modeled components, ρ_i, and the density required to obtain the same mass as the real components, ρ_f, are also presented in the same table.

Table 7.4: Measured mass, FEM model components mass and change in density value to match values.

Component	Real mass [g]	FEM mass [g]	ρ_i [kg m^{-3}]	ρ_f [kg m^{-3}]
Battery	48	56.16	3200	2734.9
PCB	30	26.19	1900	2176.7
1U rails	15	16.17	2700	2503.9
Top cap	38	39.74	2810	2687.1
Bottom cap	88	92.23	2810	2681
Integrating sphere	42	42.98	2700	2638.3
Backplane	16.4	14.54	1900	2143.8
Magnetorquers	33	32.57	4800	4863.7

7.1.3 Boundary Conditions and Loads

As described before, the most significant source of vibrations is the launch vehicle. Therefore, the modal analysis shall be performed for a structure under its launch configuration, accommodated in the deployment system. According to NanoRacks, the NRCSD deployer the only parts of the satellite that are in contact with the capsule are the four outer rails [18]. Thus, said components shall be constrained. An axial view of NRCSD can be found in Figure 7.2.

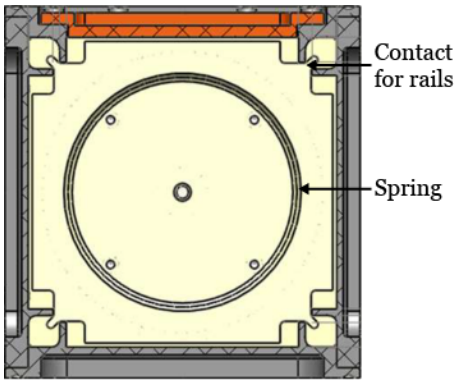

Figure 7.2: NRCSD Axial Cross-Section (+X view). Adapted from [18].

The contact for the rails guarantee that the satellite is deployed with minimal rotation rate as the satellite glides through them. Therefore, the NRCSD constrains the satellite rails in the X direction, but it is allowed to move in Z and Y directions due to clearance. Those shall be the boundary conditions applied.

No loads are applied since the goal is to know the natural frequencies and corresponding modes of vibration, i.e. in free vibration conditions.

Because the model to analyze is an assembly of different components mounted together, it was necessary to define surface contacts between components with faces in contact and consider the solar cells glued to the solar boards. Otherwise, the components would penetrate in each other, giving incorrect results for the natural frequencies and mode shapes. For these constraints to be taken into account, it was also necessary to crate a *Static Subcase* before the *Eigenvalue Method Subcase* of *Solution 103 - Real Eigenvalues*. As stated in [64], such constraints were difficult to apply and consumed hundreds of hours of simulations, since the contacts definition is not straightforward and leads to a long process of trial and error, and in each trial it is necessary to wait for an iterative method to resolve the contacts between the components before proceeding to the eigenvalue extraction.

7.1.4 Results

The modal analysis were performed with *Solution 103 - Real Eigenvalues* from the *NX NASTRAN* solver. Again, the number of elements was based on the worked developed in [64], in order to guarantee solution convergence. The number of elements and the natural frequencies for each FEM are found in Table 7.5 and Figure 7.3 illustrates the first mode of vibration for the different models. Again, a solution convergence study can be found in Appendix A.

Table 7.5: Number of elements and first natural frequencies of each dynamical FEM.

	FEM 1	FEM 2	FEM 3
Number of nodes	308736	673632	790072
f_1 [Hz]	1108.4	660.4	146.3
f_2 [Hz]	1566.9	667.3	155.3
f_3 [Hz]	1611.0	761.6	167.0

As expected, by increasing the total mass of the structure, the natural frequencies assumed lower values. It can also be checked that the fundamental frequency is higher than 90 Hz. However, due to errors associated to the modeling process, this result can't be accepted as proof that the satellite fundamental frequency is actually 146.3 Hz. Nonetheless, the value is almost 40% higher than the one required, which can be accepted as the satellite's fundamental frequency is, indeed, above 90 Hz. Yet, to verify that, the satellite must be assembled and tested experimentally to validate the numerical results and improve the accuracy of the computational model.

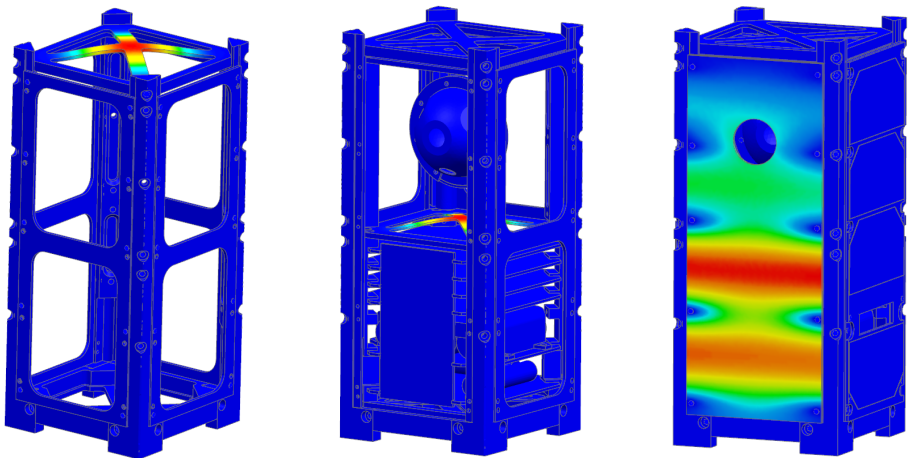

(a) FEM 1 (b) FEM 2 (c) FEM 3

Figure 7.3: First modes of vibrations of each FEM.

7.2 Experimental Modal Analysis

Experimental testing was performed on a shaking table at the National Research Council in Ottawa, by team leaders, for the 3U cubesat *Homathko* as part of the CSDC competition.The experimental testing consisted in performing a sine sweep from 5 Hz to 2200 Hz, followed by a random vibration test and concluded with another sine sweep. The first sine sweep is used to identify the resonance frequencies of the satellite. The random vibrations simulate launch conditions. The last sine sweep is used to verify if the resonance frequencies change. When that happens, it means that a failure in a component or a connection was broken, altering the dynamic behavior of the satellite. The decrease in the natural frequency of *Homathko* during the second sine sweep was due to some screws and connectors that got loose, reducing the structure stiffness and increasing damping. Three tests were performed for each of the satellite axis, but only the results of the first sine sweep are going to be analyzed, since the objective is to compare the resonance frequencies with the natural frequencies obtained for ORCA^{2}Sat.

Six points were used as measuring points and accelerometers were mounted in the chosen locations. The acceleration is measured in the direction normal to the surface they are located in. Those points and the direction of acceleration measured are illustrated in Figure 7.5 and in accordance with the reference body frame. Three accelerometers measured the acceleration in the x direction: one in the payload PCB in the middle 1U module **(3)**, another on the bottom cap of the same module **(5)** and the last one on the battery holder of the last 1U module **(6)**; two measured the acceleration in the y direction: one on the integrating sphere mounting wall **(2)** and another on the side of the battery holder from the middle 1U module **(4)** and the only accelerometer measuring the acceleration in the z direction was mounted on the backside of the integrating sphere mounting wall **(1)**.

Each accelerometer allows to obtain a frequency response for each of the tests. Considering only the sine sweep before the random vibrations, there is a total of 18 measurements of the acceleration with the frequency. Due to the large amount of data, only the needed part of the results will be shown in this work.

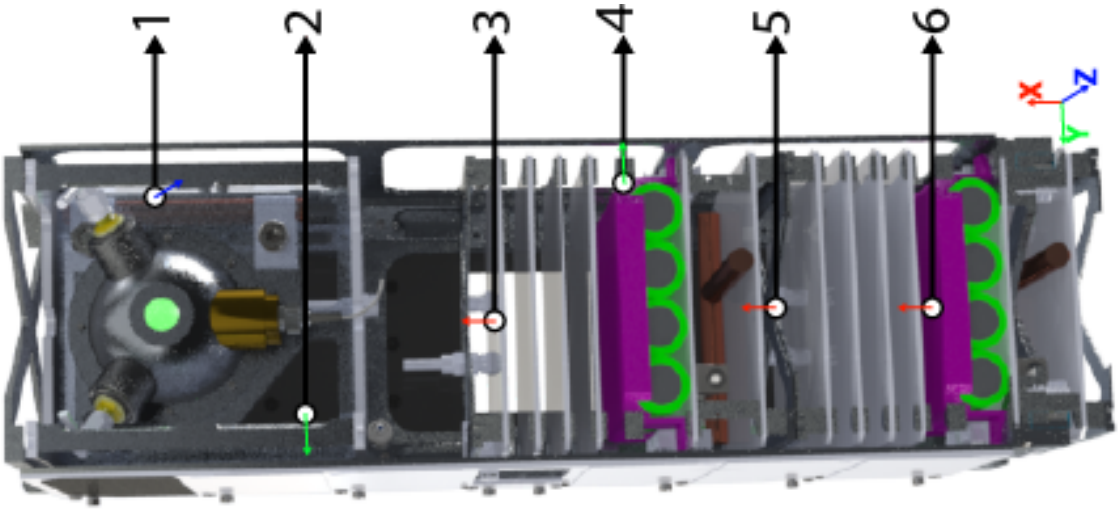

Figure 7.4: Accelerometers locations in *Homathko*.

Since the structure used at testing is heavier than the one used in the experimental model, according to Eq.(2.44), it is expected that the experimental test will yield a smaller value than 146.3 Hz. In fact, as can be seen in , the fundamental frequency of *Homathko* is 130.1 Hz.

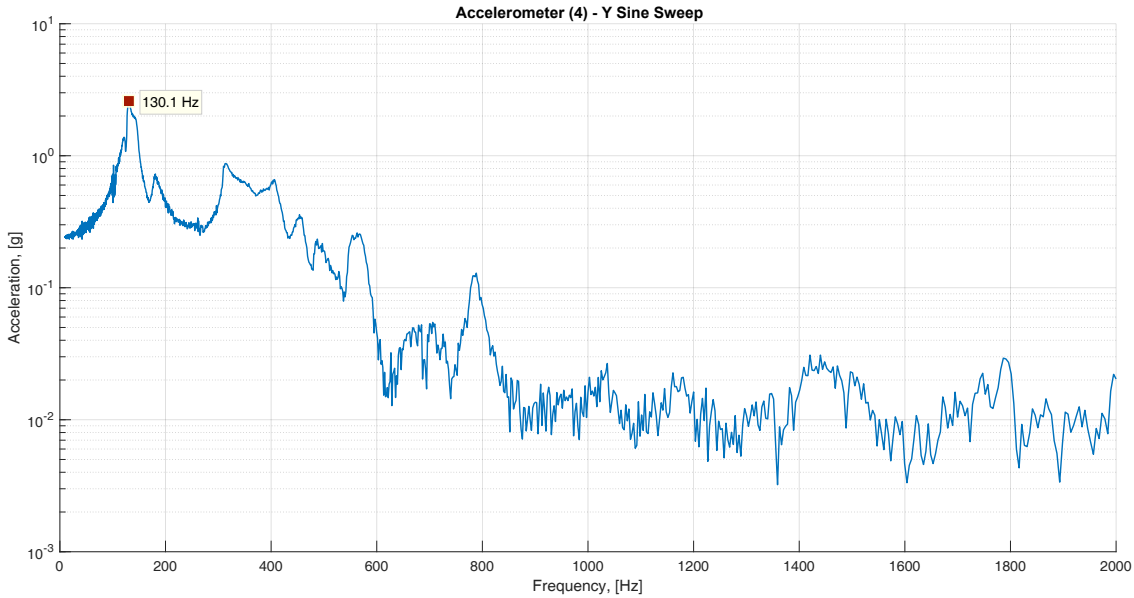

Figure 7.5: Fundamental frequency taken from the measurement of the accelerometer **(4)**.

Besides the distinct mass, the difference between the computational model and the real model results can have other sources. For instance, the boundary conditions during the experimental testing may be different from the ones simulated in the computational model because of the interaction between the testing hardware and sensors mounted and the satellite itself. Another factor can be the damping of the structure, which decreases the resonance frequencies to a value lower than the natural frequencies. The different boards used for testing weren't perfectly equal and are subjected to manufacturing tolerances. Also, the computational model used could have even more refined meshes, even though, with the author resources, that would be complicated.
Nonetheless, it is clear that *Homathko* satisfies the requirement regarding the minimum frequency. Thus, is reasonable to assume that ORCA^{2}Sat also satisfies it. As mentioned before, it is not possible to update the computational model of ORCA^{2}Sat in order to achieve a more precise dynamic behavior. Such procedure can only be done once the same testing is done with the 2U ORCA^{2}Sat structure. However, both results can be compared in a way that allows to predict that ORCA^{2}Sat, indeed, satisfies the requirement of having a fundamental frequency of at least 90 Hz. The FRF amplitude diagram of the accelerometer on the side of the battery holder is the one with a higher response, meaning this should comply with the first mode of vibration from the computational model. However, the battery holder used at testing was 3D printed in Polylactic Acid, which has a much lower modulus of elasticity than aluminum used in the computational model [96]. Nonetheless, the accelerometer placed on the bottom cap of the first 1U module, yield a natural frequency of around 140 Hz and, according to Figure 7.3c, the same component corresponded to the first mode of vibration. Although providing strong evidence of similar modes of vibration, cannot be validated, adding to the fact that the satellite used at testing did not have an aluminum battery holder nor a radiator panel (which corresponded to the first mode of vibration in the full ORCA^{2}Sat computational model). All this information can be used during the future tests of ORCA^{2}Sat in order to achieve the most accurate FEM as possible.

Chapter 8

Conclusions

8.1 Overview

The main goal of this thesis was to assess whether or not ORCA^{2}Sat's mission was feasible from an ISS launch. This study started with an orbital model of the satellite where several aspects of the mission were evaluated.

Due to the mission's nature, it was fundamental to guarantee that the satellite had access to specific ground observatories either for calibration or communication purposes. Since cubesats are subjected to power constraints, the power generation was also estimated for two different flight attitudes. After selecting the more adequate attitude, a power budget had to be developed. Some extreme values had to be assumed in order to show how robust the power system was. In addition, the power budget was simulated over the course of one year as short term power budgets don't allow to draw realistic conclusions. In addition, cubesats are also constrained in terms of volume and mass. Therefore, ORCA^{2}Sat relies on only magnetorquers for active attitude control. As such, the Earth's magnetic field variation was also modeled to ensure ORCA^{2}Sat was capable of generating control torques which could surpass the perturbative environmental torques. The mission duration was also studied with two main concerns: guarantee a minimum mission duration in order to correctly test the payloads and comply with space debris mitigation laws.

A more detailed computational model of ORCA^{2}Sat was developed based on previous work with the aim of studying the thermal impact on the subsystems and the dynamical behavior of the structure. The thermal impact was studied for the two worst cases conditions in terms of minimum and maximum temperatures. The temperatures reached by the different components was evaluated and, by identifying those which attained temperatures outside their safe limits, a thermal control system as developed. Such non-safe temperatures were linked exclusively to the cold case. In addition, due to a low altitude, the minimum temperatures did not reached extremely low values. Therefore, it was studied the impact of coating the outside structure with black paint. This procedure allowed for the implementation of a simple passive thermal control system, maintaining the critical components within safe temperatures range, without needing power supply. The dynamical study aimed to guarantee that the fundamental frequency of the entire satellite was above a specific limit. Although the computational model developed cannot be considered completely reliable, the results were compared with the ones from an experimental analysis. Bearing in mind the errors associated with several modeling assumptions and inherent to the different structures analyzed, the obtained solution cannot be taken for granted. However, there are strong evidences that allowed to conclude that the fundamental frequency is, indeed, above the desired threshold.

Finally, even so all the simulations were specifically done for ORCA^{2}Sat, the results can be applied to other cubesat missions launched from the ISS. That way, investigators can have a quick estimate regarding the success of their mission in terms of ground access, power generation, attitude control, mission duration, thermal impact and dynamic behavior. If it is assessed that the ISS launch won't allow for a successful mission, other launching systems shall be considered.

8.2 Achievements

It was concluded that a launch from the ISS could still guarantee enough access to the different ground observatories in order to correctly test both payloads. Although, it is notorious that a launch from the ISS is preferable for missions which focus on North America access.
The power generated was also within typical values for 2U cubesats. The battery capacity, bound with the in-house design of the power system, allows for an operational throughout the mission. It is important to refer that the values used for the systems' power consumption were a surplus of the real ones and that the power budget was simulated for an entire year. This procedure is crucial since one of the biggest mistakes made by students teams designing cubesats is only doing the power budget for a few days. Power generation varies greatly throughout an year, having a huge impact on the power available in different stages of the mission. Thus, the author developed a user interface in *MATLAB* which is able to produce the power budget with just an *STK* power generated file and the different systems' specifications. Such tool shall help the future of the Canadian team of mission planning and systems design.
Regarding the magnetic field, a very simple study was conducted since the ADCS system was not the scope of this thesis. Nevertheless, for the variation of the Earth's magnetic field, it was proved that the magnetorquers can generate control torques capable of surpassing the perturbative torques inherent to the LEO environment.
As expected, the mission lifetime was very reduced not even reaching a two years milestone. However, even orienting the larger face along the flight direction, allows for enough time in orbit to test the payloads. However, for missions which aim for longer duration without applying changing maneuvers shall consider other launch mechanisms rather than an ISS deployment.
It was also concluded that the altitude at which ORCA^{2}Sat orbits Earth didn't allow for it to reach extremely low or high temperatures. Thus, a simple passive thermal control system of black coating the satellite is enough to keep the batteries within a temperature which allows them to safely recharge. In fact, if the team still decides to use heaters for the batteries due to differences between simulations and real life, there is enough power to allocate for such systems.
Lastly, the dynamic behavior of the structure was evaluated in order to guarantee that the launch won't compromise the satellite's integrity. Even so the value obtained for the fundamental frequency cannot be accepted as definitive, strong evidences show that the satellite's structure is able to withstand the launching loads.
In conclusion, it was proved that ORCA^{2}Sat is able to complete its mission by analyzing several aspects of the mission planning process.

8.3 Recommendations and Future Work

The study performed in this thesis can be improved and continued in several aspects.
For instance, the correct pointing requirements for the different payloads shall be defined and the access time study remade for such changes. Pointing requirements can affect greatly the duration of each access and, in turn, the payload testing.
The power budget can also be improved and include new features. One example is to include the detumbling phase after deployment, allowing to see how much power is drained from the batteries in order to detumble the spacecraft. Such information allows to determine how much power should be allocated for the magnetorquers since while in detumbling phase the satellite is not generating power, being interest in shortening this phase duration.

The thermal FEM can also be upgraded by adding the different sensors and small components when all the hardware is defined. The integrated circuits of the printed circuit boards and micro controllers shall also be modeled. This way, the heat dissipation from the electronic stack can be correctly modeled delivering more accurate results. Routing and wiring can also be modeled using the *Siemens NX* software.

Is strongly recommended to do an experimental testing of the ORCA^{2}Sat dynamic behavior in order to update the the dynamic FEM, resulting in more accurate results. This way, future changes in the structure configuration can be studied with the computational model with a high level of confidence. The same software is also capable of simulating a pre-testing scenario delivering the ideal number of sensors and their location in order to obtain the correct modes of vibration during the experimental testing.

Lastly, it is recommended to increase the computational resources available, in order to obtain more accurate results and to guarantee that the meshes used generate solutions that are converged. This also helps to meet critical deadlines. For example, it is important that the computational model doesn't show flaws or errors before proceeding to the experimental testing. This way, one knows what to expect from the testing results.

Bibliography

[1] "Space Radius." http://www.radiusspace.com. Accessed: 19-04-2018.

[2] D. O. M. A. Rondão, "Modeling and Simulation of the ECOSat-III Attitude Determination and Control System," 2016.

[3] "Satellite Solar Outage." https://www.satandpcguy.com/satellite-help/satellite-solar-outage/. Accessed: 26-04-2018.

[4] V. A. Chobotov, *Orbital Mechanics*. AIAA, Education Series, 1991.

[5] T. L. Bergman, F. P. Incropera, D. P. DeWitt, and A. S. Lavine, *Fundamentals of heat and mass transfer*. John Wiley & Sons, 2011.

[6] H. D. Curtis, *Orbital mechanics for engineering students*. Butterworth-Heinemann, 2013.

[7] D. Roddy, *Satellite Communications*. McGraw-Hill Professional: New York, 2006.

[8] S. Cakaj, B. Kamo, V. Koliçi, and O. Shurdi, "The range and horizon plane simulation for ground stations of low earth orbiting (LEO) satellites," *International Journal of Communications, Network and System Sciences*, vol. 4, no. 09, p. 585, 2011.

[9] D. A. Vallado and D. Finkleman, "A critical assessment of satellite drag and atmospheric density modeling," *Acta Astronautica*, vol. 95, pp. 141–165, 2014.

[10] F. L. Markley and J. L. Crassidis, *Fundamentals of Spacecraft Attitude Determination and Control*, vol. 33. Springer, 2014.

[11] "ThorLabs: Mounted Photodiodes." https://www.thorlabs.com/newgrouppage9.cfm?objectgroup_id=1285. Accessed: 07-07-2018.

[12] *Venus838FLPx GPS Receiver For CubeSat Application - Data Sheet. Version 2.* SkyTraq Technology, Inc., 2018.

[13] *Digital output magnetic sensor: ultra-low-power, high-performance 3-axis magnetometer. Revision 6.* STMicroelectronics, 2017.

[14] *3-Axis Digital Angular Rate Gyroscope. Revision 2.1.* Freescale Semiconductor, 2015.

[15] *Sun Sensor NANO-ISSX/c - Technical Specifications. Version 1.04.* Solar MEMS Technologies, 2016.

[16] *CoolEYE Sensor New Image Sensor Solutions.* Excelitas Technologies, 2015.

[17] "Azur Space: TJ Solar Cell Assembly 3G30A." http://www.azurspace.com/images/products/0003401-01-01_DB_3G30A.pdf. Accessed: 30-07-2018.

[18] A. Mehrparvar, D. Pignatelli, J. Carnahan, R. Munakat, W. Lan, A. Toorian, A. Hutputanasin, and S. Lee, "NanoRacks CubeSat Deployer (NRCSD) Interface Control Document," *NanoRacks, LLC*, 2015.

[19] S. S. Arnold, R. Nuzzaci, and A. Gordon-Ross, "Energy budgeting for cubesats with an integrated FPGA," in *Aerospace Conference, 2012 IEEE*, pp. 1–14, IEEE, 2012.

[20] A. I. Mazlan, K. I. Shakar, and Z. A. Aziz, "Development of Lithium Ion Power System for Satelite," *A Guide to Certified Engineering Companies & Products*, 2009.

[21] W. J. Larson and J. R. Wertz, *Space Mission Analysis and Design*. 1992.

[22] H. Taha, D. Sailor, and H. Akbari, "High-albedo materials for reducing building cooling energy use," 1992.

[23] "Aluminum 7075-T6." `http://www.matweb.com/search/datasheet.aspx?MatGUID=4f19a42be94546b686bbf43f79c51b7d`. Accessed: 16-05-2018.

[24] "Aluminum 6061-T6." `http://www.matweb.com/search/datasheet.aspx?MatGUID=b8d536e0b9b54bd7b69e4124d8f1d20a`. Accessed: 16-05-2018.

[25] "High Performance Laminate and Prepreg." `https://www.isola-group.com/products/all-printed-circuit-materials/fr408hr/`. Accessed: 26-07-2018.

[26] "Panasonic NCR18650B." `https://www.batteryspace.com/prod-specs/NCR18650B.pdf`. Accessed: 27-07-2018.

[27] S. Chen, C. Wan, and Y. Wang, "Thermal analysis of lithium-ion batteries," *Journal of power sources*, vol. 140, no. 1, pp. 111–124, 2005.

[28] "Armstrong Metalcrafts." `https://www.armstrongmetalcrafts.com/Reference/AWGCopperWireProperties.aspx`. Accessed: 17-08-2018.

[29] B. Lal and T. Zurbuchen, "Achieving science with cubesats: Thinking inside the box," in *AGU Fall Meeting Abstracts*, 2016.

[30] H. Heidt, J. Puig-Suari, A. Moore, S. Nakasuka, and R. Twiggs, "Cubesat: A new generation of picosatellite for education and industry low-cost space experimentation," 2000.

[31] A. Mehrparvar, D. Pignatelli, J. Carnahan, R. Munakat, W. Lan, A. Toorian, A. Hutputanasin, and S. Lee, "Cubesat Design Specification R.13," *The CubeSat Program, Cal Poly San Luis Obispo, US*, 2015.

[32] D. Selva and D. Krejci, "A survey and assessment of the capabilities of cubesats for earth observation," *Acta Astronautica*, vol. 74, pp. 50–68, 2012.

[33] "Canadian Satellite Design Competition." `http://www.csdcms.ca/`. Accessed: 23-04-2018.

[34] "The Canadian CubeSat Project." `http://www.asc-csa.gc.ca/eng/satellites/cubesat/what-is-the-canadian-cubesat-project.asp`. Accessed: 06-07-2018.

[35] "The Canadian CubeSat Project: Selected Teams." `http://www.asc-csa.gc.ca/eng/satellites/cubesat/selected-teams.asp`. Accessed: 06-07-2018.

[36] "Photometric Calibration and the Monitor Telescope." `https://www.astro.princeton.edu/PBOOK/photcal/photcal.htm`. Accessed: 24-04-2018.

[37] J. Albert, "Satellite-mounted light sources as photometric calibration standards for ground-based telescopes," *The Astronomical Journal*, vol. 143, no. 1, p. 8, 2011.

[38] C. Pavlovsky, J. Biretta, R. Bohlin, *et al.*, *ACS Instrument Handbook*. STScI, Baltimore, 2001.

[39] J. Bouwmeester and J. Guo, "Survey of worldwide pico-and nanosatellite missions, distributions and subsystem technology," *Acta Astronautica*, vol. 67, no. 7-8, pp. 854–862, 2010.

[40] B. Lynch and C. Wallace, "Cubesat electronic power system," 2014.

[41] P. Bugryniec, "CubeSat: The Need for More Power to Realise Telecommunications," 2016.

[42] I. Vertat and A. Vobornik, "Efficient and reliable solar panels for small CubeSat picosatellites," *International Journal of Photoenergy*, vol. 2014, 2014.

[43] M. M. Garzon, "Development and Analysis of the Thermal Design for the OSIRIS-3U CubeSat," 2012.

[44] H.-u. Oh and T. Park, "Experimental feasibility study of concentrating photovoltaic power system for cubesat applications," *IEEE Transactions on Aerospace and Electronic Systems*, vol. 51, no. 3, pp. 1942–1949, 2015.

[45] E. Escobar, M. Diaz, and J. C. Zagal, "Evolutionary design of a satellite thermal control system: Real experiments for a CubeSat mission," *Applied Thermal Engineering*, vol. 105, pp. 490–500, 2016.

[46] S.-J. Kang and H.-U. Oh, "On-Orbit Thermal Design and Validation of 1 U Standardized CubeSat of STEP Cube Lab," *International Journal of Aerospace Engineering*, vol. 2016, 2016.

[47] A. Ghosh, "Small Spacecraft Active Thermal Control: Micro-Vascular Composites Enable Small Satellite Cooling," 2016.

[48] "Novel Radiation Shielding Material for Dramatically Extending the Orbit Life of Cubesats." `https://technology.nasa.gov/patent/LAR-TOPS-250`. Accessed: 16-04-2018.

[49] S. Weinberg, *Gravitation and cosmology: principles and applications of the general theory of relativity*. Wiley, 2014.

[50] J. M. Palmer and L. Carroll, "Radiometry and photometry faq," *URL: http://www. optics. arizona. edu/Palmer/rpfag/rpfag. htm# motivation*, 1999.

[51] G. Kopp and J. L. Lean, "A new, lower value of total solar irradiance: Evidence and climate significance," *Geophysical Research Letters*, vol. 38, no. 1, 2011.

[52] D. Bhanderi and T. Bak, "Modeling Earth Albedo for satellites in Earth orbit," in *AIAA Guidance, Navigation, and Control Conference and Exhibit*, pp. 64–65, 2005.

[53] V. Khorenko, C. Baur, G. Siefer, M. Schachtner, S. Park, B. Boizot, J. C. Bourgoin, M. Casale, and R. Campesato, "Bol and eol characterization of azur 3g lilt solar cells for esa juice mission," in *E3S Web of Conferences*, vol. 16, p. 03011, EDP Sciences, 2017.

[54] S. Park, J. C. Bourgoin, O. Cavani, V. Khorenko, C. Baur, and B. Boizot, "Origin of the degradation of triple junction solar cells at low temperature," in *E3S Web of Conferences*, vol. 16, p. 04004, EDP Sciences, 2017.

[55] C. Clark and E. Simon, "Evaluation of Lithium Polymer technology for small satellite applications," 2007.

[56] N. A. Saad and M. Ismail, "Influence of geomagnetic field on the motion of low satellites," *Astrophysics and Space Science*, vol. 325, no. 2, pp. 177–184, 2010.

[57] A. C. Stickler and K. Alfriend, "Elementary Magnetic Attitude Control System," *Journal of spacecraft and rockets*, vol. 13, no. 5, pp. 282–287, 1976.

[58] S. P. Bhat and A. S. Dham, "Controllability of spacecraft attitude under magnetic actuation," in *Decision and Control, 2003. Proceedings. 42nd IEEE Conference on*, vol. 3, pp. 2383–2388, IEEE, 2003.

[59] J. E. Oliver, *Encyclopedia of World Climatology*. Springer Science & Business Media, 2008.

[60] D. Bhanderi and T. Bak, "Modeling earth albedo for satellites in earth orbit," in *AIAA Guidance, Navigation, and Control Conference and Exhibit*, p. 6465, 2005.

[61] "Earth Fact Sheet." `https://nssdc.gsfc.nasa.gov/planetary/factsheet/earthfact.html`. Accessed: 07-05-2018.

[62] A. De Luca, *Architectural design criteria for spacecraft solar arrays*. InTech, 2011.

[63] G. L. Matloff, *Deep space probes: To the outer solar system and beyond*. Springer Science & Business Media, 2006.

[64] S. F. C. Aboobakar, "Dynamic and Thermal Models for ECOSat-III," 2016.

[65] "Heat Generation in Electronics," 2014.

[66] *Siemens NX: Thermal Analysis User's Guide*. Siemens Product Lifecycle Management Software Inc, 2014.

[67] J. Archer, "Natural vibration modal analysis," 1968.

[68] S. S. Rao and F. F. Yap, *Mechanical vibrations*, vol. 4. Prentice Hall Upper Saddle River, 2011.

[69] *Siemens NX: Basic Dynamic Analysis User's Guide*. Siemens Product Lifecycle Management Software Inc, 2014.

[70] N. Larbi and J. Lardies, "Experimental Modal Analysis of a structure excited by a random force," *Mechanical Systems and Signal Processing*, vol. 14, no. 2, pp. 181–192, 2000.

[71] P. Avitabile, "Experimental modal analysis: A Simple Non-Mathematical Presentation," *Sound and vibration*, vol. 35, no. 1, pp. 20–31, 2001.

[72] J. D. Hays, J. Imbrie, and N. J. Shackleton, "Variations in the Earth's orbit: pacemaker of the ice ages," American Association for the Advancement of Science Washington, DC, 1976.

[73] C. Han, X. Gao, and X. Sun, "Rapid satellite-to-site visibility determination based on self-adaptive interpolation technique," *Science China Technological Sciences*, vol. 60, no. 2, pp. 264–270, 2017.

[74] "Minimum Antenna Elevation Angle." `https://www.law.cornell.edu/cfr/text/47/25.205`. Accessed: 22-06-2018.

[75] M. Eshagh and N.-A. Mehdi, "Perturbations in orbital elements of a low earth orbiting satellite," *Journal of the Earth and Space Physics*, vol. 33, no. 1, pp. 1–12, 2007.

[76] A. Tewari, *Atmospheric and space flight dynamics*. Springer, 2007.

[77] J. R. Wertz, *Spacecraft Attitude Determination and Control*, vol. 73. Springer Science & Business Media, 2012.

[78] P. C. Hughes, *Spacecraft Attitude Dynamics*. Courier Corporation, 2012.

[79] *Integrating Sphere Theory and Applications*. Labsphere, 2017.

[80] *Concept of Operations for CHIME Calibration Source*. Simon Fraser University, 2018.

[81] Y. Goueffon, L. Arurault, C. Mabru, C. Tonon, and P. Guigue, "Black anodic coatings for space applications: Study of the process parameters, characteristics and mechanical properties," *Journal of Materials Processing Technology*, vol. 209, no. 11, pp. 5145–5151, 2009.

[82] "The FreeRTOS Kernel." `https://www.freertos.org/`. Accessed: 27-07-2018.

[83] "Hercules TMS570LS Safety MCU." `http://www.ti.com/en/download/mcu/SPRB204.pdf?DCMP=hercules&HQS=hercules-mc`. Accessed: 27-07-2018.

[84] "ISS TRAJECTORY DATA." `https://spaceflight.nasa.gov/realdata/sightings/SSapplications/Post/JavaSSOP/orbit/ISS/SVPOST.html`. Accessed: 18-04-2018.

[85] P. A. Anigstein and R. S. Peña-Sanchez, "Analysis of solar panel orientation in low altitude satellites," *IEEE Transactions on Aerospace and Electronic Systems*, vol. 34, no. 2, pp. 569–578, 1998.

[86] "The World Magnetic Model." `https://www.ngdc.noaa.gov/geomag/WMM/DoDWMM.shtml`. Accessed: 29-04-2018.

[87] N. Khalifa, "Space base laser torque applied on leo satellites of various geometries at satellite's closest approach," *NRIAG Journal of Astronomy and Geophysics*, vol. 2, no. 2, pp. 266–271, 2013.

[88] J. C. Liou and N. L. Johnson, "Risks in space from orbiting debris," *SCIENCE-NEW YORK THEN WASHINGTON*, vol. 311, no. 5759, p. 340, 2006.

[89] *Process for Limiting Orbital Debris*. NASA-STD-8719.14A, 2012.

[90] G. F. Abdelal, N. Abuelfoutouh, and A. H. Gad, *Finite element analysis for satellite structures: applications to their design, manufacture and testing*. Springer Science & Business Media, 2012.

[91] J. E. Graebner, "Thermal conductivity of printed wiring boards," *Electronics Cooling Magazine*, 1995.

[92] S. Chandel and T. Agarwal, "Review of current state of research on energy storage, toxicity, health hazards and commercialization of phase changing materials," *Renewable and Sustainable Energy Reviews*, vol. 67, pp. 581–596, 2017.

[93] "Solstices & Equinoxes." `https://www.timeanddate.com/calendar/seasons.html`. Accessed: 12-06-2018.

[94] G. Aglietti, Z. Zhang, G. Richardson, B. Le Page, and A. Haslehurstl, "Disturbance sources modeling for analysis of structure-borne micro-vibration," in *Proceedings of III ECCOMAS Thematic Conference on computational methods in structural dynamics and earthquake engineering*, 2011.

[95] *CubeSat101: Basic Concepts and Processes for First-Time CubeSat Developers*. NASA CubeSat Launch Initiative, 2017.

[96] "Young's Modulus - Tensile and Yield Strength for common Materials." `https://www.engineeringtoolbox.com/young-modulus-d_417.html`. Accessed: 19-07-2018.

Appendix A

FEM Solution Convergence Study

Thermal Analysis

A crucial step while performing FEM analysis is verifying the adequacy of the mesh used. In the case of the thermal analysis of a satellite, another important parameter is to evaluate if the number of orbital positions to compute the spacecraft's temperature is enough to obtain a converged solution.

Since thermal simulations required several hours to deliver a solution, it was decided not to increase both parameters at the same time. Thus, its was decided to use a coarse mesh and increase the number of orbital positions, evaluating for the same time instant the temperatures of three different nodes located in the top cap, the power PCB and in the exit port of the integrating sphere. Then, the same process was followed for a constant number of 6 orbital positions and increasing the number of nodes, *i.e.*, using sequential refined meshes.

As represented in Figure A.1, for the two different convergence studies, both solutions did not fully converge. However, the change in the temperature is relatively small after 12 orbital positions and for meshes with at least 1.5×10^5 nodes.

Since meshes with over 1.5×10^5 nodes and computing temperatures for more than 10 orbital positions would greatly increase the simulation running time, it was decided to use the model with 152080 nodes, computing temperatures for 12 orbital positions. This decision allowed to obtain an enough accurate solution while maintaining the running time within acceptable values.

Dynamic Analysis

Since Dynamic Analysis took less time to compute and, contrary to the Thermal Analysis, did not require any orbital information, it was possible to use finer meshes than the one used for thermal simulations. However, for extremely refined meshes, the computing time would increase exponential.

The convergence study presented in Figure A.2 consisted in sequentially refining the mesh of the three different models simulated. Again, the solution did not fully converge due to computational resources. However, after a threshold of the number of nodes, the solution did not change significantly and a trend of the decrease in the slope with the mesh refinement is noticeable.

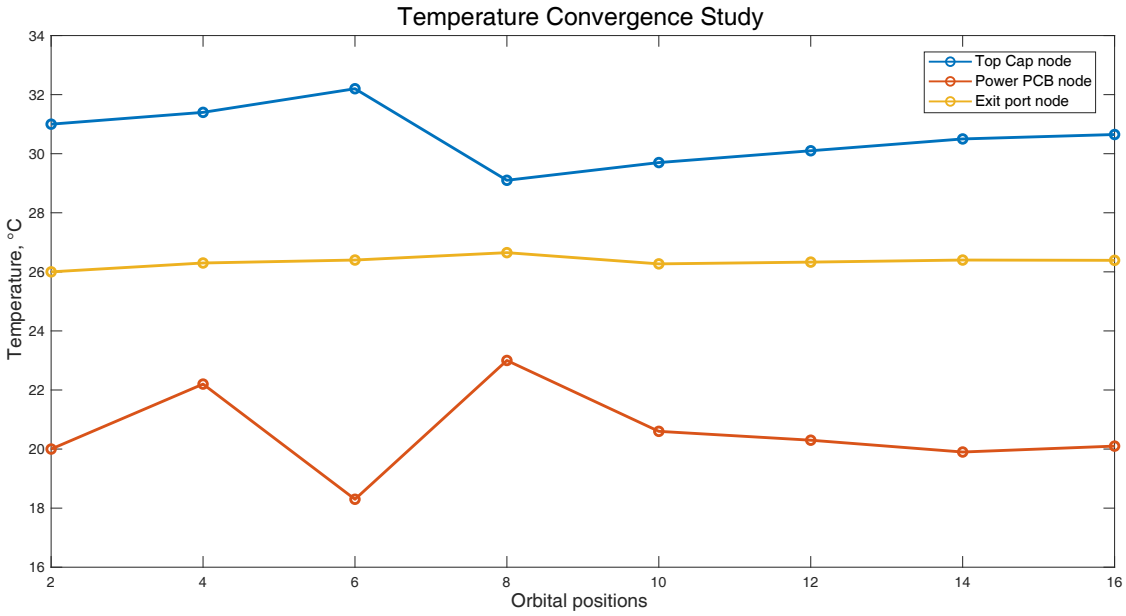

(a) Temperature convergence in function of the number of orbital positions.

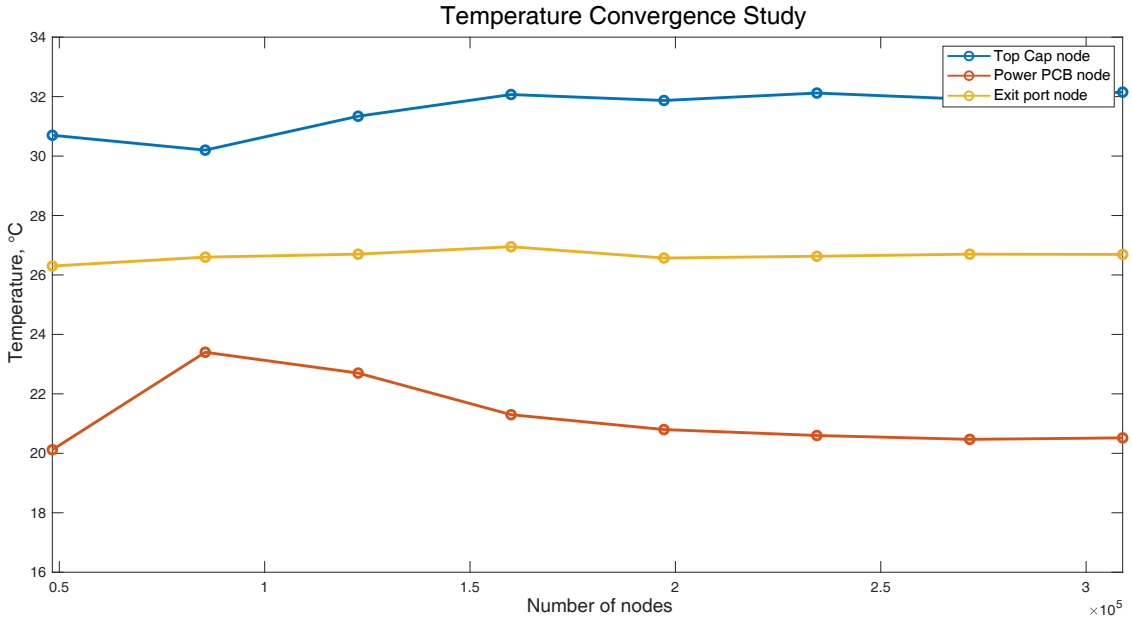

(b) Temperature convergence in function of the number of nodes.

Figure A.1: Thermal analysis convergence study.

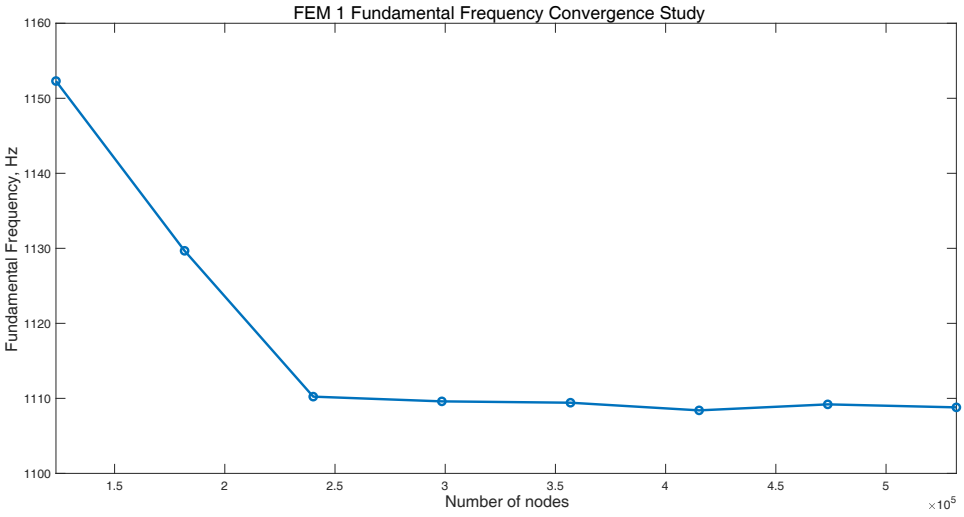

(a) Fundamental frequency convergence for FEM 1.

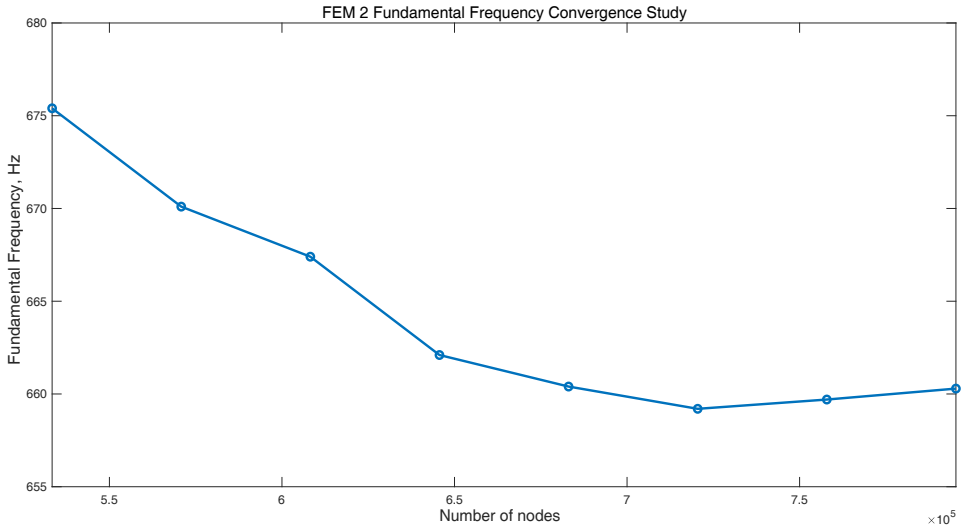

(b) Fundamental frequency convergence for FEM 2.

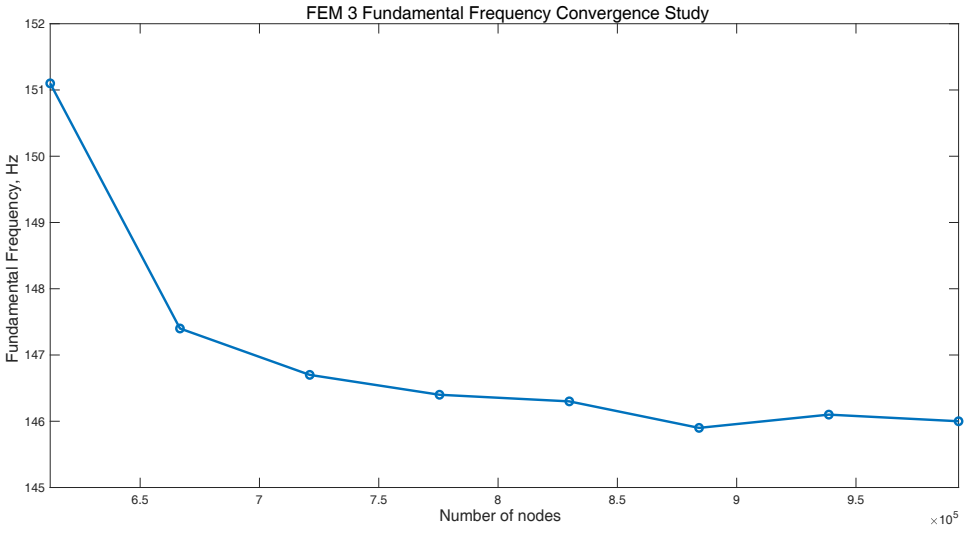

(c) Fundamental frequency convergence for FEM 3.

Figure A.2: Dynamic analysis convergence study.

Appendix B

Thermal cycles for the different components

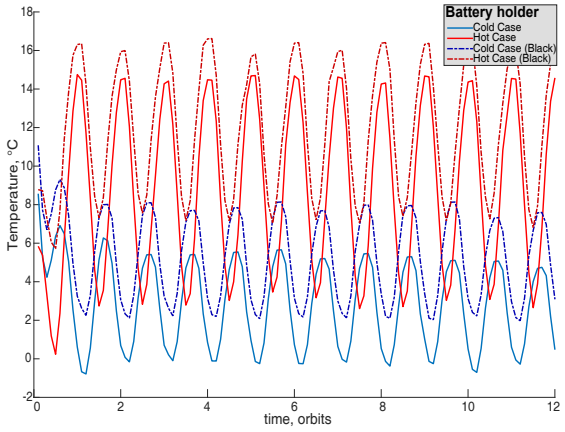

(a) Battery holder

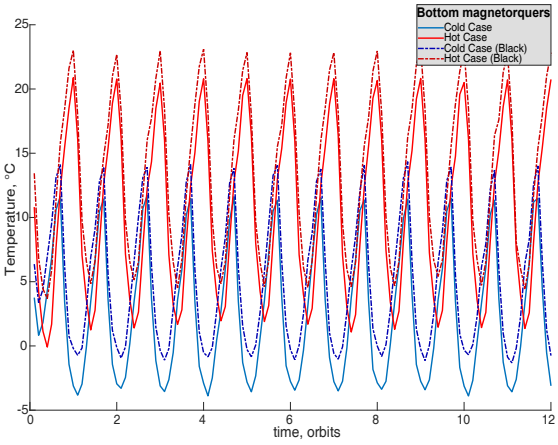

(b) Bottom magnetorquers

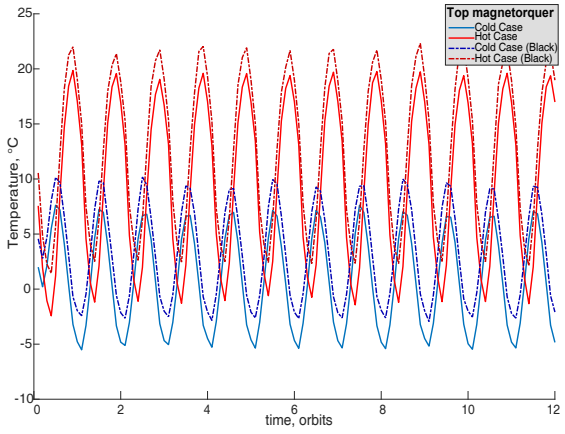

(c) Top magnetorquer

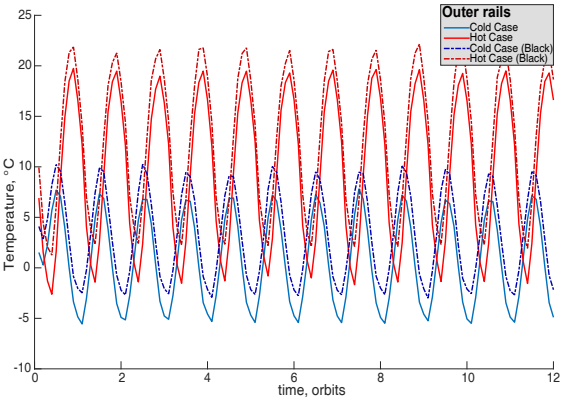

(d) Outer rails

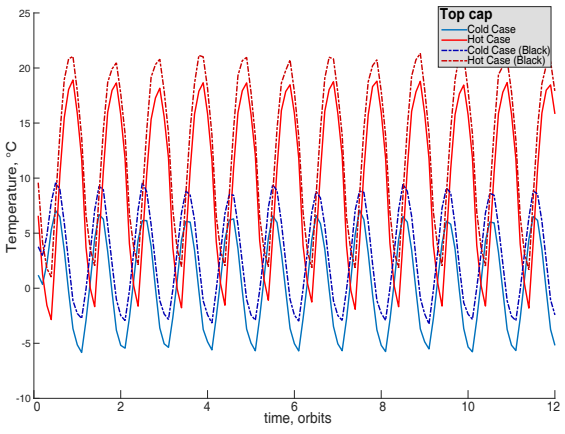

(e) Top cap

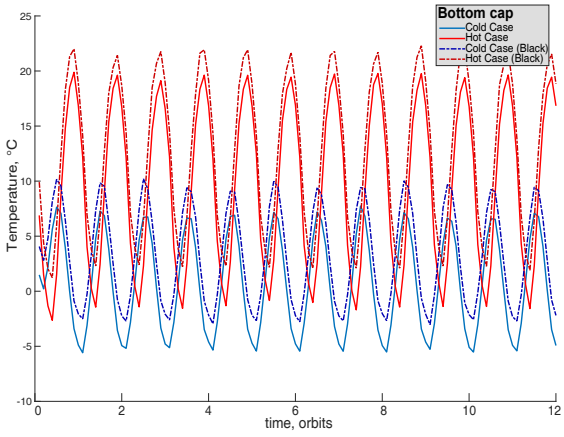

(f) Bottom cap

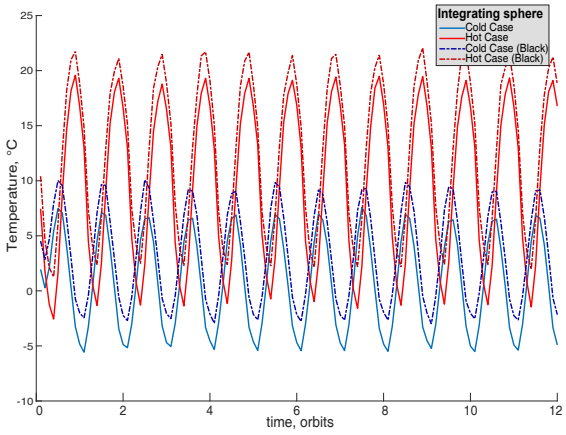

(g) Integrating sphere

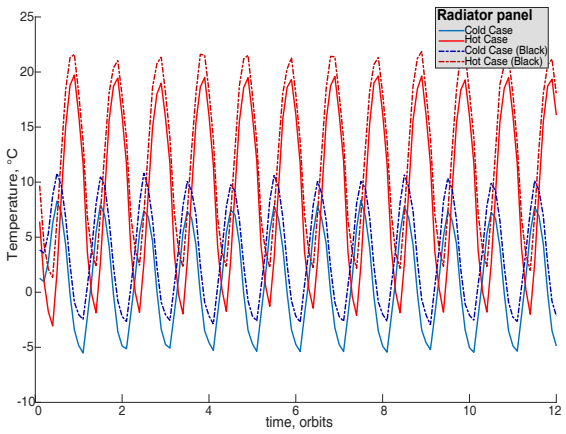

(h) Radiator panel

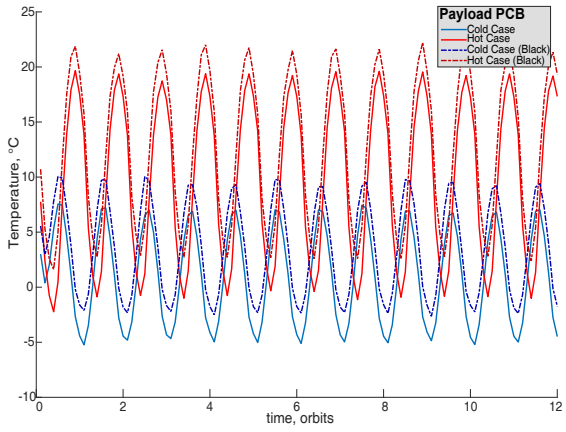

(i) Payload PCB

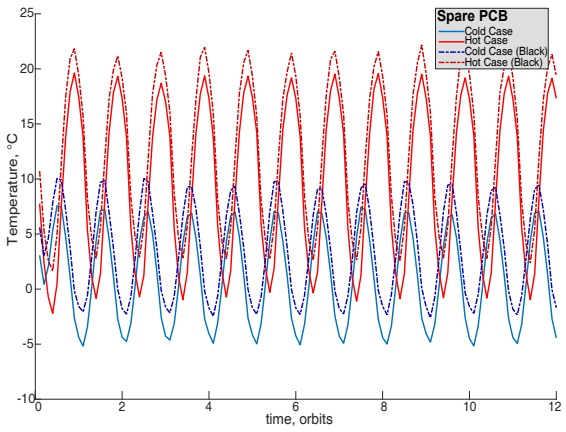

(j) Spare PCB

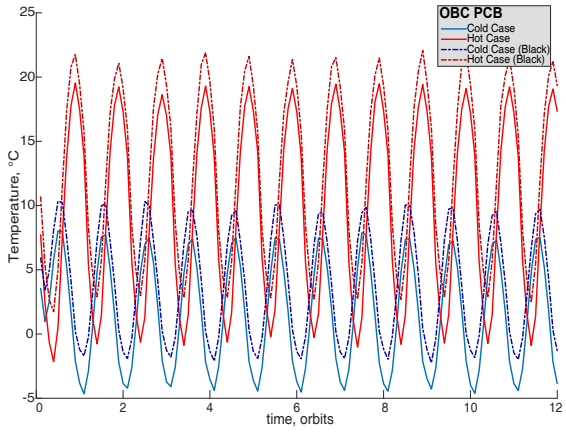

(k) OBC PCB

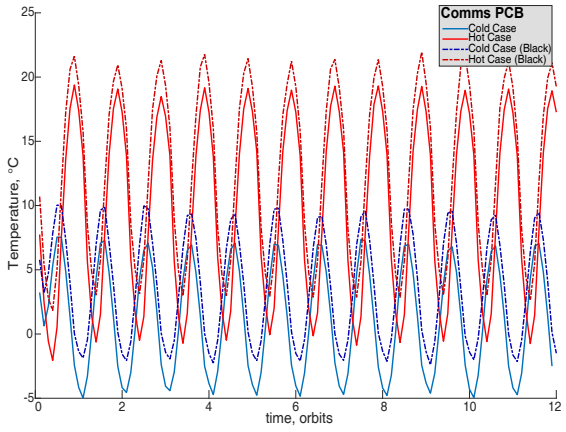

(l) Comms PCB

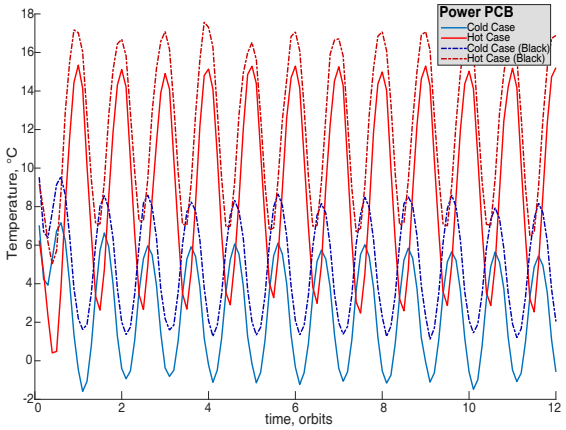

(m) Power PCB

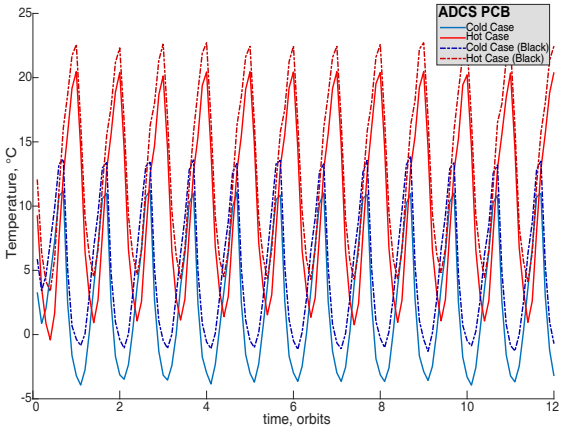

(n) ADCS PCB

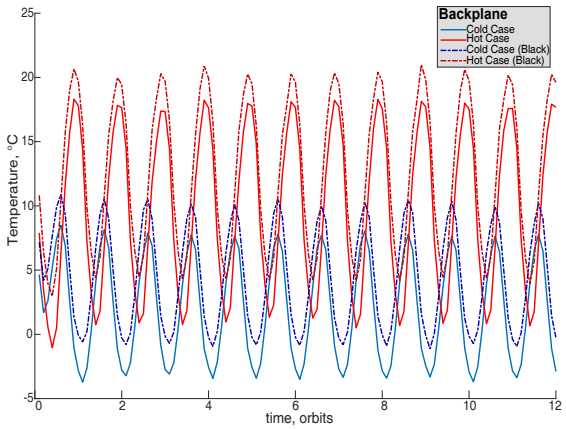

(o) Backplane

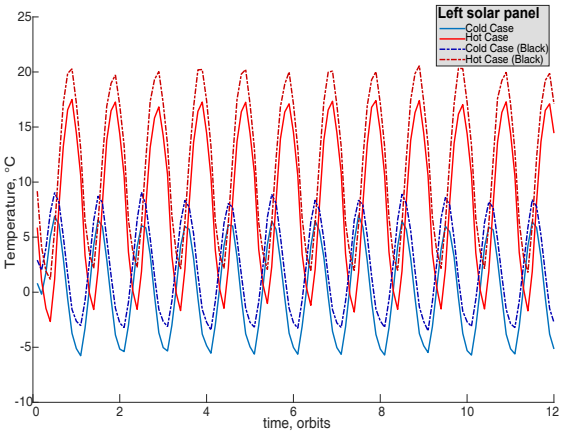

(p) Left solar panel

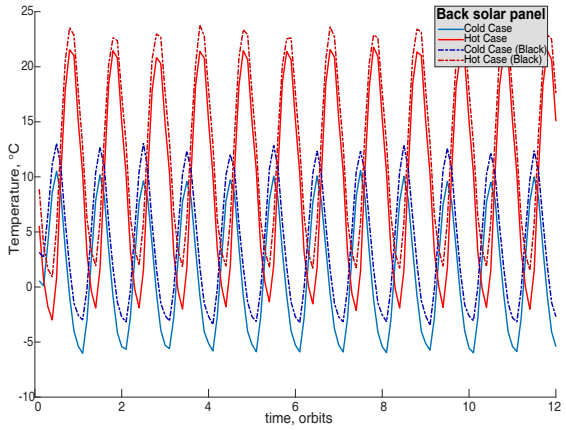

(q) Back solar panel

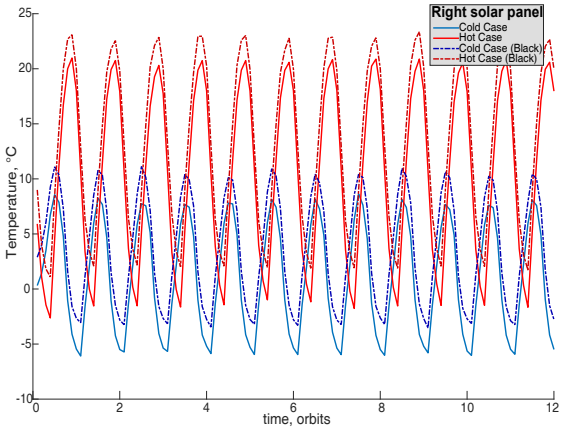

(r) Right solar panel

Figure B.-1: Thermal cycles for the different components.